Iterative Learning Control for Fuel Robust HCCI

by

Craig E. Slepicka

A thesis submitted in partial fulfillment of the requirements for the degree of

Master of Science

Department of Mechanical Engineering
University of Alberta

Abstract

A dual-fuel system is used to control HCCI combustion timing and load in a CFR engine. The systems steady-state response to iso-octane and n-heptane injected energy is investigated then a dynamic ARMAX model is found using system identification. This model is used to design a norm-optimal Iterative Learning Controller (ILC). A new design for an ILC is developed that requires minimal system information and is called the model-less ILC. The stability and noise transference of this new design is investigated. Both ILC designs are then optimized for experimental implementation. To attenuate noise in the system two non-causal filters are developed to use with the ILC: a Gaussian and a zero-phase Butterworth. The filters are optimized on the ARMAX model and then implemented on the CFR engine. The three best ILC designs are are found to be the model-less with zero-phase Butterworth, norm-optimal with zero-phase Butterworth and a norm optimal without a filter. These ILC designs are compared to a Proportional-Integral (PI) controller and all three ILCs are found to out perform the PI controller.

The three best ILC designs are then implemented on the engine with different operating conditions to explore the controller robustness. The intake temperature and compression ratio are varied and all ILC designs performed well with the ILC convergence time being most affected by these disturbances. The disturbance rejection of the controllers is then tested with the addition of biofuels: ethanol and biodiesel. The controllers are able to converge with the new fuel and out-performed the PI controller subject to the same biofuel disturbance.

For the CFR engine with HCCI combustion performing repetitive steps in combustion timing and load, ILC outperforms PI control and is robust to changes in intake temperature, compression ratio and the addition of biofuels with little changes in the final iteration reference tracking error.

Table of Contents

List of Tables

List of Figures

Nomenclature

Acronyms

aTDC	after Top Dead Center
bTDC	before Top Dead Center
CA20-80	Crank Angles for 20% to 80% mass burned
CA50	Crank Angle of 50% mass burned
CFR	Cooperative Fuels Research
CI	Compression Ignition
CO	Carbon Monoxide
CO_2	Carbon Dioxide
COV	Coefficient of Variation
CR	Compression Ratio
DAQ	Data AcQuisition
EGR	Exhaust Gas Recirculation
EPA	Environmental Protection Agency
EVC	Exhaust Valve Closing
EVO	Exhaust Valve Opening
EVVT	Electromagnetic Variable Valve Timing
HCCI	Homogeneous Charge Compression Ignition
HTHR	High Temperature Heat Release
ILC	Iterative Learning Controller

IMEP	Indicated Mean Effective Pressure
IVC	Intake Valve Closing
IVO	Intake Valve Opening
KLSA	Knock Limiting Spark Advance
LHV	Low Heating Value
LTHR	Low Temperature Heat Release
LTI	Linear Time Invariant
MIMO	Multi-Input Multi-Output
MON	Motor Octane Number
NO_x	Oxides of Nitrogen
O_2	Oxygen
OI	Octane Index
ON	Octane Number
PI	Proportional Integral
PRF	Primary Reference Fuel
PW	Pulse Width
RON	Research Octane Number
RPM	Revolutions Per Minute
SI	Spark Ignition
SISO	Single-Input Single-Output
SOC	Start of Combustion
TDC	Top Dead Center
uHC	unburnt HydroCarbons

Symbols

γ	Ratio of Specific Heats
λ	Airfuel Equivalence Ratio
$\delta CA50$	Error in CA50
$\delta IMEP$	Error in IMEP
δP	Error in Cylinder Pressure
η	Thermal Efficiency
θ	Crankshaft Angle
d	Sytem Disturbance
$E_{bio/hept}$	Injected Energy of Biodiesel/n-heptane Mixture
$E_{eth/iso}$	Injected Energy of Ethanol/iso-octane Mixture
E_{hept}	Injected Energy of n-heptane
E_{inj}	Injected Energy
E_{iso}	Injected Energy of iso-octane
e	Output Error
f_{cut}	Cut-off Frequency
h_t	Heat Transfer Coefficient
j	Iteration Index
J	Steady-State Jacobian
k	Cycle Index
K	Model-less ILC Gain
K_I	Integral Gain
K_P	Proportional Gain
L_e	ILC Learning Filter
L_u	ILC Forgetting Filter

O	Filter Order
P	Pressure
$Q(\theta)$	Heat Release
Q_{filt}	ILC Filter
T	Temperature
u	Plant Input
V	Cylinder Volume
V_d	Displaced Volume
y	Plant Output
y_r	Reference Signal

Chapter 1

Introduction

This Chapter details the problem addressed in this thesis, why it should be addressed and how it is investigated.

1.1 HCCI

Homogeneous Charge Compression Ignition (HCCI) is type of combustion that uses the auto-ignition properties of the fuel to incite combustion. By igniting the fuel in this manner, combustion occurs much quicker than traditional combustion strategies, like Spark Ignition (SI) or Compression Ignition (CI), leading to higher thermal efficiencies Stanglmaier and Roberts [1999]. As well low NOx and soot emissions have been found with HCCI combustion due to the low temperature observed during and after combustion Iida et al. [2003]. However, several drawbacks are known for HCCI combustion. Due to the fast combustion, high pressure rise rates occur and can be damaging to the engine Oakley et al. [2001], therefore less fuel must be used so as not to damage the engine, which limits the load of the engine. Also, due the low temperature high amounts of unburnt HydroCarbons (uHC) and CO are produced compared to CI engines Stanglmaier and Roberts [1999]. Since the combustion is a dictated by chemical kinetics Najt and Foster [1983], combustion timing is difficult as there is no direct mechanism to control combustion like there is with SI and CI

engines.

1.2 Problem Statement

The objective of this research is to design and test a control strategy that can control combustion timing for an HCCI engine. The control method will involve using a dual-fuel strategy to control both combustion timing and load. The method will be tested for its robustness for changes in operating conditions and the use of biofuels. The control strategy chosen is an Iterative Learning Controller (ILC).

1.3 Motivation

The US Environmental Protection Agency (EPA) and National Highway Traffic Safety Administration (NHTSA) have begun setting new standards for emissions and fuel economy for cars and light trucks with model years between 2017-2025 EPA [2012]. These regulations will enforce a combined CO2 emission of cars and trucks at 163 g/mi and a fuel economy of 54.5 mpg by the end of 2025. The 2014 regulation for CO_2 emissions is 293 g/mi with a fuel economy of 31.3 mpg. This enforcement is estimated to cut 6 billion tonnes of GHG over the years 2012-2025 and save $1.7 trillion in fuel costs. This improvement is expected to come from advancements in internal combustion engines EPA [2012]. HCCI engines can provide part of this improvement by having a higher thermal efficiency.

With HCCI's unique combustion strategy multiple fuels can be used Fiveland et al. [2001]. This can utilized to for the use of biofuels Arrègle et al. [2009]. Biofuels are useful in that they can be carbon neutral and are a renewable resource Schneider [2010]. Work is currently happening of the development of advanced biofuels, which are derived from non-food source feedstocks BFN [2013]. This allows fuel to be produced without decreasing the worlds food supply while producing low net green-

house gas emissions. Many of these biofuels have different properties compared to traditional gasolines Schneider [2010]. This means they cannot be readily put into traditional SI engines and must either go through further processing to become a drop-in fuel or a new combustion strategy, like HCCI must be used.

ILC is chosen as the control method as it can optimize the input sequence for a process that is repetitive. Any engine application that requires repetitive operation is well suited for ILC implementation. This may include idle speed control for disturbance rejection, load changes for generator applications or even en route performance optimization for mass transit systems Kapania and Gerdes [2015]. By using an ILC to control HCCI combustion timing, the ILC can optimize the input so that the system follows the reference trajectory without a loss of performance.

1.4 Thesis Organization

This thesis begins with operating a dual fuel engine using primary reference fuels. This will be the base point that will be used to compare control structures. This base point has a system identification as well as an operating domain variation. These are used to generate a norm-optimal control and a model-less control. The stability and optimization of these control strategies are investigated. Then the application of non-casual filters is explored. Finally the ILC is tested against a traditional Proportional-Integral (PI) controller.

Next the robustness of the control is tested by varying the operating conditions and looking if the controllers can converge. To see how well the controller handles the addition of biofuels, ethanol and biodiesel are added to the primary reference fuels and the ILC performance is tested. The ILC biofuel performance is then compared to the baseline proportional-integral controller again.

Chapter 2

Background

An overview of the fundamental topics discussed in this study are given in this chapter. A short summary of previous research pertinent to this study is also given.

2.1 HCCI

The HCCI cycle utilizes the compression of the engine to ignite the charge, similar to the Diesel cycle, rather than using a electrical discharge which is used in the spark ignition cycle. However, like the spark ignition cycle, in the HCCI cycle the fuel mixes with air to make a homogeneous charge before ignition occurs. This allows for a much faster combustion than either spark ignition or Diesel Oakley et al. [2001]. The fast combustion observed by HCCI has a near constant volume pressure rise that allows the cycle to more closely mimic the Otto cycle Heywood [1988] which has the maximum efficiency possible for an internal combustion engine. Because the ignition is caused by the compression of the already mixed charge, the combustion timing is a function of the chemical kinetics Najt and Foster [1983]. The chemical kinetics determine the combustion so interesting mechanism can be seen in HCCI like a low temperature heat release Kelly-Zion and Dec [2000] and an intermediate temperature heat release Yang et al. [2010] that depend largely on the fuel. With the fast combustion, high pressure rise rates occur which may cause damage to the

engine Oakley et al. [2001]. To reduce the pressure rise, HCCI is often run with either large air to fuel ratios or by diluting the charge with recirculated exhaust gas (EGR). This reduces the torque of the engine but also decreases the temperatures observed in the cycle Warnatz et al. [2006]. This low temperature reduces the amount of NO_x produced Warnatz et al. [2006] but also causes lower temperatures to occur later in the cycle which is known to increase uHC and CO emissions Stanglmaier and Roberts [1999]. Since HCCI timing is dependent on the properties of the fuel, two methods have been used to predict the combustion timing of fuel in HCCI. They are chemical kinetic modeling and empirical combustion metrics.

2.2 Fuel Properties

2.2.1 Volatility

Volatility is the tendency for a fuel to evaporate. It is characterized by Taylor and Taylor [1961]:

$$F_v = \frac{m_{fv} p_f}{m_a (p - p_f)} \tag{2.1}$$

where

$$\begin{aligned} F_v &= \text{mass ratio of evaporated fuel to air [-]} \\ m_{fv} &= \text{average molecular weight of fuel vapor [g/mol]} \\ p_f &= \text{partial pressure of the fuel vapor [Bar]} \\ m_a &= \text{molecular weight of air [g/mol]} \\ p &= \text{total pressure of mixture [Bar]} \end{aligned}$$

The vapor pressure of the fuel is dependent on the temperature and fuel type,

$P_{vap} = P_{vap}(T, \text{Fuel})$.

The volatility has two affects on engine performance Taylor and Taylor [1961]. One is the minimum temperature the fuel can start at. This is the temperature that the fuel cannot evaporate to the minimum air fuel ratio required for combustion. As well if it is too volatile it may cause vapor lock.

Volatility is required to mix the fuel with the air. The fuel must be volatile enough to reach a homogeneous mixture.

2.2.2 Heat of Combustion

Heating value is the energy released when the fuel is combusted Smith and Stinson [1952]. It can be affected by many things, such as if it is combusted at constant pressure or constant volume, if the water produced condenses or not, and what temperature the reaction occurred at. When the water condenses this is known as the Higher Heating Value (HHV) and when it does not it is known as the Lower Heating Value (LHV).

While it would seem that having a higher specific heating value is ideal, one issue can occur due to the need for oxygen. Some fuels require a higher air to fuel ratio, this can decrease the heat value density in the combustion chamber therefore negating affects the higher heating value had with respect to cycle analysis.

2.2.3 Heat of Evaporation

Heat of evaporation is the energy required to change the fuel from a liquid to a gaseous phase. This can dramatically change the mixture temperature compared to the intake temperature Taylor and Taylor [1961]. This change can be ideal it can cool the charge allowing for a higher density.

Table 2.1: RON and MON operating conditions ASTM [1968].

Factor	MON	RON
Inlet Temperature	300 F°	125 F°
Speed	900 rpm	600 rpm

2.2.4 Chemical Stability

This aspect of the fuel is for practical purposes. If a fuel degrades quickly it may not be ideal as a fuel for internal combustion engines Taylor and Taylor [1961]. If it corrodes metals or plastics it would require specialized delivery system. Its safety precautions should also be considered when choosing a fuel for consumers.

2.3 Combustion Metrics

2.3.1 Octane Rating

Detonation is often characterized by the octane number (ON) Taylor and Taylor [1961]. This is its tendency to knock compared to iso-octane and n-heptane mixture which is called a Primary Reference Fuel (PRF). A fuel with 100 ON knocks like iso-octane and a fuel with 0 ON knocks like n-heptane. There are two definitions of ON: one being research octane number (RON) and the other being motor octane number (MON). The difference are the operating conditions which are given in Table 2.1.

A fuel with a higher ON is more resistant to knocking. The sensitivity is the difference between the MON and RON and characterizes how sensitive the fuel is to operating condition changes.

To measure ON for a particular fuel, a Cooperative Fuels Research (CFR) engine is operating at the desired conditions for either MON or RON ASTM [1968]. The compression ratio is then altered until knocking is achieved. Then a PRF mixture is prepared that matched the knocking intensity observed by the test fuel. The PRF mixture by volume of iso-octane to n-heptane percentage is taken as the ON.

Fuel Sensitivity is the difference between MON and RON; it is used to indicate how sensitive the fuel is to operating conditions, particularly the inlet temperature. Fuels that are more paraffinic tend to have less fuel sensitivity Lichty [1951].

ON is very dependent on fuel structure and the burn process. Since ON is a measure of the tendency to knock, the knocking mechanism must first be understood. Knocking occurs after the fuel is initially ignited. As the flame front expands through the combustion chamber, the burnt charge expands and compresses the unburnt charge. If the unburnt charge detonates (autoignites) before the initial flame front reaches it, the new combustion zone increases in pressure. This will then cause a large pressure gradient since the old burnt charge has begun expanding and thereby lowering its pressure. The pressure gradient then oscillates causing the characteristic pinging sound of knock. These pressure waves can strip the thermal boundary layer off the combustion chamber allowing excessive heat transfer to the cylinder walls and piston that can damage the engine and reduces efficiency Lichty [1951].

With this knowledge of knocking, fuels can be characterized on their tendency to knock by their detonation characteristics. Combustion is a summation of many elementary reactions Smith and Stinson [1952]. These elementary reactions, when in the context of combustion, are categorized as chain branchers and chain breakers. Chain branchers cause an increase in the radicals used to begin the reaction thereby cause a positive feedback effect. Chain breakers use up the radicals used in the reaction therefore ending the chain. Detonation occurs when the number of chain branchers out numbers the chain breakers causing a rapid reaction Smith and Stinson [1952]. For molecules to begin reacting, they must collide with enough energy to break their initial bonds. For a long chain hydrocarbon this is initially difficult. But after the first hydrogen is stripped away, an alkyl radical is left. These oxidize easily and the process of stripping the carbons and hydrogens off begins causing chain branching. Due to this characteristic, longer and straighter (less branches) hydrocarbons react

more readily as less initial alkyl radical formation has to occur Lichty [1951].

This gives long straight chain molecules like n-heptane a low ON since it reacts more readily, and iso-octane, a compact shorter chain molecule with lots of branches, a high ON since it is more difficult ignite and has a longer ignition delay.

Kalghatgi proposed that the knock limiting spark advance, KLSA was linearly dependent on the RON and MON of the fuel at a given operating point Kalghatgi [2003].This can be written as:

$$KLSA = c + a\,RON + b\,MON \tag{2.2}$$

Rewriting eqn. 2.2 by substituting in Octane Index, OI, and K, gives the following:

$$KLSA = c + (a+b)OI \tag{2.3}$$

$$OI = (1-K)RON + K \cdot MON \tag{2.4}$$

The value K should only be dependent of operating conditions. These equations characterized the experiment well in Kalghatgi [2003] with R^2 value of 0.97. From eqn. 2.4, it can be seen that if K=1 the OI will equal the MON of the fuel. This corresponds to the engine parameters that will simulate knocking conditions similar to the ones produced by the MON ASTM test seen in ASTM [1968]. Similarly if K=0, it will be equivalent to RON. Kalghatgi also noted that the K maybe negative. If it is then a fuel with a large difference sensitivity, S, can have a higher OI and therefore be more resistant to knocking. These results show that RON and MON have enough information to characterize a fuels auto-ignition quality in SI engines and the only other parameters needed to predict knocking are the operating conditions.

2.3.2 Octane Rating for HCCI

Kalghatgi then proceeded to apply this method to HCCI, with the following change Kalghatgi [2003]:

$$CA50 = aRON + bMON + c \tag{2.5}$$

Where CA50 is crank angle after top dead center where 50% of the fuel is burnt. Eqn. 2.5 can be manipulated similarly to eqns. 2.3 and 2.4. Here Kalghatgi is stating that the RON and MON are also enough information to characterize the fuel's auto-ignition characteristics in HCCI and the only other information needed is the operating conditions to predict the CA50 of the test. The results proved quite good with R^2 values of 0.89 and 0.96 with CA50 vs. OI Kalghatgi [2003]. However he did later show that for one of the operating conditions, a quadratic fit worked better, this indicates that the relationship is more complicated or other fuel factors must be involved. Risberg et al. went on to compare the OI_0 of different operating conditions Risberg et al. [2003]. The value OI_0 is the required OI that at a set of operating conditions, would result in a CA50 of 0 crank angle degrees after top dead center. It was found that OI_0 could be described by the $T_{maxcomp}$, $P_{maxcomp}$, λ, and RPM. This relationship is found using PRFs only. Then a new fuel is run at different operating conditions and through the use of the equation derived from PFR's, the OI and how it changes with respect to operating conditions can be found. In Risberg et al. [2003] they also predicted K with respect to T_{comp15} and λ. It is noted that the subscripts *comp15* relates to to the temperature of compression at 15 bars and *maxcomp* refers to the maximum compression both which can be found through thermodynamic relations. In Kalghatgi and Head [2004] the relations of K and OI_0 were similar to that found in Risberg et al. [2003] showing that engine geometry may not play a significant role. The results were also extended; Since OI_0 and K both depend on T_{comp15},

if a fuel had a particular RON and MON value, it is theorized that the fuel would always ignite at top dead center if the λ and speed were kept constant, no matter what T_{comp15} is used. Another extension is that sensitive fuels are better for HCCI because if the load increases, the K value will decrease and if it is negative this will increase the OI for highly sensitive fuel thereby making it resistant to knock.

2.3.3 Other Proposed Metrics

Shibata stated that OI was not sufficient for HCCI Shibata [2007]. His indexing was based of the fuel's components which is more useful with naphthas and the auto-ignition of the High Temperature Heat Release (HTHR) based off of its low temperature reactions is compared. Intake air heating is used to show these results. The octane number at different operating points by scaling their HTHR CA20s with that of iso-octane and n-heptane is described. For example, if at a certain operating condition 20% of the high temperature heat release happens at -10 CAD for n-heptane and 0 CAD for iso-octane, then if a fuel had its at -5 CAD its new ON would be 50. By plotting the new ONs vs intake temperature it is seen that at high temperatures the fuels tend to move towards 100 ON. This is attributed to iso-octane having neither a LTHR or a LTHR inhibitor. Shibata stated that the fuels below 100 ON have a LTHR with n-heptane having the largest LTHR. Any that were above 100 ON had low temperature reactions that caused chain breaking radicals to occur thereby reducing any low temperature heat release and delaying ignition. As intake heating increases, these low temperature reactions become negligible as the heat from LTHR does not contribute as much to combustion making the fuel tend to a neutral position best described by iso-octane.

The combustion timing is correlated with the amount of low temperature heat release (LTHR) Shibata et al. [2005]. An indexing based off of the required compression ratio for constant combustion phasing is developed Truedsson et al. [2014]. The

method provided cannot go below a RON of 60 due to a quadratic regression.

While all these methods have their benefits, none can predict CA50 for all fuels Rapp et al. [2013]. It has also been found that a different mode of combustion, called intermediate temperature heat release (ITHR), can also affect the combustion timing Vuilleumier et al. [2014] Yang et al. [2010].

2.4 Predicting Properties Based of Chemical Structure

2.4.1 Enthalpy of Formation

The enthalpy of formation (Δh_f^0) is the energy required to create the compound from its base elements, which are defined to have enthalpy of formations of 0. If the enthalpy of formation of each compound in a chemical reaction are known then the heat of the reaction can be found. One can find the heating value of a fuel if the enthalpies of formation are known for that fuel, water and carbon dioxide. O_2 is not needed as it is defined as 0. This process is shown below using it on methane:

$$CH_4 + 3O_2 \rightarrow CO_2 + 2H_2O \tag{2.6}$$

$$\Delta h_{reaction} = \Delta h^0_{f(CO_2)} + 2\Delta h^0_{f(H_2O)} - \Delta h^0_{f(CH_4)} - 3\Delta h^0_{f(O_2)} \tag{2.7}$$

In eqn. 2.7 the $\Delta h_{reaction}$ is the molar heating value of methane due to it being a combustion reaction.

To estimate the enthalpy of formation, a group contribution method can be applied Poling and Prausnitz [2001]. Joback's method is one such, where the groups are defined by their central atom, how many hydrogens are attached and their bonds to the other groups. For example propane, C_3H_8, has 2 -CH_3 groups and 1 >CH_2. This method's advantage is its simplicity and the only requirement is the compound's

structure. This method was applied by Lapuerta to estimate the enthalpy of formation of methyl and ethyl esters Lapuerta et al. [2010]. This method was also applied to ether biofuels created by the University of Manitoba. The structures of these fuels are given in Fig. 2.1. The groups required for the estimation of these biofuels are given in Table 2.2. The values are used in the following:

$$\Delta h_f^0 = 68.29 + \sum_i N_i J_i \tag{2.8}$$

where:

$$N_i = \text{Number of groups}$$

$$J_i = \text{Groups contribution}$$

The enthalpy of formation for the C8 and C10 fuels were found to be -519.45 kJ/mol and -560.73 kJ/mol respectively. These are then used to find the lower heating value (as the water is assumed to be gaseous form) to give values of -6075.65 kJ/mol and -7305.02 kJ/mol of C8 and C10 fuels, respectively.

Testing using a bomb calorimeter was done to experimentally find these values. The results of the testing gave values of -6611±307 kJ/mol and -7671±368 kJ/mol for the C8 and the C10 fuels respectively. The C10 estimate is within error of the experimentally found value while the C8 value is not. The C8 value has an 8% error which is still considered to be good considering the testing apparatus was unable to account for heat loss to the environment due to the large resolution of the temperature measurement and the estimation was using the simplest group contribution possible.

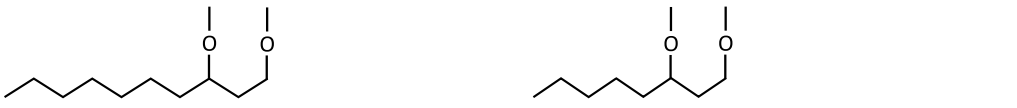

(a) 1,3-dimethyl ether decane (C10). (b) 1,3-dimethyl ether octane (C8)

Figure 2.1: Biofuels' structures that are created at University of Manitoba

Table 2.2: Values of group contribution for enthalpy of formation Lapuerta et al. [2010].

Group	Contribution
-CH_3	-76.45
-CH_2-	-20.64
-CH<	29.89
-O-	-132.22

2.4.2 Enthalpy of Vaporization

To estimate the enthalpy of vaporization, Jia used a positional distributive contribution method Jia et al. [2010]. This method is similar to Joback's method with the addition of what each group is bonded to and the location of particular groups are accounted for. An example of this is done with ethyl isobutanoate Jia et al. [2010], shown in Fig. 2.2. The position groups are as follows:

1. 1 C-$(CH_2)(H)_3$
2. 2 C-$(CH)(H)_3$
3. 1 C-$(C)_2(CO)(H)$
4. 1 C-$(C)(O)(H)_2$
5. 1 CO-(CH)(O)
6. 1 O-$(CO)(CH_2)$

The groups indicate what the central atom is and what it is attached to and the number in front is how many groups there are in the molecule, e.g. there are 2 group

2's which are a carbon atom attached to three hydrogens and a carbon atom which only has 1 hydrogen attached to it. These groups are used in the following equation:

$$\Delta_{vap}H = \Delta_{vap}H_o + \sum_i A_i N_i + \sum_j \tanh(N_j/N) + \sum_k A_k P_k + a_1\, e^{1/M} + a_2\, e^{1/N} \quad (2.9)$$

where:

N = Total number of groups.

i = Index corresponding to number of groups with saturated carbon as central atom.

j = Index corresponding to number of groups without saturated carbon as central atom.

k = Index corresponding to number of groups with position corrections.

A = Contribution value.

P = Position of group.

M = Molecular weight.

$\Delta_{vap}H_o$ = Offset value.

$a_{1\&2}$ = Coefficients.

In the example = 7, $i \in [1,5]$, $j \in [1,2]$ and Pz for the CO group would be 3. $\Delta_{vap}H_o$, a_1, and a_2 have predetermined values of 2.359, 55.293 and -25.335 respectively.

Jia compared this method to multiple other ones and found it did quite well for estimating the enthalpy of vaporization for 311 molecules, especially when compared to Joback method Jia et al. [2010]. This method was applied to the C8 and C10 fuels and found to give values of 51.57 kJ/mol and 56.97 kJ/mol. The groups required to do this calculation are given in Table 2.3.

Table 2.3: Values of group contribution for enthalpy of vaporization Jia et al. [2010].

Group	Contribution
C-$(CH_2)(H)_3$	-3.786
C-$(C)_2(H)_2$	1.965
C-(O)$(C)_2$(H)	10.908
C-(C-O)$(H)_3$	2.277
C-(O)(C)$(H)_2$	7.350
O-$(C)_2$	-51.222
>(CH) Position factor	0.247

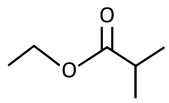

Figure 2.2: ethyl isobutanoate.

2.4.3 Octane Number

A combination of Joback's and positional distributive contribution method was applied to estimating the RON and MON of paraffins, olefins, cyclic and aromatics Albahri [2003]. Albahri setup a Joback's method and added functional groups that accounted for distances between branches.

For ON estimation the following formula was created as it produced the best results Albahri [2003]:

$$\begin{aligned} \mathrm{ON} = a + b\left(\sum_i \mathrm{ON_i}\right) + c\left(\sum_i \mathrm{ON_i}\right)^2 + d\left(\sum_i \mathrm{ON_i}\right)^3 \\ + e\left(\sum_i \mathrm{ON_i}\right)^4 + f\left(\sum_i \mathrm{ON_i}\right)^{-1} \end{aligned} \tag{2.10}$$

The $\sum_i \mathrm{ON_i}$ terms are the summation of the functional groups values in the associated pure compound hydrocarbon. Some of the functional group values are given in Table 2.4.

In Table 2.4 only paraffins are includes as these will be the only functional groups that will be used in ON prediction later on. The coefficients to be used with eqn. 2.10

Table 2.4: Group Contribution for Estimation of the Octane Number Albahri [2003].

HC type	serial no.	group	RON	MON
paraffins	1	$-CH_3$	0.459	0.491
	2	C_2H_5	0.948	0.517
	3	$>CH_2$	0.680	0.722
	4	α^a >CH–	-0.139	-0.430
	5	β >CH–	-0.362	-0.186
	6	γ >CH–	-0.358	-0.768
	7	α >CH<	-1.357	-1.983
	8	β >CH<	-1.828	-12.88

[a] α, β, and γ refer to the second, third, and fourth positions on the HC chain, respectively.

Table 2.5: Coefficients for eqn. 2.10 Albahri [2003]

octane no.	use with Table	a	b	c	d	e	f
RON	2.4	104.8	-5.395	6.532	-5.165	0.6189	-0.0037
MON	2.4	84.04	1.84	-1.452	-0.357	-0.0179	0

are given in Table 2.5. This method is found to have a correlation coefficient ranging from 0.975 to 0.84 and a maximum deviation between predicted ON and experimentally found ON of 48 with the average deviations ranging from 5 to 8 Albahri [2003].

This same method can be applied to the biofuels, shown in Fig. 2.1, created by the University of Manitoba. The biofuels are diethers and since ether functional groups are not included in the prediction method, their values must be ascertained. This required the non-linear regression to be re-done so that the coefficients in Table 2.5 can fit the oxygenated fuels better.

The majority of fuels' octane number are found from API [1968]. The oxygenated fuels are found from Eglof, Gusftav And Arsdell [1941]. Some fuels could not be used as they required a functional group used by no other fuel. This over defines the system for the non-linear regression and gives an ill-defined Jacobian when solving. With regards to the ethers only some are used as the values presented in Eglof, Gusftav And Arsdell [1941] are of a blended compound. They are mixed at 25% vol.

with a 74 ON aviation fuel. Since ON is not linear when blended F. H. Garner, E. B. Evans, C. H. Sprake [1933], the only values that are taken are ones that are within 12 ON of 74 ON so that a linear extrapolation will give minimal error.

Eqn. 2.10 is used in Matlab's non-linear regression formula to find the weights of coefficients and functional group contribution. These values are shown in Tables 2.6 and 2.7. The resulting system is found to be very flat. In Fig. 2.3 the results of the regression are shown by comparing the predicted and actual values. For validation, 39 and 40 fuels are taken from the RON and MON sets, respectively, and are not used in the regression. This ensures that the regression does not "over-fit" the data and accurately represents the system. An analysis of the results is given in Table 2.8. This shows that the validation data is comparable to the data used for the regression.

When comparing the results to Albahri [2003], the fit obtained in this study is not as good. This may be due to the addition of oxygenated fuels, or the fact that some groups are neglected in this study. This is from not enough fuels contained these groups. Further investigation needs to be done on the structure effects of the system and if a more positional distributive group contribution should be used.

The values obtained are then applied to the biofuels. Alberta Innovates Technology Futures (AITF) did a RON test following procedure in ASTM [1968] using 10:1 mixture of iso-octane to biofuel. The results are 88.7 for C8 and 87.7 for C10. This is compared to results given from the regression, as shown in Fig. 2.4. The functional group for -O- does not exist for RON prediction so the MON -O- functional group value is used instead. The blend plots are assumed linear but since the mixture is close to 0% this assumption can still give accurate results. The predicted RON values are -11.9 and -28.7 which gives a predicted mixture strength of 89.8 and 88.3 for C8 and C10 fuels, both respectively, which strongly agrees with the values obtained from AITF.

Table 2.6: Functional group contribution values found from non-linear regression.

HC type	Functional group	$(RON)_i$	$(MON)_i$
Paraffins	-CH_3	-0.0327	0.8651
	-C_2H_5 branch	0.2041	0.9659
	>CH_2	0.3539	-0.8298
	α^a >CH-	0.1419	-1.5369
	β >CH-	-0.1052	-0.7070
	α >C<	-0.3145	-2.7885
	β >C<	-0.6014	-0.9706
Olefins	=CH-	-2.6930	0.7081
	>C=	-2.6730	-1.0141
	=CH_2	2.3976	1.7461
	=CH- cis	-0.1973	0.0791
	=CH- trans	-0.2823	0.2070
	≡CH	-1.0985	NA
	≡C-	-0.0229	-1.669
Cyclic	>CH_2	0.0939	-0.2027
	>CH-	0.1827	-0.5613
	>CH- (o)	-0.2057	-0.3570
	>C<	4.4030	13.2212
	=CH-	-0.1371	0.0118
	=C-	-0.1543	-0.3699
	C3 corr	-0.7919	8.3049
Aromatics	=CH-	-2.5480	2.0614
	-C=	11.7227	0.6863
	-C= (o)	-2.1602	1.3045
	-C= (m)	-2.9424	1.5313
	-C= (p)	-2.5744	1.2973
	OH	4.6837	10.9525
	O (non-ring)	NA	0.0837
	>C=O (keton)	NA	1.5897

[a] α and β refer to the second and third positions on the HC chain, respectively.

Table 2.7: Coefficients for eqn. 2.10 found from non-linear regression.

Octane Type	a	b	c	d	e	f
MON	76.9442	8.7299	-3.737	0.4847	-0.0183	0.0018
RON	93.1085	-31.6944	-11.8588	1.4722	0.5003	0.1399

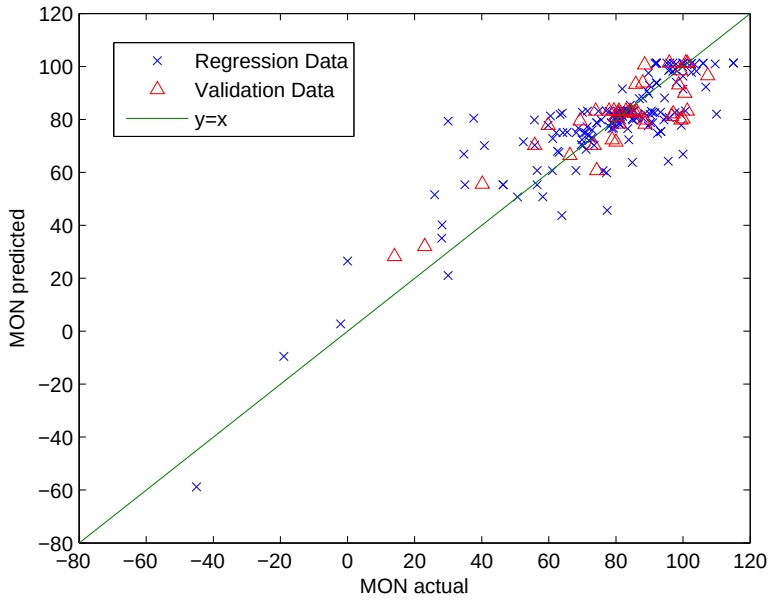

(a) Motor

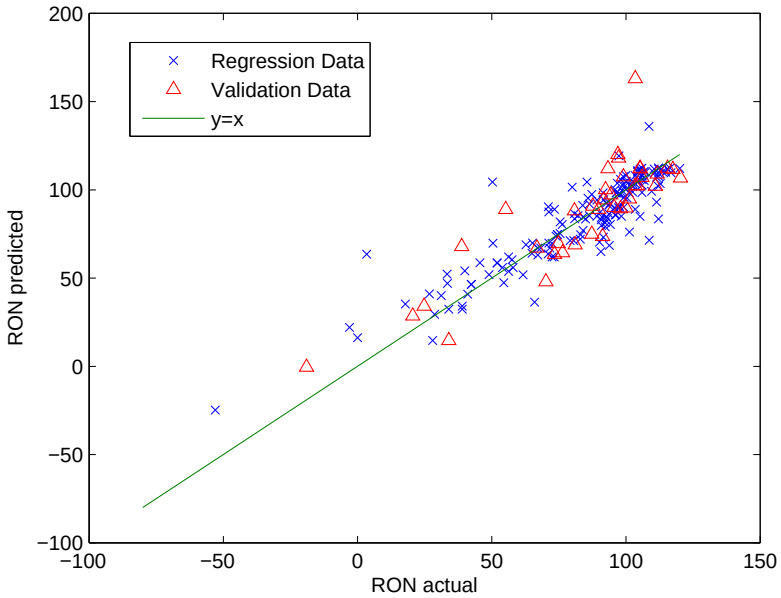

(b) Research

Figure 2.3: Predicted vs. actual ON values obtained from non-linear regression.

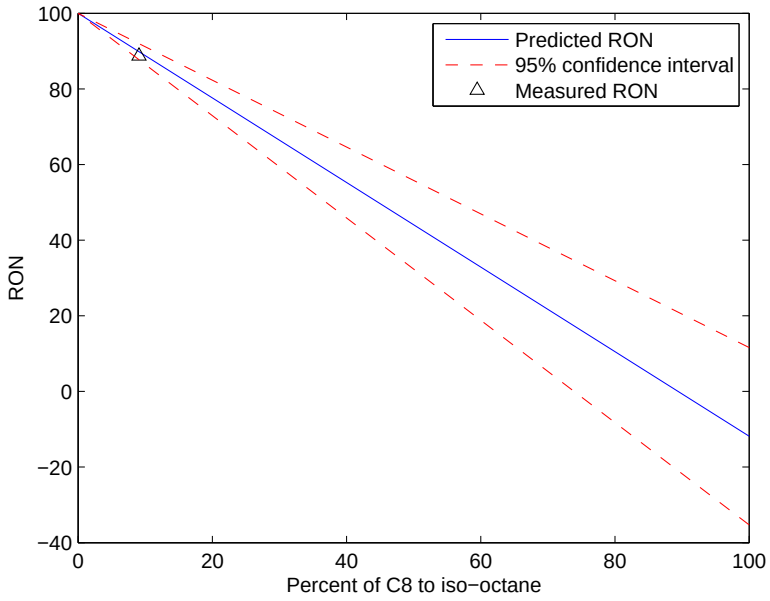

(a) 1,3-dimethyloxyoctane

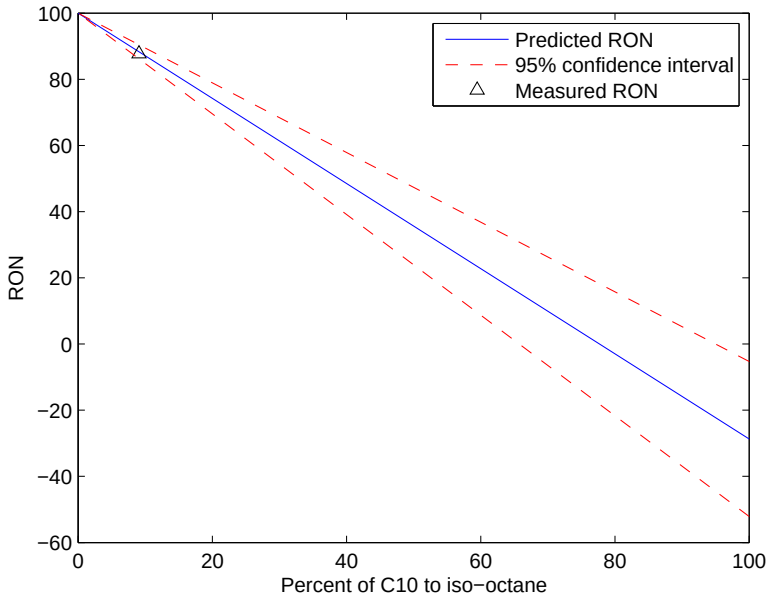

(b) 1,3-dimethyloxydecane

Figure 2.4: Blend plots assuming linear trend and comparison of predicted vs measured RON values of biofuels.

Table 2.8: Results from non-linear regression.

Octane Type	Correlation coefficient	Average residual	Max residual
MON	0.861	7.63	49
MON validation	0.874	7.86	19
RON	0.901	7.97	60
RON validation	0.863	11.5	59

2.4.4 Combustion Modeling

The combustion event can be modeled by solving the set of differential equations describing the reactions that occur in the combustion Warnatz et al. [2006]. The amount of reactions can vary from 100 reactions Kirchen [2004] for a skeletal model to several thousand Slavinskaya and Haidn [2003] for a detailed model. Depending on the goal of the model, the number of zones in the combustion chamber can also be varied, with a single zone simulating combustion timing well Aceves et al. [1999] while a multi zone is needed for combustion duration or emissions Flowers et al. [2002]. Combustion modeling and experiments have been used to show the effects EGR has on HCCI in Zhao et al. [2001] and Atkins [2004] by four main aspects: charge heating, thermal property change, dilution and chemical additions. Charge heating's effect is equivalent to heating the intake and advances the combustion timing. The change in thermal properties, like the increase in heat capacity, by the addition of EGR delays combustion by lowering the temperatures observed and therefore delays combustion. The dilution effect lowers the reactants' concentrations and delays the combustion timing. The chemical species from exhaust gases that have not completely reacted adds either active radicals or high energy compounds like CO or uHC which advance reaction time. The predominant effects are found to be the charge heating and the thermal property effects Zhao et al. [2001].

For combustion modeling the chemical kinetics are needed Warnatz et al. [2006]. This has been done for primary reference fuels Kirchen [2004], natural gas Aceves

et al. [1999] and many others. These models are difficult to develop and many fuels are not available. For gasoline, that can contain as many as 1000 compounds Smith and Stinson [1952], the ability to accurately model and predict HCCI combustion properties, like timing, is very difficult.

2.5 Control

2.5.1 Previous Control Strategies

Instead of trying to predict combustion timing, feedback controllers can be used to control combustion timing in HCCI. Many control strategies have been implemented. These include intake temperature control Chia-Jui Chiang et al. [2012], valve control Yeom et al. [2007], and fuel control Bidarvatan and Shahbakhti [2013]. Intake temperature is found to have long time delays and require large amounts of energy to implement Aceves et al. [2001]. Valve control works by utilizing the internal EGR to effect the timing of next cycles timing and has been found to be effective Ebrahimi and Koch [2015]. Dual-fuel control uses two fuels with different combustion reactivity. By changing the proportion of fuel injected, the combustion timing can be altered while the total amount is used to dictate the load of the engine. A control strategy must be implemented like MPC Ebrahimi and Koch [2015], or PI Strandh et al. [2004] to so that the timing can be kept constant while the load is set to its required value.

2.5.2 Iterative Learning Control

Iterative learning controllers are designed to find the ideal input for a specific trajectory. The ILC repeatedly attempts to follow a given reference trajectory. The error from this trajectory is compared to the system output and is used to design a new input. This new input is used on the system and the cycle repeats. By looking at the entire iteration at once, the input it able to anticipate aspects of the reference

trajectory before they occur. This allows the system to have ideally zero error when the ILC converges. Furthermore, only minimal system information is need Ahn et al. [2007a] and ILC has been known to work well on non-linear systems Jian-Xin and Tan [2003].

ILC is useful for repetitive processes, like robotics Parzer et al. [2015], and machining Fiorentino et al. [2015]. Several surveys have been done to highlight the current ILC knowledge and its strength and weaknesses Bristow et al. [2006] Moore et al. [2006] and Wang et al. [2009]. A norm-optimal control has been developed by Barton and Alleyne [2011] to provide control that has weightings on the system error, the inputs and the change inputs. Several papers have investigated its convergence and robustness using worst-case norm optimal Son et al. [2015], Linear Matrix Inequality (LMI) Gauthier and Boulet [2005] and Galkowski et al. [2003], and interval values Ahn et al. [2007b].

ILC have been analyzed in the frequency domain Wang et al. [2014] and using the "super vector" approach Ahn et al. [2007a]. The super vector approach treats the entire iteration's output as a single output vector as well as the input. This converts it into a Multi-Input Multi-Output (MIMO) system that operates through the iteration domain rather than the time domain.

ILC is very applicable for some automotive control due to its repetitive nature. These include electromagnetic valve control Tsai et al. [2012], and Diesel combustion control Hinkelbein et al. [2010]. Dooren [2015] used an ILC to control multiple aspects of an spark ignition engine. In Kapania and Gerdes [2015] a ILC was used for path optimization for an autonomous vehicle.

Chapter 3

Experimental Setup

This Chapter details the engine test cell, the system used to control certain aspects of the engine and the system used for data acquisition. As well it details the testing conditions and matrix functions used in the later chapters.

3.1 Engine Assembly

The test cell is a Waukesha CFR engine that is used for testing octane ratings of fuels in the ASTM standard testing procedures ASTM [1968]. This engine is ideal for testing biofuels as its primary use is for fuel testing. Since it is designed to withstand large amounts of knock, it is ideal for advanced combustion research. Minor adjustments have been made compared to the original including the replacement of the head for one with optical ports. This allows for installment of a Kistler piezoelectric pressure transducer for in-cylinder pressure and a thermocouple for jacket temperature. A schematic of the engine is given in Fig. 3.1 with a component list given in Table 3.1. The engine specifications are given in Table 3.2. In this table for valve timing the values are given in crank angle degrees with respect to either Top Dead Center (TDC) which is when the piston is at top of its respective stroke, or Bottom Dead Center (BDC) when the piston is at the bottom of its respective stroke. The prefix before indicates whether the it happens before, denoted with a "b", or after,

Table 3.1: Engine Description

Label	Description
1	Air Flow meter
2	Intake Plenum
3	Intake Heater
4	Throttle
5	Intake Manifold
6	Fuel Injectors
7	EGR valve
8	Combustion Chamber
9	Lambda Sensor

denoted with an "a" e.g. after top dead center becomes aTDC. The water cooling is set up by having the engine jacket in a water bath. This water evaporates to cool the engine then is condensed by coils supplied with tap water. This ensures the average temperature of the water bath is at the atmospheric boiling point at all times, which is found to be 97°C.

The dyno power is supplied by the original Waukesha dyno controller but RPM and load are controlled by a Digalog dynamometer controller.

Power for a the Tec-GT engine control unit, ignition, throttle and fuel pumps are supplied by an auto battery. As injectors are sensitive to supply voltage, a 6034A HP power supply set at 13.5 V is used to supply power to the injectors and other measurement systems.

There are 3 separate fuel systems. One for iso-octane, one for n-heptane and one for a test fuel. All 3 are designed the same but with the test fuel having a flow meter attached. The fuels are pressurized by the Walboro 255 LPH inline pumps with pressure regulated by a Aeromotive Universal Bypass Regulator with reference to the intake manifold. The injectors are low flow high impedance Accel injectors.

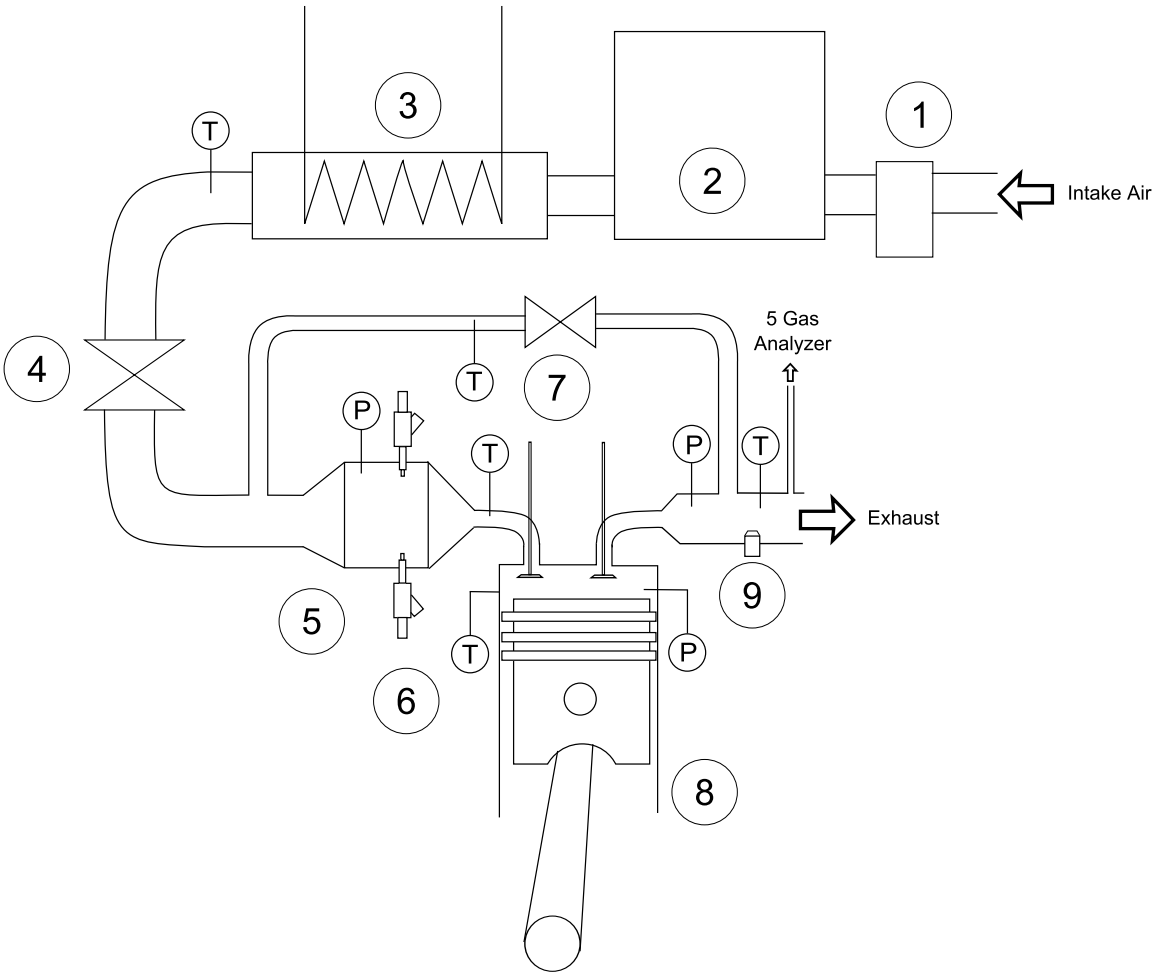

Figure 3.1: Engine Schematic

Table 3.2: Engine Specifications

Engine Parameter	Value/Type
combustion chamber	pancake with flat-top piston
engine type	water cooled
number of cylinders	1
displacement	612 cm^3
bore	82.6 mm
stroke	114.3 mm
compression ration	variable from 4 to 18
IVO	10° aTDC
IVC	34° aBDC
EVO	40° bBDC
EVC	15° aTDC

3.2 Engine Control System

To control spark and injection timing a Tec-GT engine control unit is used. This system is ideal as many of the controls can be changed on-line and only required the installation of a 60 tooth wheel on the engine crank and a CAM sensor. Even though it can control pulse width to two separate injectors, the secondary pulse width can only be set as a percentage of the first and therefore could not exceed the pulse width of the first. To allow for more fuel injection freedom an Arduino Due is used to control pulse widths of both injectors with use of a high power NPN transistor. The Arduino gets the injection timing from the Tec-GT as shown in Fig. 3.3, and then pulls each injector to ground for the time specified by the NI system, which will be discussed in the next section. The pulse width is communicated from the NI system to the Arduino using an 12-bit parallel signal for each injector. A schematic for this system can be seen in Fig. 3.2.

3.3 Data Acquisition

The Data Acquisition System (DAQ) has 3 NI DAQ cards using Labwindows/CVI software. This software allows for the DAQ system to be coded in C, with specialized libraries for communicating with the cards. Each card is used for separate set of analog inputs, depending on their type and acquisition rate. A list of how each measurement is recorded is given in Table 3.3.

The crankshaft has a 3600 pulse/rev encoder attached. This allows for the 0.10° digital signal to be used as a sampling clock for PCIe-6431. The z signal from the encoder, which occurs once every revolution, is sent through an AND gate with the CAM signal as shown in Fig. 3.2. This allows all data recording to trigger at precisely the same time every cycle, i.e. every two revolutions. This point is found to be 161.4° bTDC on the compression stroke. Each DAQ card uses this to begin recording data.

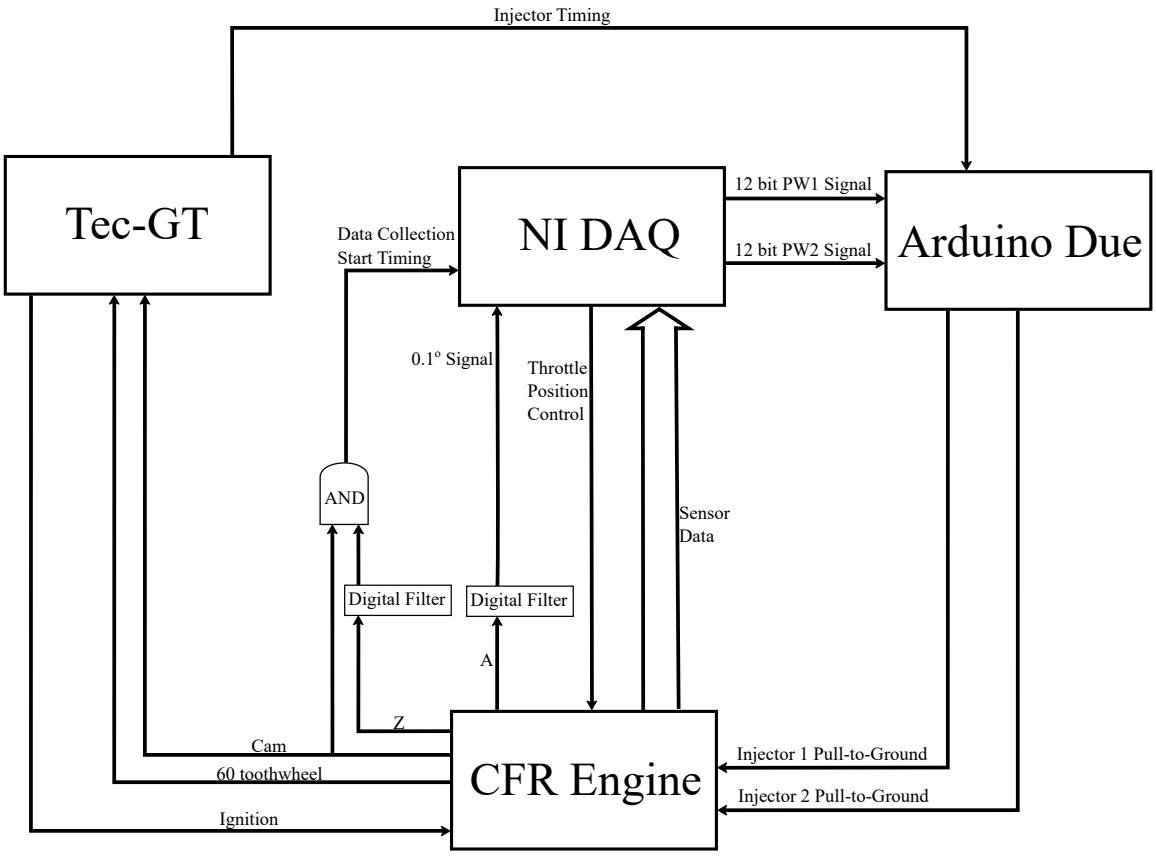

Figure 3.2: Engine Control Scheme

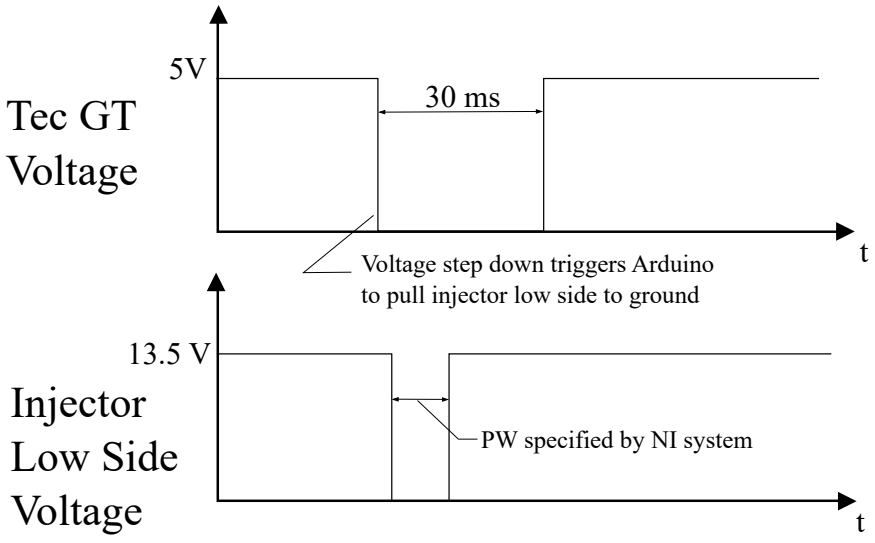

Figure 3.3: Tec-GT and injector voltages for injector timing control.

Table 3.3: DAQ cards with sampling rates and corresponding engine measurements.

Card	Sampling rate	Measurement
PCIe-6431	0.1°	in-cylinder pressure, intake pressure, torque
NI PCI-MIO-16E-1	100 Hz	fuel 1 pressure, fuel 2 pressure, exhaust pressure, air flow, lambda, throttle position, fuel flow
NI USB-6225	50 Hz	intake temperature, mixture temperature, coolant temperature, exhaust temperature, EGR temperature, cylinder wall temperature

This ensures that if need be, the time-based data can be resampled to crank-based for comparison using the speed of the engine. To allow the NI program enough time to calculate needed values before the next cycle occurs, only 3800 out of the possible 7200 data points are taken, i.e. 380 crank angle degrees. This allows the intake and in-cylinder pressure signals to capture everything from IVC and EVO which contains the compression stroke, combustion, and expansion stroke.

3.4 Sensors

This section lists the sensors used for measuring engine operating conditions. The uncertainty calculations for each measurement are calculated as in Moffat [1988] and are given in Appendix B. The single sample uncertainty is given as the error as the multi-sample uncertainty is dependent on the number of samples taken.

3.4.1 Pressure Sensors

The in-cylinder pressure sensor is a Kistler 6043A piezoelectric. The sensitivity is found from Handford [2009] and is tested to ensure that the sensitivity has not changed; the results are given in Appendix A. To convert the piezoelectric signal to a voltage a Kistler 507 Charge Amplifier is used. The single sample uncertainty is calculated as 321 kPa for in-cylinder pressure.

The intake, exhaust and fuel pressures use Validyne DP-15 pressure transducers. These are calibrated to find their sensitivity as given in Appendix A. They have operating ranges of ±86 kPa gauge and are measured with respect to the atmosphere therefore at the beginning of every test the atmospheric pressure is recorded using a mercury vertical barometer for reference. The accuracy is ±0.25%. The intake and exhaust pressure single sample uncertainty is calculated as 7.7 kPa and 0.59 kPa respectively.

3.4.2 Air Flow

Airflow is measured using a TSI 4235 laminar flowmeter. This system outputs a current rather than a voltage so a high precision resistor is used to convert it to a voltage for the DAQ system to measure. The meter has a range of 20 to 1000 L/min with an accuracy of ±2.5%

3.4.3 Lambda

Lambda ratio is measured using a LM-2 Innovate Motorsport Digital Air/Fuel Ratio with a wide-band Bosch oxygen sensor and has an accuracy of ±0.05.

3.4.4 Fuel Flow

The fuel flow for iso-octane and n-heptane is calibrated with respect to pulse width of the injector as discussed in detail later. Since flow rate is a function of both viscosity and density, this method is not practical for every fuel. Therefore a flow meter is attached to the test fuel tank to monitor flow rate. It is a Max Machinery 284-512 positive displacement piston flowmeter and transmitter and has an accuracy of ±0.2%.

Table 3.4: Thermocouple types used for temperature measurements.

Location	Thermocouple Type	Single Sample Uncertainty (°C)
Intake	J	5.9
Mixture	K	3.4
Coolant	T	1.9
Exhaust	T	2.7
EGR	J	7.2
Cylinder Wall	T	4.8

3.4.5 Temperatures

Temperatures recorded are intake, jacket, mixture, coolant, exhaust and EGR as shown in Fig. 3.1. The thermocouple type for each is given in Table 3.4 along with each thermocouple measurement single sample uncertainty. The DAQ card NI USB-6225 does not have an internal temperature measurement so a Texas Instrument LM-19 thermistor is used to find for the cold junction temperature for temperature conversion from voltage.

The intake temperature is controlled by an Omega CNi-852 temperature controller that activates an intake heater located at point 3 in Fig.3.1. The heater is powered by a 208 V 25 Amp custom power supply.

3.4.6 Torque

Torque is measured using a Durham Instruments load cell connected to the dyno. Measuring the moment arm from the load cell to the center of the dyno and multiplying it by load cell measurement gives the torque. The load cell is connected to a wheatstone bridge to measure the signal. The single sample uncertainty is found to be 0.20 Nm

Table 3.5: PXA-1100 Gas Analyzer specification.

Gas	Range	Resolution	Accuracy
uHC	0-20000 ppm	1ppm	6ppm or 5% of reading
CO	0-10%	0.01%	0.06% or 5% of reading
CO_2	0-20%	0.1%	0.5% or 5% of reading
O_2	0-25%	0.01%	0.01% or 5% of reading
NOx	0-4000 ppm	1ppm	32 ppm at 0-1000ppm
			60 ppm at 1001-2000ppm
			120 ppm at 2001-4000ppm

3.4.7 Emissions

For emission testing, a PXA-1100 Gas Analyzer Vetronix is used to test for unburnt HydroCarbons (uHC), NOx, CO, CO_2 and any unused O_2. The range and accuracy of each gas are given in Table 3.5.

3.5 Injector Calibration

The injectors work off a low side driver that a pull-to-ground setup operates on one side of the injector and the other side is attached to a 13.5 V power supply. The injector is turned on by closing the low side to ground and allowing current to flow through the injector. The pulse width is how long the low side is connected to ground. The injectors are calibrated to relate injected mass to injector pulse width. This is done by setting the pulse width, and injecting fuel into a container for 1000 injections then measuring the mass of the fuel injected. The mass per injection is then found by dividing the mass by the number of injections. Iso-octane and n-heptane are calibrated in this manner with results given in Appendix A. For other fuels, the flow rate is measured by the flow meter and correlated to the mass per injection by the engine speed and fuel density with the following formula:

$$\dot{V} = \frac{m_{inj}\text{RPM}}{2\rho} \tag{3.1}$$

with $\dot{V}$ being the volume flow rate measured by the flow meter, in mL/min, m_{inj} is the mass per injection in g, ρ is the fuel density in g/mL and RPM is the revolutions per minute of the engine. A 2 appears in the denominator since injection occurs every other engine revolution. The correlation between pulse width and m_{inj} is again done by measurement and a linear regression which gives the following relation:

$$m_{inj} = p_1\text{PW} + p_2 \tag{3.2}$$

where p_1 and p_2 are the regression coefficients and PW is the pulse width in ms. The inputs into the engine for control are injected energy of the fuel. To do this the Lower Heating Value, LHV, of the fuel is needed. The formula for relating the pulse width, which is controlled by the Arduino Due, to the energy injected, E_{inj}, is:

$$E_{inj} = \text{LHV}_{fuel}(p_1\text{PW} + p_2) \tag{3.3}$$

The calibration values of the injected mass and single sample uncertainties of the injected energy are given in Table 3.6. The injector calibration is detailed in Appendix A and the error calculation formulas are given in Appendix B.

Table 3.6: Injector calibration values and injection error.

Fuel	p_1 (g/ms)	p_2 (g)	Single sample uncertainty (J)
n-heptane	1.49×10^{-3}	-8.71×10^{-4}	6.3
iso-octane	1.57×10^{-3}	-1.04×10^{-3}	7.8
ethanol/iso-octane	1.42×10^{-3}	-1.12×10^{-3}	14.1
biodiesel/n-heptane	1.49×10^{-3}	-1.47×10^{-3}	47.3

3.6 Post Processing and Output Calculations

The in-cylinder pressure is used for measuring combustion properties. Since it uses a peizoelectric pressure transducer, the signal drifts. Therefore pegging the in-cylinder pressure is done every cycle using the intake pressure at IVC. This ensures that the in-cylinder pressure is equal to the intake pressure at IVC. An ensemble of 100 cycles of pressure traces is shown in Fig. 3.4. The confidence interval in Fig. 3.4 is a single sample uncertainty of each point using only the pressure trace deviation to show the range of cyclic variation.

The desired control system outputs are combustion timing and load of the engine. Two common metrics for these are crank angle when 50% of the fuel mass fraction is burned (CA50) and gross indicated mean effective pressure (IMEP). CA50 can be calculated from the pressure trace Heywood [1988] as:

$$dQ = \frac{\gamma}{\gamma - 1} P dV + \frac{1}{\gamma - 1} V dP + h_t (T_g - T_w) A_s \tag{3.4}$$

with Q being the chemical energy released from the fuel, γ is ratio of specific heats of the gas, P is the in-cylinder pressure, V is the in-cylinder volume, h_t is the heat transfer coefficient, T_g is the mean gas temperature, T_w is the wall temperature and A_s is the surface area of the cylinder. The heat transfer coefficient can be calculated using a modified Woschni correlation derived from Chang et al. [2004]. Eqn. 3.4

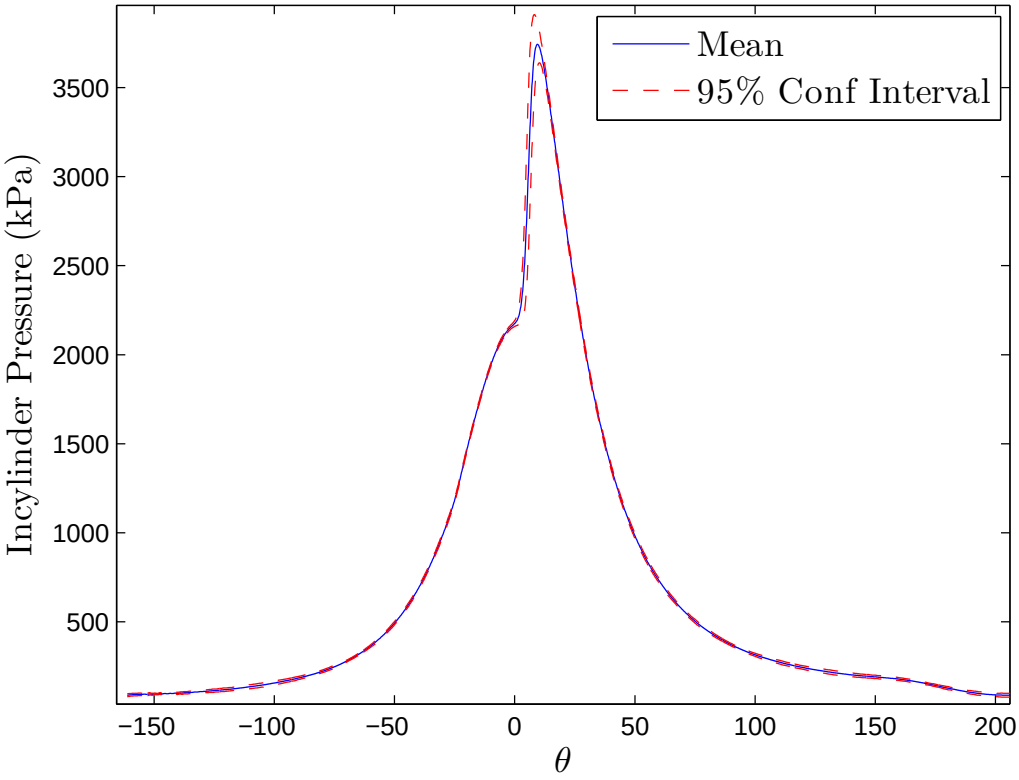

Figure 3.4: Ensemble of the pressure traces with HCCI.

assumes that crevice losses are negligible. Then CA50 is found by integrating dQ from IVC to EVO and finding θ when $Q(\theta) = Q_{max}/2$. Note: CA50 is given in crank angle degrees after top dead center of the compression stroke and will be denoted with "*deg*". Examples of dQ and Q are given in Figs 3.5 and 3.6.

Calculation of the heat loss to the walls is computationally expensive and CA50 is needed in real-time for control. To minimize calculation time, the last term in eqn 3.4 is ignored so CA50 can be calculated while the engine is running. The heat release plot for neglected heat transfer to the walls using the same pressure trace is also shown in Fig. 3.6. The comparison for 21 operating points with different CA50 mean of 100 cycles is given in Fig. 3.7. The on-line values are calculated while the engine is running and therefore do not include the modified Woschni heat transfer correlation while the off-line values do include the modified Woschni heat transfer correlation. The difference is a relatively constant increase of ≈0.5 deg when the modified Woschni heat transfer correlation is neglected and which is acceptable for control. The single sample uncertainty is found to be 0.25 deg and is detailed in Appendix B.

The IMEP of the cycle is a measure of how work is output from the cycle normalized by the engine displacement. It is calculated from:

$$\text{IMEP} = \frac{1}{V_d} \int_{IVC}^{EVO} PdV \tag{3.5}$$

with V_d is the displacement volume. The single sample uncertainty is found to be 27 kPa and is calculated in Appendix B.

Combustion duration is defined as CA20-80 similar to Shahbakhti [2009]. It is found from:

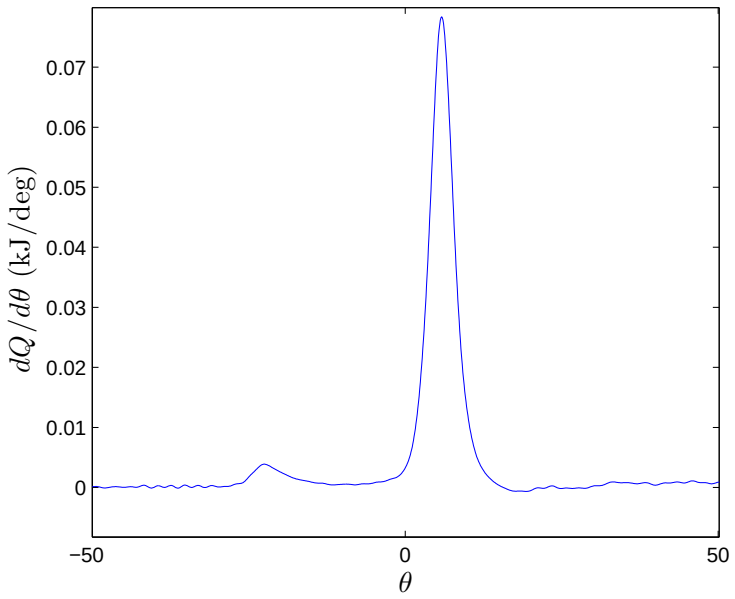

Figure 3.5: Heat release rate calculated from ensembled pressure trace.

$$\text{CA20-80} = \theta_{80} - \theta_{20} \tag{3.6}$$

where θ_{20} is θ when $Q(\theta) = 0.2Q_{max}$ and likewise for θ_{80}. By measuring from 20% of the total heat released it ensures that the LTHR is not included in the calculation.

The Coefficient Of Variation (COV) is found similar to Shahbakhti [2009] from:

$$\text{COV} = \frac{\text{std(IMEP)}}{\text{IMEP}} \times 100\% \tag{3.7}$$

with std signifying the standard deviation. This gives a measure of the consistency of combustion and if any misfires occur.

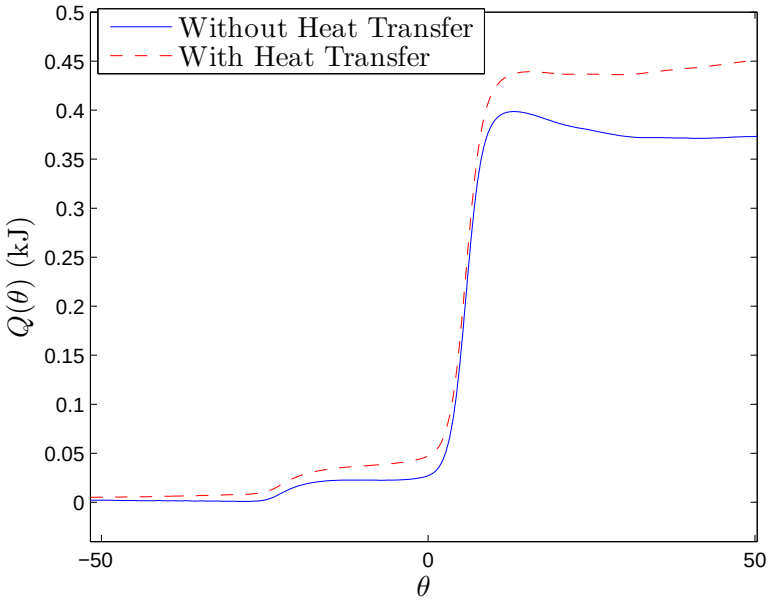

Figure 3.6: Total heat release from integrating heat release rate with and without the modified Woschni heat transfer correlation.

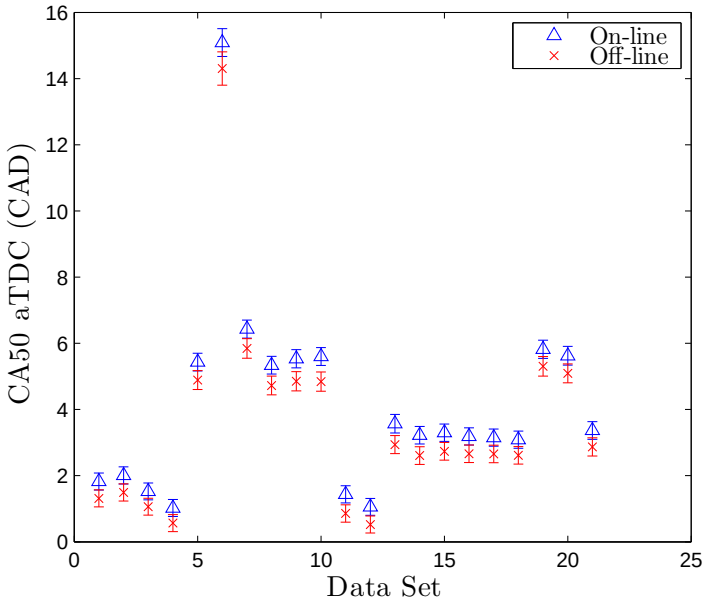

Figure 3.7: Online vs offline CA50 calculation.

3.7 Test Conditions

For designing and testing the ILC, a base operating condition is chosen as the values given in Table 3.7. To test the ILC robustness several other operating points are used. These operating condition changes are given in Table 3.8. For each operating point in Table 3.8, all other operating parameters are equivalent to their values in Table 3.7 other than the one indicated in Table 3.8.

Table 3.7: Base operating condition.

Parameter	Value
Intake Temperature	100°C
Intake Pressure	Atmospheric (92 to 94 kPa)
Speed	800 RPM
Compression Ratio	11:1
Fuel 1	n-heptane
Fuel 2	iso-octane

Table 3.8: Parameter changes from base operating condition for robustness testing operating points.

Operating point	Change from Base operating condition
1	Intake temperature decreased to 50°C
2	Intake temperature increased to 150°C
3	Compression ratio decreased to 10:1
4	Compression ratio increased to 12:1
5	Fuel 2 changed to 10% ethanol/90% iso-octane vol%
6	Fuel 1 changed to 10% biodiesel/90% n-heptane vol%

3.8 Reference Trajectory

The reference trajectories chosen for the ILC to follow is 60 combustion cycles with a step in IMEP then in CA50. The IMEP reference trajectory starts at 330 kPa then steps up to 370 kPa at cycle 20. For CA50, the reference trajectory starts at 3 deg then steps to 6 deg at cycle 40. These trajectories are given in Fig. 3.8. A step is used

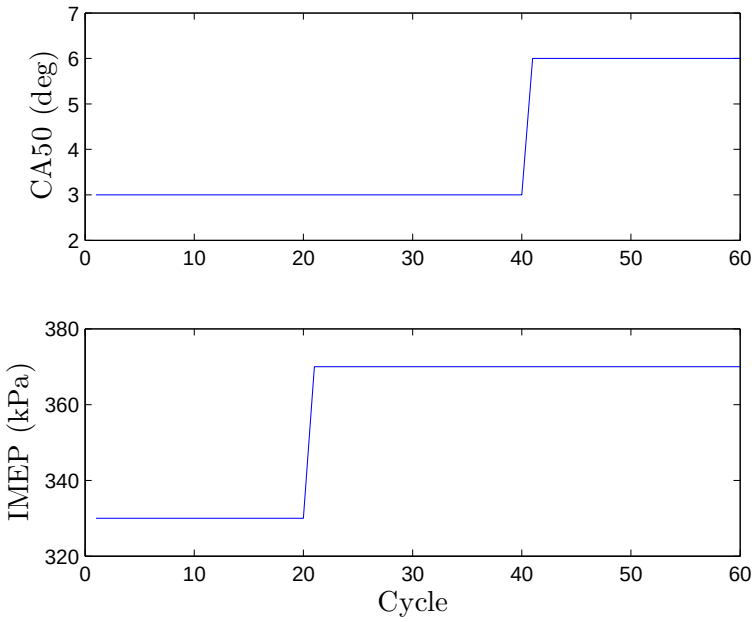

Figure 3.8: Reference trajectory to test controllers.

in both to illustrate the advantages of using an ILC as many feedback controllers have large initial errors when a step is implemented. The steps are separated so the effects of the step on each reference can be seen and without the other step complicating the response. This reference trajectory will be used for all tests so that the error norms can be compared without the need to normalize.

3.9 Matrix Function Definitions for ILC

Several matrix functions are used in the analysis of ILC systems. This section details the calculation of these functions. The spectral radius, $\rho(\cdot)$, of a matrix, $A \in \mathbb{C}^{n\times n}$, with eigenvalues of $\lambda_1,\ ...,\ \lambda_n$ is Golub and Van Loan [1996]:

$$\rho(A) = \max\{|\lambda_1|, ..., |\lambda_n|\} \tag{3.8}$$

Singular values of a matrix, A, are square roots of the eigenvalues of the matrix

A^*A where A^* denotes the adjoint of A Golub and Van Loan [1996]. The singular values are non-negative real numbers with the maximum being denoted by $\overline{\sigma}(\cdot)$ and the minimum being denoted by $\underline{\sigma}(\cdot)$. The maximum singular value of a matrix is similar to spectral radius, however they are not equivalent and some analyses, like matrix interval values, have only been proven with spectral radius and therefore both are used.

Matrix norms are extensions of vector norms for a matrix. Generally a norm, denoted with $||\cdot||$ is defined as:

$$||A||_p = \sup \frac{||Ax||_p}{||x||_p} \tag{3.9}$$

where $x \in \mathbb{C}^n$, $||x|| \neq 0$ and p is the chosen norm and is defined for vectors as:

$$||x||_p = \left(\sum_{i=1}^{n} |x_i|^p \right)^{1/p} \tag{3.10}$$

The $p = 2$ norm correlates to the vector length in Euclidean space $\mathbb{R}^n$. For matrices the 2-norm is the largest singular value Golub and Van Loan [1996], i.e. $||A||_2 = \overline{\sigma}(A)$. From here on $||\cdot||$ will denote the 2-norm of a matrix or vector to simplify the notation.

These properties of matrix 2-norms are used throughout this study Golub and Van Loan [1996]:

- $||A|| \geq 0$
- $||A|| = 0$ iff $a_{i,j} = 0 \ \forall \ i, j$
- $||\alpha A|| = |\alpha| \, ||A|| \ \forall \ \alpha \in \mathbb{R}$

- $||A + B|| \leq ||A|| + ||B||$
- $||AB|| \leq ||A||\,||B||$

with A, $B \in \mathbb{R}^{n \times n}$

Chapter 4

Iterative Learning Control Design and Implementation

This Chapter begins by characterizing the engine output responses in steady-state and dynamically. It then details iterative learning control designs and analyzes their response using analytics, simulation and experiment. It then compares the iterative learning control reference tracking to a traditional feedback controller

4.1 Domain Exploration

The operating domain of the engine is first explored to get a range of the inputs for which HCCI combustion is possible and to determine how the inputs, E_{hept} and E_{iso}, affect the outputs, CA50 and IMEP, in steady-state operation. With all other engine parameters being constant at the values given in Table 3.7, the amount of injected energy of each fuel, E_{iso} and E_{hept} , are swept through the operating domain resulting in 20 points as shown in Figs. 4.1 and 4.2. In these figures, the relationships between iso-octane, n-heptane, CA50 and IMEP can be inferred. Increasing n-heptane decreases CA50, while iso-octane has very little effect. From Kalghatgi [2003] the Octane Numbers, RON and MON, of a fuel can determine its combustion timing. This initially differs with the results shown in Fig. 4.1 as increasing E_{iso} should increase

ON and thereby decrease combustion timing. This effect is canceled out since the decreasing of λ retards combustion timing as well Hosseini [2008]. For E_{hept} these two affects add making CA50 very sensitive to E_{hept}. IMEP is increased when either of the two inputs, E_{hept} or E_{iso}, are increased, since IMEP is a measure of work output from the cycle.

There are 4 main limits to the operating domain. These are: (1) IMEP too high causing knock; (2) IMEP too low and engine could not maintain operating speed; (3) CA50 too early causing inefficient combustion; and (4) CA50 too late causing inconsistent combustion Shahbakhti [2009]. The knock limit is defined by Dec et al. [2011] as having a $dP/d\theta > 8$ bar/CAD. The limit is seen in Fig. 4.2 when the surface reaches 400 kPa as the $dP/d\theta$ is 7.5 bar/CAD. The system was not pushed past knock to avoid possible damage to engine. The three points near the knock boundary are $\{E_{hept}, E_{iso}\}$=$\{0.37$ kJ, 0.56 kJ$\}$, $\{0.39$ kJ, 0.53 kJ$\}$ and $\{0.41$ kJ, 0.49 kJ$\}$ resulting in an approximate domain limit of $E_{iso} + E_{hept} < 0.92$ kJ which is a diagonal line through the operating domain. The IMEP low limit occurs when the total fuel is too low and any decrease in either of the fuels will cause the CFR engine to slow down. This gives another approximate limit of $E_{iso} + E_{hept} > 0.70$ kJ which is also a diagonal line through the operating domain. The combustion timing limits on CA50 are set at 0 deg and 8 deg. They are set to these values as having a combustion timing before top dead center tends to decrease engine efficiency and too late can increase combustion inconsistency and decrease efficiency Shahbakhti [2009]. Steady-state combustion timing is dominated by E_{hept} . This translates to limits of n-heptane which are approximately 0.37 kJ $< E_{hept} < 0.41$ kJ.

Within the domain described, the steady-state responses of CA50 and IMEP for the engine are approximately linear. A 2-D linear regression for these 20 points is

performed giving:

$$\begin{bmatrix} \text{CA50} \\ \text{IMEP} \end{bmatrix} = \begin{bmatrix} -110 & 0.0445 \\ 464 & 492 \end{bmatrix} \begin{bmatrix} E_{hept} \\ E_{iso} \end{bmatrix} + \begin{bmatrix} 46.2 \\ -46.9 \end{bmatrix} \tag{4.1}$$

The regression has an R^2 equal to 0.965 for CA50 and 0.980 for IMEP. The parameters obtained by the regression in eqn. 4.1 are consistent with the above described mechanisms. The CA50 has a large negative sensitivity to E_{hept} and almost no sensitivity to E_{iso}. The IMEP has nearly equal sensitivity between E_{iso} and E_{hept}. The total steady-state standard deviation of CA50 and IMEP is 0.47 deg and 3.9 kPa, respectively. These values will be considered as the noise levels of their respectively signal.

The combustion duration is shown in Fig. 4.3. This figure shows the decrease in combustion duration as both E_{hept} and E_{iso} are increased. This is due to the increase in fuel concentration increasing the reaction rates Warnatz et al. [2006]. The COV for steady-state operation is shown in Fig. 4.4 and varies between 0.8 and 1.3 for 100 engine cycles. This figure shows that COV is relatively independent of E_{hept} or E_{iso} within the domain indicating no misfire occurs. An additional data point is taken with a CA50 of 15.1 deg and has a COV of 2.1. This point is outside of the operating range prescribed before but is used to highlight why the operating range was chosen as such. The increase in COV agrees with Shahbakhti [2009] in that later combustion becomes less consistent and would increase the COV of the system which would also increase the noise levels of the CA50 and IMEP.

4.2 System Identification

The transient response is modeled in this section. As discussed in Chapter 2 this can be done using detailed physics of the system; which is an on going research area. Here

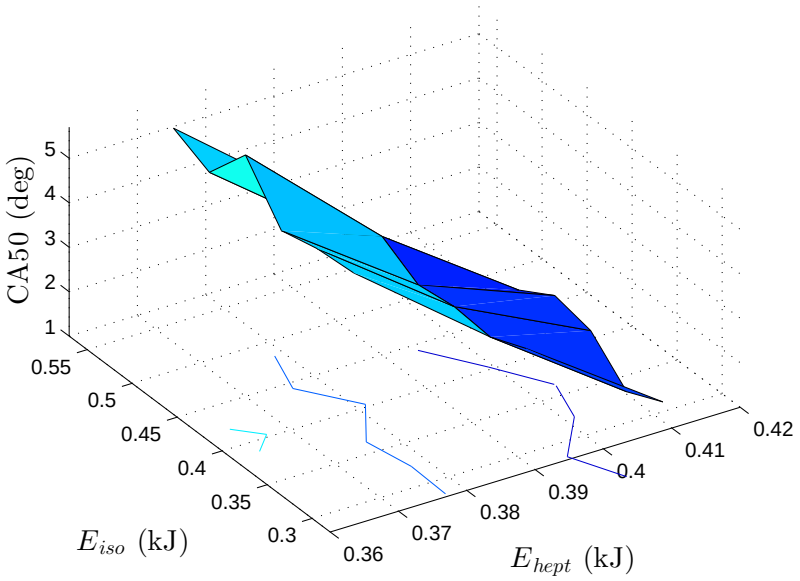

Figure 4.1: Steady-state combustion timing responses in HCCI with each point having a multi-sample uncertainty of 0.16 deg for varying iso-octane and n-heptane.

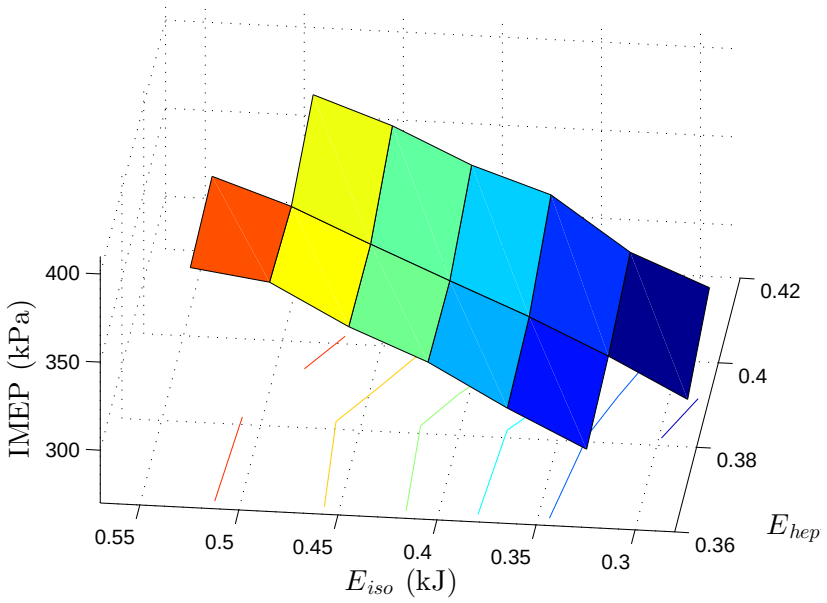

Figure 4.2: Steady-state IMEP responses in HCCI with each point having a multi-sample uncertainty of 14 kPa for varying iso-octane and n-heptane.

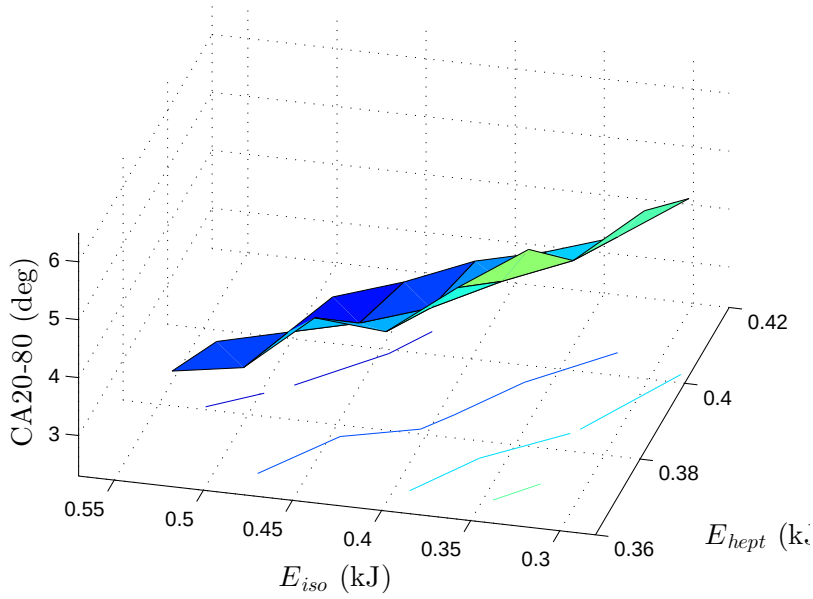

Figure 4.3: Steady-state combustion duration responses in HCCI with varying iso-octane and n-heptane.

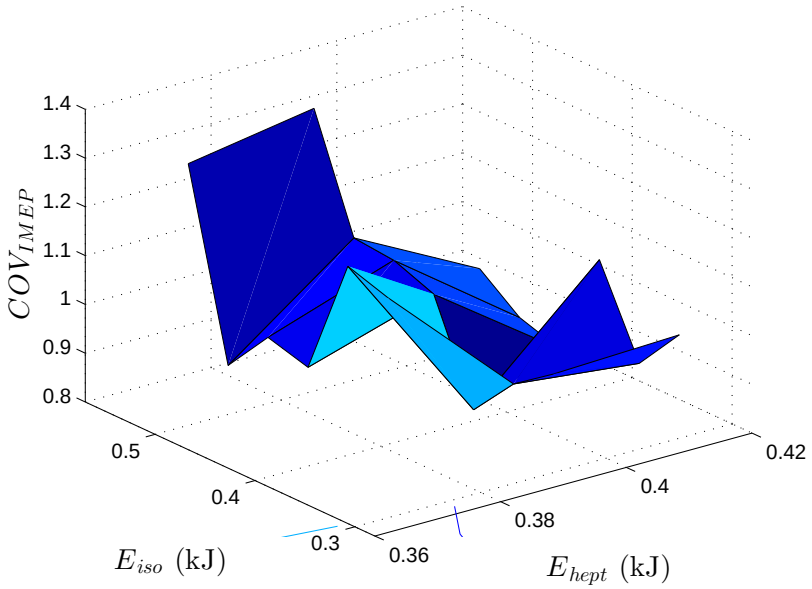

Figure 4.4: Steady-state combustion variation responses in HCCI with varying iso-octane and n-heptane.

system identification procedure is used to identify a model that accurately simulates the system Ljung [1999] using the input and output time series data of the system. The model can then be used to design a controller.

4.2.1 Pseudo-Random Binary Signal

The first step in system identification is to create an input that has persistent excitation. Persistent excitation to order n is defined in Soderstrom and Stoica [1989] as:

1. The following limit exists:

$$r_u(\tau) = \lim_{N\to\infty} \frac{1}{N} \sum_{t=1}^{N} u_{t+\tau} u_t^T \tag{4.2}$$

   Where u_t is the input at time t, τ is the lag and $r_u(\tau)$ is cross-correlation.

2. The matrix

$$R_u(n) = \begin{bmatrix} r_u(0) & r_u(1) & ... & r_u(n-1) \\ r_u(-1) & r_u(0) & ... & r_u(n-2) \\ \vdots & \vdots & \ddots & \vdots \\ r_u(1-n) & ... & ... & r_u(0) \end{bmatrix} \tag{4.3}$$

   is positive definite.

A necessary condition for consistent estimation (i.e. as $N \to \infty$, the estimated parameters of the system, $\hat{\theta}$, approaches the actual system parameters, θ) of a linear model of order n is the input should have persistent excitation to order $2n$ except for ARX model Huang et al. [2013]. A random binary signal has persistent excitation to any order Huang et al. [2013]. However it also excites all frequencies which may not be ideal as some unnecessary dynamics may be captured Huang et al. [2013].

Instead some frequencies can be eliminated by using a Pseudo-Random Binary Signal (PRBS) as an input. This is implemented using Matlabs "idinput" function Ljung [1999]. This signal randomly jumps between two levels. The length of the input is set to 1000 cycles as this is the maximum the software can store as described in Chapter 3. The PRBS levels are constrained by the operating domain limits described in Section 4.1. To cover the operating range and maintain the highest signal to noise ratio, the PRBS levels are set to the maximum operating range. This results in: $0.370 \leq E_{hept} \leq 0.409$ kJ and $0.332 \leq E_{iso} \leq 0.448$ kJ. The normalized frequency band of the input is $[0, 0.2]$ and the sample rate is every other engine revolution (at 800 RPM this is ≈ 6.7 Hz) This ensures sufficient number of level changes occur in the input but still enough low frequency excitation to capture any slow dynamics like RPM response and wall temperature changes. The results of the PRBS input, with operating conditions given in Table 3.7 and the mean removed from both the input and output signals, is given in Fig. 4.5. Here the Δ signifies that the mean was removed from the signal as

$$\Delta\text{CA50} = \text{CA50} - \text{CA50}_m \tag{4.4}$$

where CA50_m is mean CA50 for all 1000 cycles. Likewise is done for the other signals.

The data is then separated into the identification and validation data, with 700 cycles being used for identification of the system and 300 being used for validation of the model. The validation data is used to evaluate how well the model predicts the output. By keeping the identification data separate from the validation data helps ensure the model does not "over-fit" the data Huang et al. [2013].

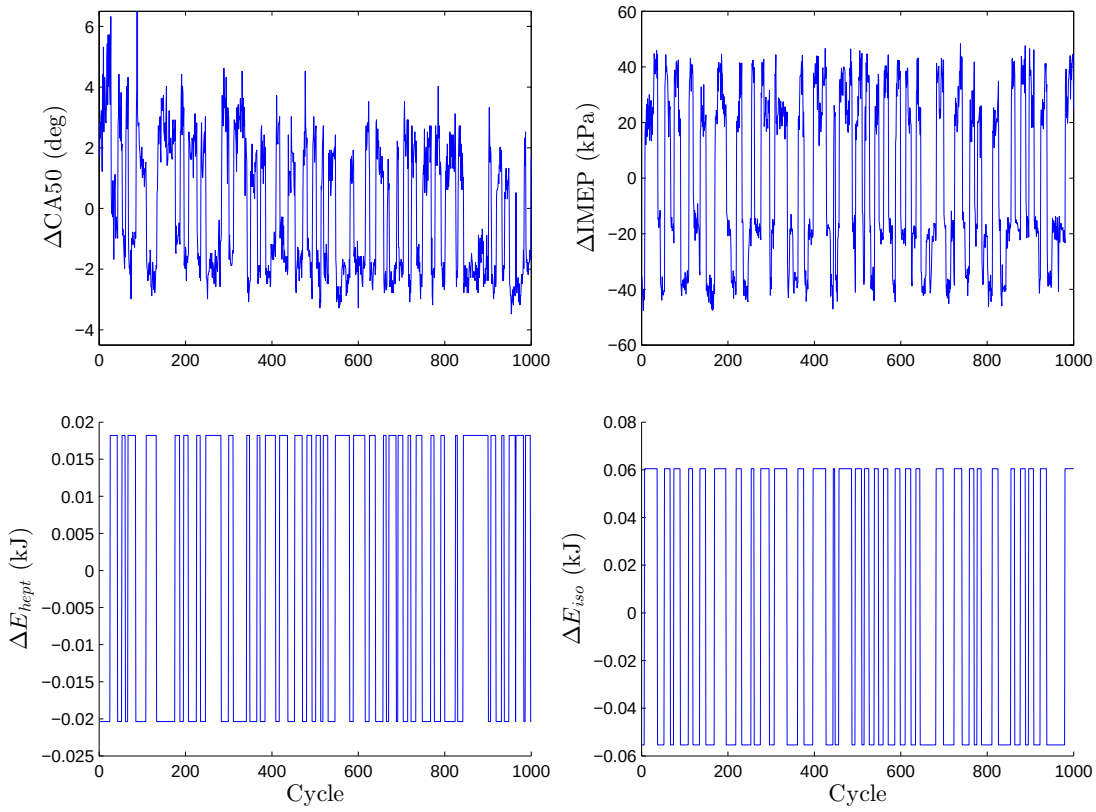

Figure 4.5: PRBS inputs and engine responses for operating conditions given in Table 3.7 with mean removed.

4.2.2 ARMAX Model

For system identification an Auto Regressive Moving Average with eXogenous input (ARMAX) model structure is used Ljung [1999]. This model structure is chosen as it is a simple model with dynamics and includes a noise model. This makes system identification easier and gives reasonable results as found in Audet [2008] which found no improvement for using the Box-Jenkins model over the ARMAX. The ARMAX model takes the form of:

$$\mathbf{a}(z)y(k) = \mathbf{b}(z)u(k) + \mathbf{c}(z)d(k) \tag{4.5}$$

where $y(k) \in \mathbb{R}^p$ and $u(k) \in \mathbb{R}^m$ are the p outputs and the m inputs of the system respectively, $d(k)$ is the noise, z^{-1} is the back-shift operator and k is the "time step" of the system, which is equivalent to a combustion event, or two crankshaft revolutions, for this system. The terms $\mathbf{a}(z)$, $\mathbf{b}(z)$ and $\mathbf{c}(z)$ are matrices of polynomial defined as:

$$\mathbf{a}(z) = \begin{bmatrix} a_{11}(z) & a_{12}(z) \\ a_{21}(z) & a_{22}(z) \end{bmatrix} \tag{4.6}$$

$$\mathbf{b}(z) = \begin{bmatrix} b_{11}(z) & b_{12}(z) \\ b_{21}(z) & b_{22}(z) \end{bmatrix} \tag{4.7}$$

$$\mathbf{c}(z) = \begin{bmatrix} c_1(z) & 0 \\ 0 & c_2(z) \end{bmatrix} \tag{4.8}$$

and the polynomials take the form of:

$$a(z) = 1 + a_1 z^{-1} + a_2 z^{-2} + a_3 z^{-3} + ... + a_{n_a} z^{-n_a} \tag{4.9}$$

$$b(z) = z^{-n_k}(b_0 + b_1 z^{-1} + b_2 z^{-2} + b_3 z^{-3} + ... + b_{n_b} z^{-n_b}) \tag{4.10}$$

$$c(z) = 1 + c_1 z^{-1} + c_2 z^{-2} + c_3 z^{-3} + ... + c_{n_c} z^{-n_c} \tag{4.11}$$

where a, b, c are the coefficients to be identified, n_a, n_b, n_c are the number of poles, zeros plus 1 and coefficients of $C(z)$, respectively. These are refered to as the order of the polynomials Ljung [1999]. The term n_k is the "delay" of the system and corresponds to how many time steps it takes before the system responds to the input. For the CFR engine setup n_k is taken as 1 as the injected fuel is first burned and then both IMEP and CA50 are calculated for the next cycle. With the model structure defined and n_k given, the orders of the polynomials can be obtained using a parametric system identification process Ljung [1999].

Three properties of the validation data simulation are chosen to evaluated how well the model simulates the system Huang et al. [2013]. They are the **residual correlation**, the **input-residual correlation** Ljung [1999] and the **% fit of the infinite step-ahead prediction**. The residuals are found from the error of the one step-ahead predictor of the model on the validation data. The one step-ahead predictor uses input and output data from before the current time step to predict the next value. In contrast, the infinite step-ahead predictor does not use the output data and only the input data to predict what the output values will be. By evaluating the cross-correlation of the residuals, a measure of how close the residuals are to white-noise is obtained. Since white noise is defined to be entirely uncorrelated, if the residuals are white noise this indicates that the model captures the deterministic part of the data Huang et al. [2013]. The cross-correlation of white noise, v_k, with itself should have a correlation of:

$$E(v_k v_{k-j}) = \begin{cases} \lambda^2 & \text{if } j = 0 \\ 0 & \text{if } j \neq 0 \end{cases} \tag{4.12}$$

with λ being the standard deviation of the noise at time step k, and $E(\cdot)$ indicating the expected value Huang et al. [2013]. The **input-residual correlation** tests correlation of the residuals to the input. If the correlation is zero for all lags then the residuals are uncorrelated to the input and that indicates no information for predicting the residuals is contained in the inputs and the model plant perfectly matches the plant for the given data set Huang et al. [2013].

The **% fit** is found using the following formula Mathworks [2015]:

$$\textbf{\% fit} = 100\left(1 - \frac{||y - \hat{y}||}{||y - \bar{y}||}\right) \tag{4.13}$$

where y is the recorded output data, $\hat{y}$ is the infinite step-ahead prediction, and $\bar{y}$ is the mean of the output data.

The orders, n_a, n_b, and n_c, are found from starting at 1 and increasing until none of the three criteria significantly changed. The noise order n_c is increased first, then the zeros, n_b, and finally the poles, n_a. With the parsimony principle, model complexity is considered as well Huang et al. [2013]. This is the reasoning for increasing the orders in this fashion as noise order has no effect on "plant complexity" and the poles have more effect on "system complexity" than the zeros do. To keep minimal complexity, if increasing the order only has a minimal affect on one of the evaluations, e.g. increase a **% fit** by ≈ 0.01, then the lower order is kept. The final model cross-correlations are given in Figs. 4.6 and 4.7. The dashed lines signify 99% confidence interval. Any

Table 4.1: ARMAX polynomial orders.

Order	Polynomial
0	a_{12}, a_{21}
2	a_{11}, a_{22}, b_{11}, b_{12}, b_{21}, b_{22}, c_1, c_2

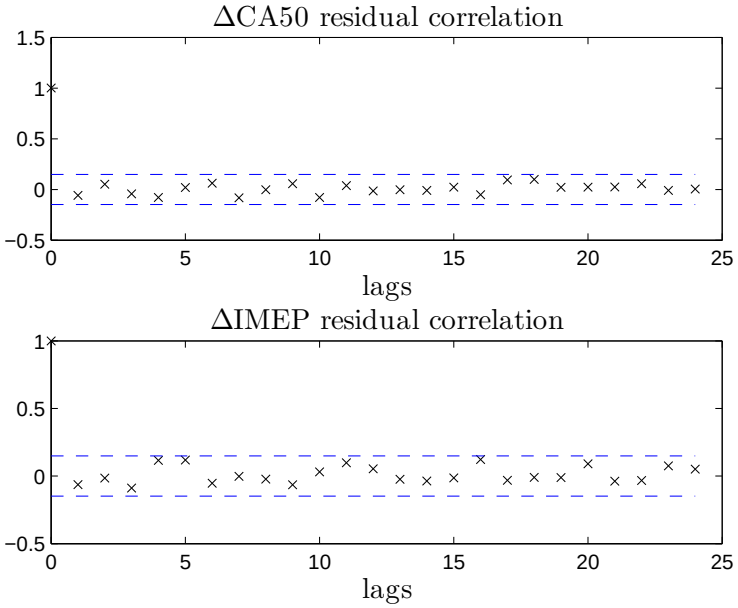

Figure 4.6: Cross-correlations of CA50 and IMEP ARMAX residuals from PRBS validation data with themselves.

point that lies within the confidence interval is deemed acceptable Huang et al. [2013]. The infinite step-ahead prediction is compared to the validation data in Fig. 4.8 with a **% fit** of 69.3 and 84.4 for CA50 and IMEP respectively. The model orders are given in Table 4.1 with coefficients given in Appendix C.

4.2.3 Markov Parameters

Another useful plant model are the Markov parameters, also known as the impulse response Ahn et al. [2007a]. From a system plant, P, with a state-state space model of the form:

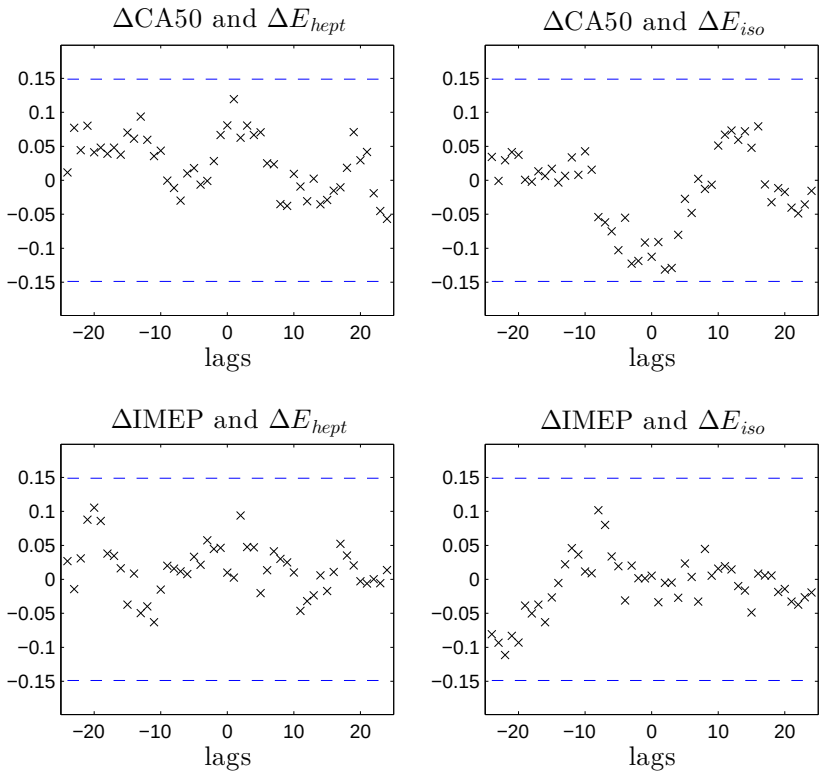

Figure 4.7: Cross-correlations of CA50 and IMEP ARMAX residuals from PRBS validation data with system inputs.

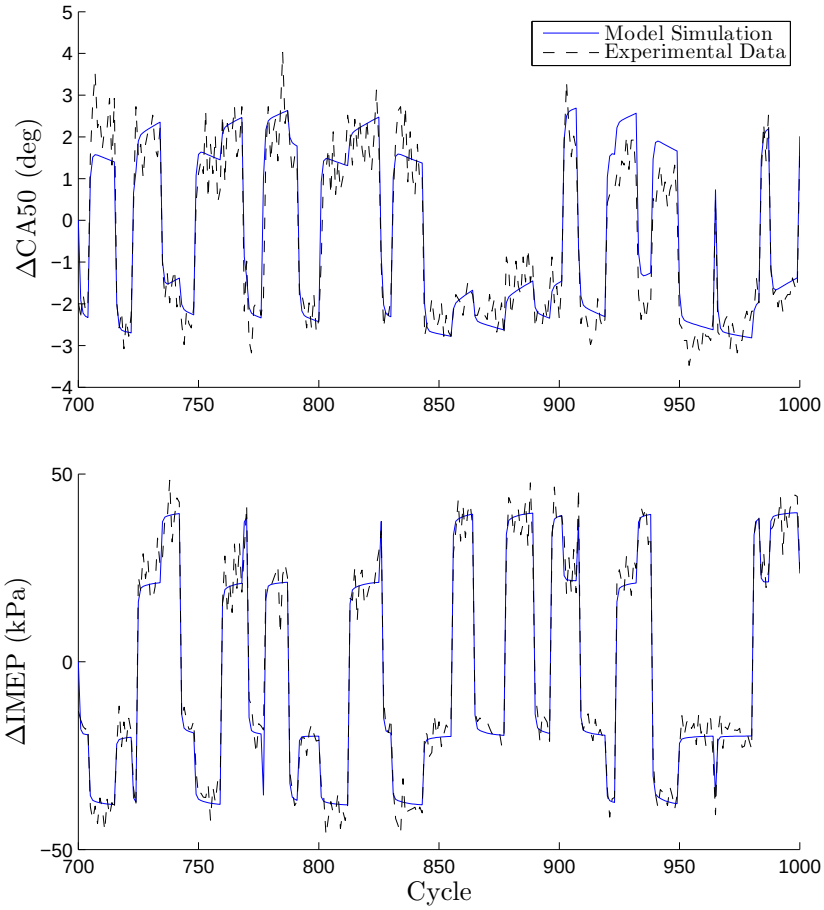

Figure 4.8: ARMAX model simulation compared to PRBS experimental validation data.

$$P \equiv \begin{cases} x(k+1) = A(k)x(k) + B(k)u(k) \\ \qquad y(k) = C(k)x(k) + D(k)u(k) \end{cases} \tag{4.14}$$

and assuming linear time invariant (LTI) system, the Markov parameters can be calculated as Ahn et al. [2007a]:

$$h(i) = \begin{cases} D & i = 0 \\ CA^{i-1}B & i > 0 \end{cases} \tag{4.15}$$

where $h(i) \in \mathbb{R}^{p \times m}$ is the i^{th} Markov parameter and $x \in \mathbb{R}^n$ being the system states, $u \in \mathbb{R}^m$ contains the inputs, and $y \in \mathbb{R}^p$ contains the outputs. For a plant transfer function:

$$y(k) = G_p(z)u(k) \tag{4.16}$$

with,

$$G_P(z) = \frac{b(z)}{a(z)} \tag{4.17}$$

the Markov parameters, or impulse response, are found from the coefficients of the long division of $a(z)$ into $b(z)$ Ljung [1999]. The Markov parameters can be used to determine the system response, $y(k)$ from any input, $u(k)$ as:

$$y(k) = (h * u)(k) \tag{4.18}$$

where $*$ is the convolution operator.

To find the Markov parameters, two linear regressions, one for each output, are performed on the PRBS data with the regression coefficients $\beta_j \in \mathbb{R}^{2n}$ being the Markov parameters, the inputs being the regressors, $\mathbf{X} \in \mathbb{R}^{N \times 2n}$ and the outputs being the regressands, $\mathbf{y}_j \in \mathbb{R}^N$ with j signifying which output, i.e. $j = 1$ corresponding to CA50 and $j = 2$ corresponding to IMEP. The regression is formulated as:

$$\mathbf{y}_j = \mathbf{X}\beta_j + \epsilon_j \tag{4.19}$$

with $\epsilon_j \in \mathbb{R}^N$ being the noise term and the other terms are:

$$\mathbf{y}_j = \begin{bmatrix} y_j(1) \\ y_j(2) \\ \vdots \\ y_j(N) \end{bmatrix}, \ \beta_j = \begin{bmatrix} H_{j1}(1) \\ H_{j2}(1) \\ \vdots \\ H_{j1}(n) \\ H_{j2}(n) \end{bmatrix} \tag{4.20}$$

$$\mathbf{X} = \begin{bmatrix} u_1(0) & u_2(0) & 0 & ... & 0 \\ u_1(1) & u_2(1) & u_1(0) & u_2(0) & 0 \\ \vdots & \ddots & & \ddots & \vdots \\ u_1(n) & u_2(n) & ... & u_1(0) & u_2(0) \\ \vdots & & \ddots & & \vdots \\ u_1(N-1) & u_2(N-1) & ... & u_1(N-n) & u_2(N-n) \end{bmatrix} \tag{4.21}$$

with n being the number of Markov terms to be determined and $N+1$ being the number of data points. The Markov parameters are $H(i)_{jk}$ for the i^{th} parameter that corresponds the k^{th} input to the j^{th} output. The subscripts for the inputs are: $k = 1$ is E_{hept} and $k = 2$ is E_{iso} . Since the system has a single step time delay, this means that the $i = 0$ Markov parameters are 0 and therefore do not need to be included in the regression. The least-squares solution to β_j is:

$$\hat{\beta}_j = (\mathbf{X}^T\mathbf{X})^{-1}\mathbf{X}^T\mathbf{y}_j \tag{4.22}$$

With a variance of:

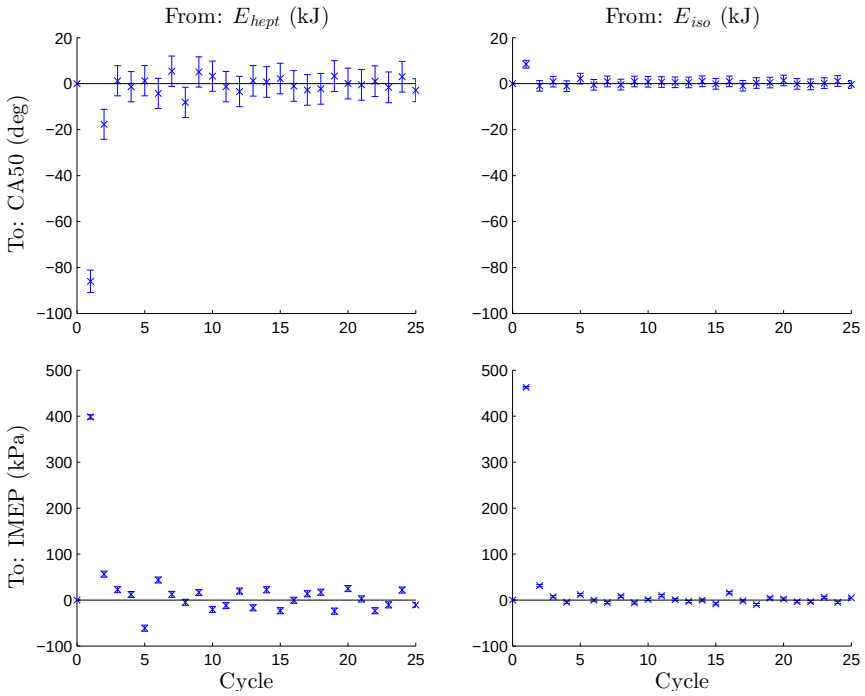

Figure 4.9: Markov parameters for operating conditions given in Table 3.7 with 95% confidence intervals found from linear regression of PRBS data.

$$Cov(\hat{\beta}_j) = (\mathbf{X}^T\mathbf{X})^{-1}\lambda_j^2 \tag{4.23}$$

with λ_j^2 is the noise variance of ϵ_j.

The results of the linear regression with a 95% confidence interval on each parameter in eqn. 4.20 for 25 of the parameters are given in Fig. 4.9.

4.3 Control Design

Defining the system P for a repetitive process by following eqn. 4.14 results in:

$$P \equiv \begin{cases} x_j(k+1) = A(k)x_j(k) + B(k)u_j(k) \\ \delta y_j(k) = C(k)x_j(k) + D(k)u_j(k) \end{cases} \tag{4.24}$$

$$y_j(k) = \delta y_j(k) + y_o(k) + d_j(k) \tag{4.25}$$

where $k \in [0, N-1]$ is the time step, N is the number of data points per "pass", and j is the iteration. This is a representation of the plant for a repetitive process. The system disturbance is $d_j \in \mathbb{R}^p$ for iteration j. Then P can be written as a lower triangular block matrix containing the Markov parameters as:

$$P = \begin{bmatrix} \mathbf{H}_{0,0} & & 0 \\ \vdots & \ddots & \\ \mathbf{H}_{N-1,0} & \cdots & \mathbf{H}_{N-1,N-1} \end{bmatrix} \tag{4.26}$$

With $\mathbf{H}_{k,j}$ being the j^{th} Markov parameter for the k^{th} time step. Since $D = 0 \in \mathbb{R}^{p \times m}$, assuming Linear Time Invariance (LTI) and referring to eqn. 4.15, P becomes:

$$P = \begin{bmatrix} 0 & & \cdots & & 0 \\ \mathbf{H}(1) & 0 & & & \vdots \\ \mathbf{H}(2) & \mathbf{H}(1) & 0 & & \\ \vdots & & & \ddots & \\ \mathbf{H}(N-1) & & \cdots & \mathbf{H}(1) & 0 \end{bmatrix} \tag{4.27}$$

Where $\mathbf{H}(i) \in \mathbb{R}^{p \times m}$. For the single cylinder engine, with $p = m = 2$, it is:

$$\mathbf{H}(i) = \begin{bmatrix} h_{11}(i) & h_{12}(i) \\ h_{21}(i) & h_{22}(i) \end{bmatrix} \tag{4.28}$$

where $h(i)_{jk}$ is the i^{th} Markov parameter corresponding the k^{th} input to the j^{th} output. This makes $P \in \mathbb{R}^{pN \times mN}$. The system can be written in a lifted form as Barton and Alleyne [2011]:

$$\mathbf{y}_j = P\mathbf{u}_j + \mathbf{d}_j \tag{4.29}$$

with

$$\mathbf{u}_j = \begin{bmatrix} u_j(0) \\ u_j(1) \\ \vdots \\ u_j(N-1) \end{bmatrix}, \; u_j(k) = \begin{bmatrix} u_j^{(1)}(k) \\ \vdots \\ u_j^{(m)}(k) \end{bmatrix} \tag{4.30}$$

$$\mathbf{y}_j = \begin{bmatrix} y_j(0) \\ y_j(1) \\ \vdots \\ y_j(N-1) \end{bmatrix}, \; y_j(k) = \begin{bmatrix} y_j^{(1)}(k) \\ \vdots \\ y_j^{(p)}(k) \end{bmatrix} \tag{4.31}$$

Here $\mathbf{u}_j$ is the input over all time samples at iteration j, and $u_j(k)$ is the m inputs (here 2) at time step k. Similarly, $\mathbf{y}_j$ is the output over all time samples at iteration j, and $y_j(k)$ is the p outputs (here 2) at time step k. This is also known as a "super-vector" rearrangement as $\mathbf{u}_j \in \mathbb{R}^{mN}$ and $\mathbf{y}_j \in \mathbb{R}^{pN}$ becomes a vector containing each time step's input and output for the j^{th} iteration. For the CFR engine $u_j(k)$ and

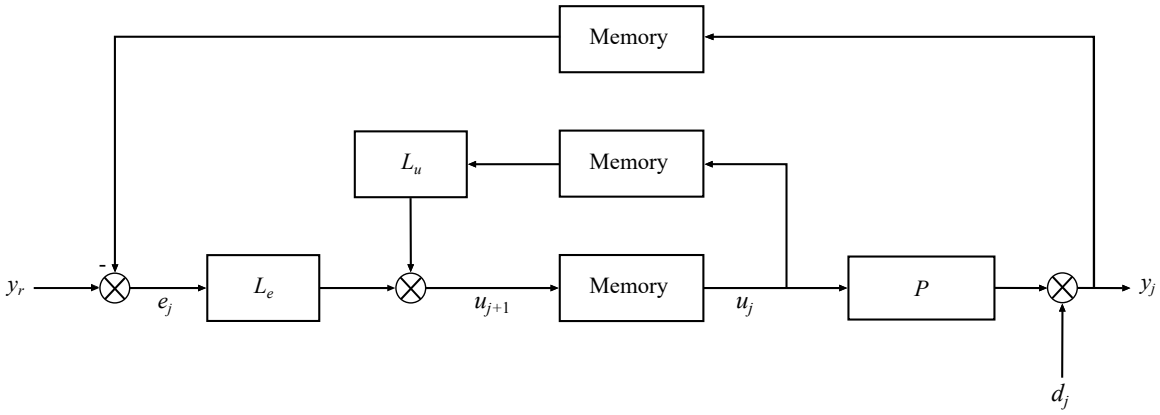

Figure 4.10: ILC block diagram schematic with memory blocks signifying when an iteration of data is saved.

$y_j(k)$ are:

$$u_j(k) = \begin{bmatrix} E_{hept,\,j}(k) \\ E_{iso,\,j}(k) \end{bmatrix}, \; y_j(k) = \begin{bmatrix} \mathrm{CA50}_j(k) \\ \mathrm{IMEP}_j(k) \end{bmatrix} \tag{4.32}$$

The iteration error, $\mathbf{e}_j$, given a reference trajectory $\mathbf{y}_r$, is defined as:

$$\mathbf{e}_j = \mathbf{y}_r - \mathbf{y}_j \tag{4.33}$$

A generalized ILC can then be implemented as, Barton and Alleyne [2011]:

$$\mathbf{u}_{j+1} = L_u \mathbf{u}_j + L_e \mathbf{e}_j \tag{4.34}$$

L_e and L_u are termed the learning and forgetting filters, respectively. A block diagram showing this control strategy is given in Fig. 4.10. The memory blocks are used to save the entire iteration's data of its respective input. The purpose of the ILC control design is to reduce each time step's error using the previous iteration's error and input. Using eqs. 4.29, 4.33 and 4.34, the next iterations input can be written

as:

$$\mathbf{u}_{j+1} = (L_u - L_e P)\mathbf{u}_j + L_e(\mathbf{y}_r - \mathbf{d}_j)) \tag{4.35}$$

The system will be asymptotically stable if Bristow et al. [2006]:

$$\rho(L_u - L_e P) < 1 \tag{4.36}$$

with $\rho(\cdot)$ being the spectral radius defined in Section 3.9 and $\mathbf{y}_r$ is bounded, i.e. $||\mathbf{y}_r|| < \infty$. Choosing $L_u = I$ and assuming no noise or disturbance in the system, i.e. $d_j(k) = 0 \; \forall j, k$, eqn. 4.34 can be combined with eqns. 4.29 and 4.33 as:

$$\mathbf{u}_{j+1} = \mathbf{u}_j + L_e \mathbf{e}_j \tag{4.37}$$

$$P\mathbf{u}_{j+1} = P\mathbf{u}_j + PL_e \mathbf{e}_j \tag{4.38}$$

$$\mathbf{y}_{j+1} = \mathbf{y}_j + PL_e \mathbf{e}_j \tag{4.39}$$

$$\mathbf{y}_r - \mathbf{y}_{j+1} = \mathbf{y}_r - \mathbf{y}_j - PL_e \mathbf{e}_j \tag{4.40}$$

$$\mathbf{e}_{j+1} = \mathbf{e}_j - PL_e \mathbf{e}_j \tag{4.41}$$

$$\mathbf{e}_{j+1} = (I - PL_e)\mathbf{e}_j \tag{4.42}$$

From eqn. 4.42, convergence to zero error is guaranteed if $\rho(I - PL_e) < 1$ Meng et al. [2011]. However ILC are known to have large transients Bristow et al. [2006], and it is desirable to also guarantee monotonic convergence. By taking the norm of eqn. 4.42 as defined in Section 3.9, the following is obtained Meng et al. [2011]:

$$||\mathbf{e}_{j+1}|| = ||(I - PL_e)\mathbf{e}_j|| \leq ||(I - PL_e)||\,||\mathbf{e}_j|| \tag{4.43}$$

If $||(I - PL_e)|| < 1$ then the system will have monotonic convergence in the sense of the chosen norm, here being the 2-norm. Note: the norm will be larger than or equal to the spectral radius for any matrix, i.e. $||A|| \geq \rho(A)$, making the monotonic convergence a more stringent criteria.

4.3.1 Norm-Optimal

There are many ways to design L_e and L_u Bristow et al. [2006]. One example is a norm optimal approach proposed by Barton and Alleyne [2011]. This involves minimizing a cost parameter $\mathcal{J}$, defined as:

$$\mathcal{J} = \mathbf{e}_{j+1}^T Q \mathbf{e}_{j+1} + \mathbf{u}_{j+1}^T S \mathbf{u}_{j+1} + (\mathbf{u}_{j+1} - \mathbf{u}_j)^T R (\mathbf{u}_{j+1} - \mathbf{u}_j) \tag{4.44}$$

where $Q \in \mathbb{R}^{pN \times pN}$, $S \in \mathbb{R}^{mN \times mN}$, and $R \in \mathbb{R}^{mN \times mN}$ are weight matrices for the error, input and change in input between iterations respectively. The learning and forgetting matrices can then be determined as:

$$\begin{aligned} L_u &= (P^T Q P + S + R)^{-1}(P^T Q P + R) \\ L_e &= (P^T Q P + S + R)^{-1} P^T Q \end{aligned} \tag{4.45}$$

For the norm-optimal, combining eqs. 4.42 and 4.45 gives Barton and Alleyne [2011]:

$$L_u - L_e P = (P^T Q P + S + R)^{-1} R \tag{4.46}$$

Convergence is then guaranteed for any symmetric positive definite Q, R and S with $P^T Q P + S + R$ being positive definite Barton and Alleyne [2011]. For LTI, it is common to set $Q = qI$, $R = rI$, and $S = sI$ to make the design easier and have minimal effects on control performance Barton and Alleyne [2011]. Since the weighting matrices weight the system variables in comparison to each other, q is set to 1 without a loss of generality. For the system to converge to zero steady-state error $||S||_2 = 0$ Barton and Alleyne [2011], therefore the s is set to 0. Thus with $Q = I$, $R = rI$ and $S = 0$, eqn. 4.45 becomes:

$$\begin{aligned} L_u &= (P^T P + rI)^{-1}(P^T P + rI) = I \\ L_e &= (P^T P + rI)^{-1} P^T \end{aligned} \tag{4.47}$$

and eqn. 4.46 becomes:

$$L_u - L_e P = r(P^T P + rI)^{-1} \tag{4.48}$$

To find the optimal value of r, the norm-optimal control is simulated using the ARMAX model found in Section 4.2.2 and using the ARMAX impulse response to create the P matrix. Increasing r has two major effects, it slows down convergence but also limits the effects that stochastic disturbances have on the subsequent iterations Barton and Alleyne [2011]. By testing the norm-optimal control, it was found that

noticeable convergence changes are only observed with changes in r magnitude. The r value was increased in magnitude until it noticeably affected the system convergence. To show this results for three of the simulated r values, $r = 1$, $r = 1000$, and $r = 100000$, are given.

The error norm iteration plot, i.e. $||\mathbf{e}_j||$ vs. j, for each r value using the ARMAX model simulation is shown in Fig. 4.11. For each r value, the convergence of the engine IMEP error norm is consistent with convergence achieved by the 4^{th} iteration. The CA50 error norm Figs. 4.11a and 4.11b are similar but for $r = 100000$ convergence is not reached within the 20 iterations as shown in Fig. 4.11c. This indicates that an r value this large slowed convergence. The difference in convergence time between IMEP and CA50 error norm for Fig. 4.11c is thought to be a result of the relative magnitudes of the two outputs and having equal weightings in the Q matrix.

The three r values are then experimentally implemented on the CFR engine and the norm-error convergences are shown in Fig. 4.11. The similarities between the experimental and simulated error norms, shown in Fig. 4.11, are noticeable giving indication that the ARMAX model does well in describing the engine's response to the ILC controller. To evaluate the ILC performance on the engine as a function of r, the mean error norm and standard deviation of the last 10 cycles' error norm are given in Tables 4.2 and 4.3 for CA50 and IMEP, respectively. The converged iteration, j_{conv}, is also given. This is defined as the first iteration that is within the standard deviation of the error mean. Due to the stochastic nature of error norm at convergence, j_{conv} will have a statistical property and is not reliable within 2 iterations. To get an accurate j_{conv} value multiple convergences must be done to find the distribution and mean. This would be time consuming and is not done in this study; instead when two control schemes are being compared, the j_{conv} value is confirmed with visual inspection of the error norm plots.

From the engine response, the $r = 1000$ case performed as expected with little

effect on the convergence time compared to $r = 1$ but with a 21% decrease in standard deviation for CA50. For the case of $r = 100000$ IMEP converged well with having a lower mean error norm and standard deviation compared to $r = 1$ and $r = 1000$ cases, but has poor convergence response in CA50 and long convergence time for IMEP so $r = 1000$ is chosen as best compromise. The final iteration, $j = 15$, control signals for $r = 1000$ are given in Fig. 4.12. The ability for an ILC controller to anticipate the reference steps despite a time delay in the system is due to the repetitive nature of the input learning and is shown in Fig. 4.12. By using the error of the previous iteration, the controller learns how to improve the input for better tracking control. This is shown in Figs. 4.13 and 4.14. These figures show the evolution of the IMEP error through each iteration. The $r = 1000$ case converges quickly so little can be discerned between the 2^{nd} and 3^{rd} iteration traces but the 1^{st} to 2^{nd} has a major decrease in error. For the $r = 100000$ case the evolution of error through the iterations is more noticeable.

Table 4.2: Experimental norm-optimal ILC performance results for CA50 error norm convergence.

ILC	mean($\|\|e_{\text{CA50}}\|\|_2$)	std($\|\|e_{\text{CA50}}\|\|_2$)	$j_{conv,\,\text{CA50}}$
$r = 1$	5.51	0.624	2
$r = 1000$	5.36	0.494	3
$r = 100000$	20.4	4.09	1

Table 4.3: Experimental norm-optimal ILC performance results for IMEP error norm convergence.

ILC	mean($\|\|e_{\text{IMEP}}\|\|_2$)	std($\|\|e_{\text{IMEP}}\|\|_2$)	$j_{conv,\,\text{IMEP}}$
$r = 1$	40.0	6.08	2
$r = 1000$	37.7	6.64	2
$r = 100000$	31.3	4.26	4

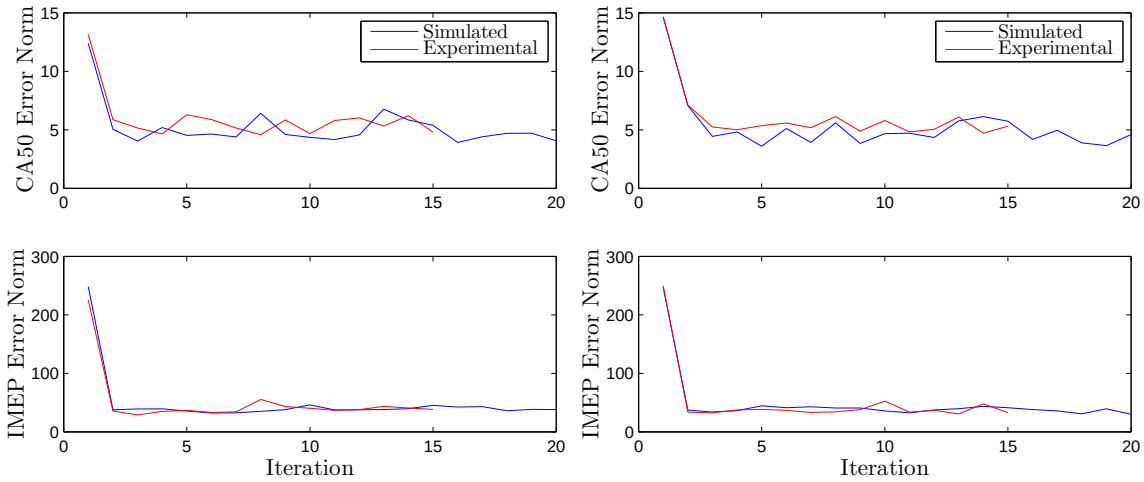

(a) $r = 1$.

(b) $r = 1000$.

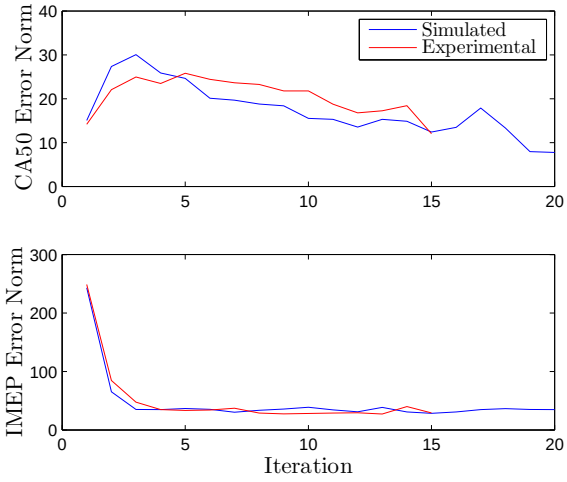

(c) $r = 100000$.

Figure 4.11: Simulation and experimental error norm using a norm-optimal ILC for varying r values using operating conditions given in Table 3.7.

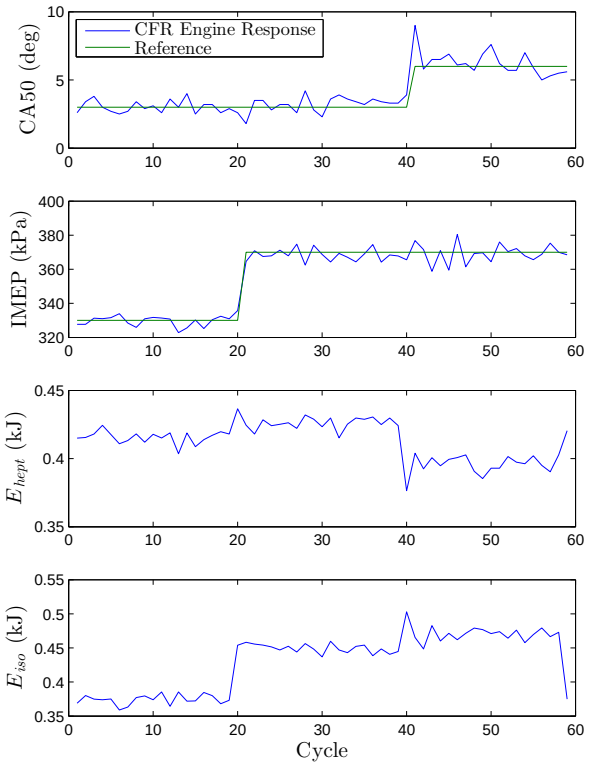

Figure 4.12: Experimental final iteration control responses with $r = 1000$.

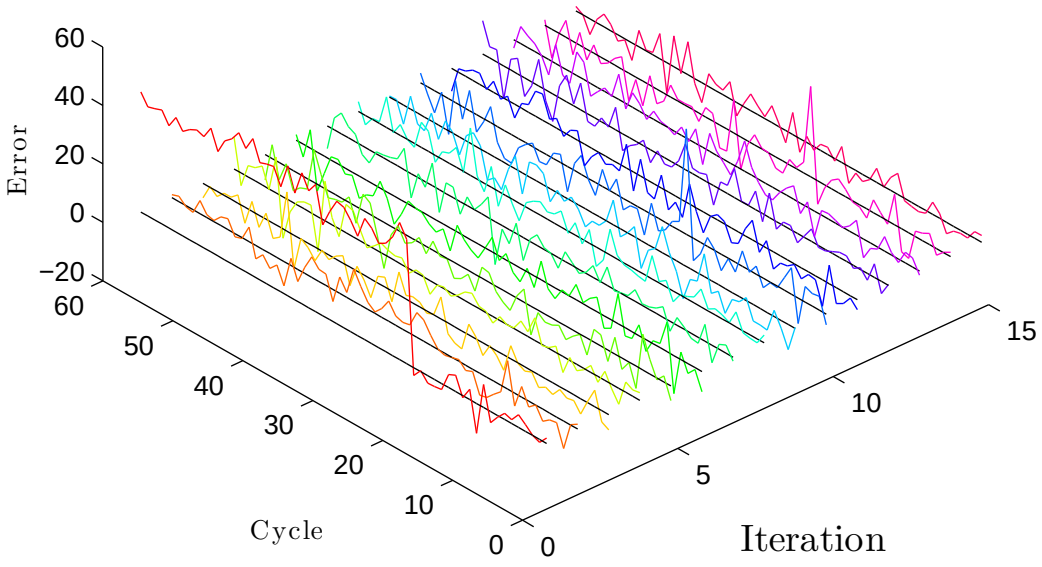

Figure 4.13: Experimental IMEP errors with $r = 1000$ for each iteration.

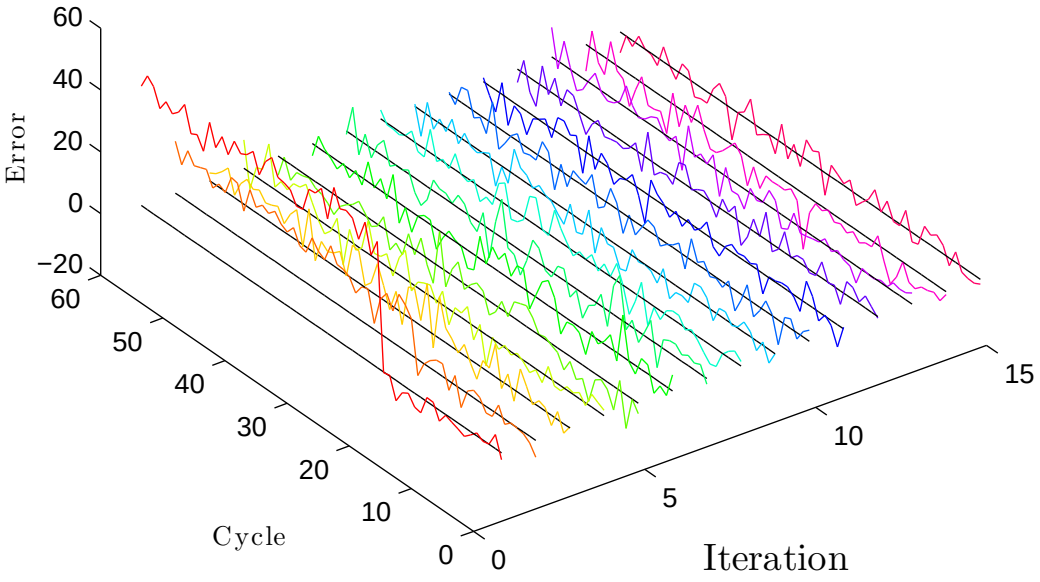

Figure 4.14: Experimental IMEP errors with $r = 100000$ for each iteration.

4.3.2 Model-less

A common ILC update law is Ahn et al. [2007a]:

$$u_{j+1}(k) = u_j(k) + \gamma e_j(k+1) \tag{4.49}$$

for a Single-Input Single-Output (SISO) system with a time delay of 1 step and with γ being the being Arimoto-like learning gain. In super-vector form:

$$\mathbf{u}_{j+1} = L_u \mathbf{u}_j + L_e \mathbf{e}_j \tag{4.50}$$

Eqn. 4.49 has learning and forgetting filters of:

$$L_e = \begin{bmatrix} 0 & \gamma & 0 & \dots & & 0 \\ 0 & 0 & \gamma & 0 & \dots & 0 \\ \vdots & & & \ddots & & \vdots \\ 0 & \dots & & & & \gamma \\ 0 & \dots & & & & 0 \end{bmatrix} \tag{4.51}$$

$$L_u = I \tag{4.52}$$

Ensuring stability requires only that γ must be chosen so that $|1 - \gamma h(1)| < 1$ Ahn et al. [2007a]. However, with a Multi-Input Multi-Output (MIMO) system, γ is a matrix, $\gamma \in \mathbb{R}^{m \times p}$, which makes selecting γ more difficult as each output has different magnitudes and are affected by each input in different proportions. To compensate for this, a method to design γ such that even in MIMO operation only a single value needs to be adjusted for control robustness is developed. This method will be called

the "model-less" control as it does not require dynamic modeling for its design. This method assumes the number of inputs equals the number of outputs, $m = p$, and the steady-state Jacobian, $J \in \mathbb{R}^{p \times m}$, of the system as found in Section 4.1 is needed. The Jacobian is Kaplan [1984]:

$$J(u_1,\, u_2 ... u_m) = \begin{bmatrix} \frac{\partial f_1}{\partial u_1}\big|_{(u_1,\, u_2 ... u_m)} & \cdots & \frac{\partial f_1}{\partial u_m}\big|_{(u_1,\, u_2 ... u_m)} \\ \vdots & \ddots & \vdots \\ \frac{\partial f_p}{\partial u_1}\big|_{(u_1,\, u_2 ... u_m)} & \cdots & \frac{\partial f_p}{\partial u_m}\big|_{(u_1,\, u_2 ... u_m)} \end{bmatrix} \tag{4.53}$$

where $y_{ss}^{(i)} = f_i(u_1,\, u_2 ... u_m)$ and all u_j are in steady-state. If the system is linear than the Jacobian is constant at all points. Thus, the Jacobian from eqn. 4.1 is:

$$J = \begin{bmatrix} -110 & 0.0445 \\ 464 & 492 \end{bmatrix} \tag{4.54}$$

Note: The Jacobian used here is a steady-state and not a dynamic Jacobian often used for linearizing state-space models. The steady-state Jacobian is the sensitivity between inputs and outputs of the system. The Jacobian is useful in that it provides a weighting between the inputs and the outputs. By taking the inverse of the Jacobian, the amount of each input needed for a desired output can be calculated. For the MIMO ILC update law, this looks like:

$$u_{j+1}(k) = u_j(k) + K \cdot J^{-1} e_j(k+1) \tag{4.55}$$

with K being a parameter that can be increased for faster response control like a

feedback control gain Franklin et al. [2015]. In super-vector form, L_e becomes a block matrix:

$$L_e = \begin{bmatrix} 0 & K \cdot J^{-1} & 0 & ... & & 0 \\ 0 & 0 & K \cdot J^{-1} & 0 & ... & 0 \\ \vdots & & & \ddots & & \vdots \\ 0 & ... & & & & K \cdot J^{-1} \\ 0 & ... & & & & 0 \end{bmatrix} \tag{4.56}$$

4.3.3 Stability

To find an optimal K value a stability analysis is performed. Here optimal is defined as the value of K that gives the quickest convergence time, therefore smallest $\rho(I - LP)$. This stability analysis uses interval matrices Ahn et al. [2007b]. Interval matrices are matrices whose elements are between two values given as Ahn et al. [2007b]:

$$A^I = [a_{ij}^I],\ a_{ij}^I \in [\underline{a_{ij}}, \overline{a_{ij}}],\ i, j = 1, ..., n \tag{4.57}$$

where $\overline{a_{ij}}$ indicates the maximum extreme value and $\underline{a_{ij}}$ indicates the minimum extreme value of the i^{th} row and j^{th} column element of the interval matrix $A^I \in R^{n \times n}$. The vertex matrices, A^V, of an interval matrix is defined as:

$$A^V = [a_{ij}^V],\ a_{ij}^V \in \{\underline{a_{ij}}, \overline{a_{ij}}\},\ i, j = 1, ..., n \tag{4.58}$$

Therefore, there are 2^{n^2} vertex matrices for single interval matrix. The interval matrix's spectral radius is bounded by the maximum spectral radius of the vertex

matrices Ahn et al. [2007b]. This allows the stability of the system to be guaranteed even if the exact Markov parameters are not known.

Using eqs. 4.56 and 4.27 the following block matrix is:

$$PL_e = \begin{bmatrix} 0 & 0 & ... & & 0 \\ 0 & K\mathbf{H}(1)J^{-1} & 0 & ... & 0 \\ \vdots & K\mathbf{H}(2)J^{-1} & K\mathbf{H}(1)J^{-1} & \ddots & \vdots \\ & K\mathbf{H}(3)J^{-1} & K\mathbf{H}(2)J^{-1} & K\mathbf{H}(1)J^{-1} & \\ & \vdots & & \ddots & \\ 0 & K\mathbf{H}(N-1)J^{-1} & ... & & K\mathbf{H}(1)J^{-1} \end{bmatrix} \tag{4.59}$$

which can then be used in eqn. 4.42. Note that a block triangular matrix's determinant is the multiplication of the determinants of the matrices down the diagonal Powell [2011]. Using this, the eigenvalues, without multiplicity, of $I - PL_e$ are 1 and eig$(I^{m\times m} - K\mathbf{H}(1)J^{-1})$. The eigenvalue of 1 is a result of the column of zeros in PL_e of eqn. 4.59 which is the from the time delay in the system. This means that the very first cycle's error cannot be manipulated, and is only a result of the systems initial condition. Ignoring the first cycles error allows the stability condition for $\rho(I - PL_e) < 1$ to be reduced to:

$$\rho(I^{m\times m} - K\mathbf{H}(1)J^{-1}) < 1 \tag{4.60}$$

An estimate for K can be found from the following logic of applying a steady-state, denoted with a subscript of ss, input into the system:

$$\Delta \mathbf{y}(k) = (\mathbf{H} * \Delta \mathbf{u})(k) \tag{4.61}$$

$$\Delta \mathbf{y}_{ss} = (\mathbf{H} * \Delta \mathbf{u}_{ss}) \tag{4.62}$$

$$\Delta \mathbf{y}_{ss} = \left[\sum_{i=1}^{\infty} \mathbf{H}(i) \right] \Delta \mathbf{u}_{ss} \tag{4.63}$$

where

$$\Delta \mathbf{u} = \mathbf{u} - \mathbf{u}_0 \tag{4.64}$$

$$\Delta \mathbf{y} = \mathbf{y} - \mathbf{y}_0 \tag{4.65}$$

with $\mathbf{u}_0$ and $\mathbf{y}_0$ chosen such that if $\Delta \mathbf{u}_{ss} = 0$ then $\Delta \mathbf{y}_{ss} = 0$ and $*$ denoting the convolution operation. Comparing eqn. 4.63 to

$$\Delta \mathbf{y}_{ss} = J \Delta \mathbf{u}_{ss} \tag{4.66}$$

gives

$$J = \sum_{i=1}^{\infty} \mathbf{H}(i) \tag{4.67}$$

and substituting the matrix argument of the spectral radius, ρ, in eqn. 4.60

$$I - K\mathbf{H}(1)J^{-1} = I - K\mathbf{H}(1)\left(\sum_{i=1}^{\infty}\mathbf{H}(i)\right)^{-1} \tag{4.68}$$

$$= I - K\left(\sum_{i=1}^{\infty}\mathbf{H}(i)\,\mathbf{H}^{-1}(1)\right)^{-1} \tag{4.69}$$

$$= I - K\left(I + \sum_{i=2}^{\infty}\mathbf{H}(i)\,\mathbf{H}^{-1}(1)\right)^{-1} \tag{4.70}$$

this is done assuming that $\mathbf{H}^{-1}(1)$ is non-singular. If $\underline{\sigma}(\mathbf{H}(1)) >> \overline{\sigma}(\sum_{i=2}^{\infty}\mathbf{H}(i))$ then

$$I + \sum_{i=2}^{\infty}\mathbf{H}(i)\,\mathbf{H}^{-1}(1) \approx I \tag{4.71}$$

with proof given in Appendix D. The interpretation of this assumption is the majority of the response is in the first cycle after the input. For the CFR engine this is found to be the case experimentally as shown in Fig. 4.9, the first Markov parameter dominates the subsequent ones. Substituting eqn. 4.71 into eqn. 4.70 gives:

$$I - K\left(I + \sum_{i=2}^{\infty}\mathbf{H}(i)\,\mathbf{H}^{-1}(1)\right)^{-1} \approx I - K(I)^{-1} \tag{4.72}$$

$$= I - KI \tag{4.73}$$

for a spectral radius of 0, $K = 1$. This will give a single iteration convergence to 0 error. This signifies that systems with large initial responses are to have an ideal K value near 1. By similar logic, if $\overline{\sigma}(\mathbf{H}(1)) << \underline{\sigma}(\sum_{i=2}^{\infty}\mathbf{H}(i))$ then

$$I + \sum_{i=2}^{\infty} \mathbf{H}(i)\, \mathbf{H}^{-1}(1) \approx \sum_{i=2}^{\infty} \mathbf{H}(i)\, \mathbf{H}^{-1}(1) \tag{4.74}$$

combining this with eqn. 4.70 gives

$$I - K\left(I + \sum_{i=2}^{\infty} \mathbf{H}(i)\, \mathbf{H}^{-1}(1)\right)^{-1} \approx I - K\left(\sum_{i=2}^{\infty} \mathbf{H}(i)\, \mathbf{H}^{-1}(1)\right)^{-1} \tag{4.75}$$

$$= I - K\mathbf{H}(1)\left(\sum_{i=2}^{\infty} \mathbf{H}(i)\right)^{-1} \tag{4.76}$$

as stated before $\rho(A) \leq \overline{\sigma}(A)$. Therefore minimizing the 2-norm of a matrix also minimizes the upper bound on the spectral radius. By taking the norm of eqn. 4.76 and applying the backwards triangle inequality Cassell [1854] with the assumption $K > 0$ gives

$$||I - K\mathbf{H}(1)\left(\sum_{i=2}^{\infty} \mathbf{H}(i)\right)^{-1}|| \geq \left|||I|| - ||K\mathbf{H}(1)\left(\sum_{i=2}^{\infty} \mathbf{H}(i)\right)^{-1}||\right| \tag{4.77}$$

$$= \left|1 - K||\mathbf{H}(1)\left(\sum_{i=2}^{\infty} \mathbf{H}(i)\right)^{-1}||\right| \tag{4.78}$$

which can be combined with

$$||\mathbf{H}(1)\left(\sum_{i=2}^{\infty} \mathbf{H}(i)\right)^{-1}|| << 1 \tag{4.79}$$

from eqn. 4.74. This means that for the lowest bound for the norm of eqn. 4.76 to be 0, $K >> 1$. This does not imply that the optimal K value is much larger

than 1, only that larger values minimize the lower bound of the matrix norm. One interpretation of this is that as majority of the response moves later in time, the optimal K values are likely to be larger. For the CFR engine response given in Section 4.2.3, the optimal value of K is expected to be slightly larger than 1. The first Markov parameter is:

$$\mathbf{H}(1) = \begin{bmatrix} \text{-86.0} & 8.47 \\ 398 & 463 \end{bmatrix} \tag{4.80}$$

from Fig. 4.9. This matrix has an inverse of:

$$\mathbf{H}(1)^{-1} = \begin{bmatrix} \text{-0.0107} & 0.0002 \\ 0.0092 & 0.002 \end{bmatrix} \tag{4.81}$$

showing that the assumption for $\mathbf{H}(1)$ being invertible is valid for this system.

In eqn. 4.60, $\mathbf{H}(1)$ is an interval matrix found in Section 4.2.3 where the intervals are the 95% confidence bounds given in Fig. 4.9 for the first cycle. Using the knowledge that the spectral radius is bounded by the vertices, the maximum spectral radius of the 16 vertex matrices is plotted with the nominal spectral radius as a function of K in Fig. 4.15. The minimum value of the maximal spectral radius is preferred as convergence will occur faster Barton and Alleyne [2011]. From Fig. 4.15 the minimum value occurs at $K = 1.12$ - slightly above one as expected. The system goes unstable for $K < 0$ or $K > 2$. Another property observed is the convergence of the expected and maximum spectral radius as K approaches 0. This shows that the control becomes more robust as K approaches 0. A plot of all 16 vertex matrices spectral radii as a function of K is given in Appendix D.

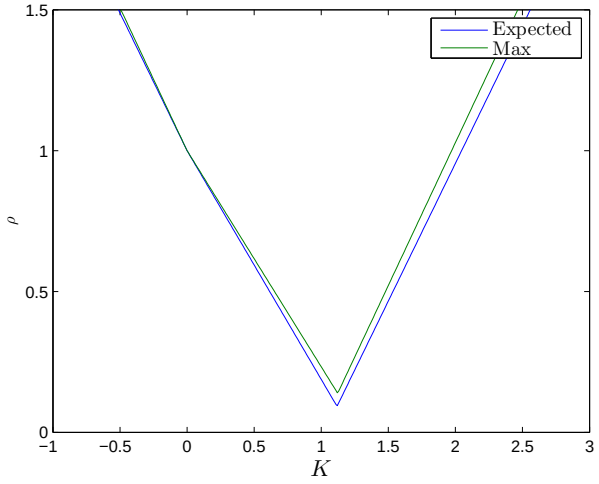

Figure 4.15: Maximum and expected spectral radius for varying K found from interval and nominal matrix of system plant shown in Fig 4.9.

4.3.4 Noise Transference

Similar to how eqn. 4.42 is formulated from eqns. 4.29, 4.33 and 4.34, but assuming d_j is stochastic gives:

$$\mathbf{e}_{j+1} = (I - PL)\mathbf{e}_j + (\mathbf{d}_j - \mathbf{d}_{j+1}) \tag{4.82}$$

which can then be used to solve for $\mathbf{e}_j$ as a function of the iteration, j, first iteration error, $\mathbf{e}_0$, and iteration stochastic disturbance, $\mathbf{d}_j$:

$$\mathbf{e}_j = (I - PL)^j \mathbf{e}_0 + (I - PL)^{j-1} \mathbf{d}_0 + \sum_{i=1}^{j-1} (I - PL)^{j-i-1} PL\, \mathbf{d}_i - \mathbf{d}_j \tag{4.83}$$

Taking the norm of eqn. 4.83 gives

$$||\mathbf{e}_j|| \leq ||(I-PL)||^j||\mathbf{e}_0|| + ||(I-PL)||^{j-1}||\mathbf{d}_0|| + ||PL||\sum_{i=1}^{j-1}||(I-PL)||^{j-i-1}||\mathbf{d}_i|| + ||\mathbf{d}_j|| \tag{4.84}$$

As discussed before if $||(I-PL)|| < 1$ then the system will converge as the $\mathbf{e}_0$ and $\mathbf{d}_0$ terms will approach 0 as $j \to \infty$ and the summation term will converge assuming the $||\mathbf{d}_j|| < \infty$. The summation is multiplied by $||PL||$, therefore it can affect the upper bound of the error norm of each iteration. Looking at eqn. 4.59, $||PL|| = |K|\,||P\mathbf{J}||$, where $\mathbf{J}$ is the learning matrix, L_e, divided by K. From this it can be deduced that larger magnitudes of K can increase the maximum iteration error norm for model-less control with stochastic disturbance.

Assuming the disturbance, d_j is Gaussian noise with zero mean and variance of λ^2, and taking the expected value of eqn. 4.84 gives:

$$E(||\mathbf{e}_j||) \leq ||(I-PL)||^j E(||\mathbf{e}_0||) + \left(||(I-PL)||^{j-1} + ||PL||\sum_{i=1}^{j-1}||(I-PL)||^{j-i-1} + 1\right) N\lambda^2 \tag{4.85}$$

as

$$E(||\mathbf{d}_j||) = E(d_j(1)^2 + ... + d_j(N)^2) \tag{4.86}$$

$$= E(d_j(1)^2) + ... + E(d_j(N)^2) \tag{4.87}$$

$$= N\lambda^2 \tag{4.88}$$

Taking eqn. 4.85 to convergence, so $j \to \infty$, gives:

$$E(||\mathbf{e}_\infty||) \leq \left(||PL|| \sum_{i=0}^{\infty} ||(I-PL)||^i + 1 \right) N\lambda^2 \tag{4.89}$$

The summation term is a geometric series that converges to

$$\sum_{i=0}^{\infty} ||(I-PL)||^i = \frac{1}{1-||(I-PL)||} \tag{4.90}$$

which gives

$$E(||\mathbf{e}_\infty||) \leq \left(\frac{||PL||}{1-||(I-PL)||} + 1 \right) N\lambda^2 \tag{4.91}$$

or using $||PL|| = |K|\,||P\mathbf{J}||$:

$$E(||\mathbf{e}_\infty||) \leq \left(\frac{||P\mathbf{J}||}{1-||(I-PL)||} + 1 \right) |K| N\lambda^2 \tag{4.92}$$

which gives the mean error norm upper bound to be a function of the noise variance, the iteration length, the system learning filter and the gain. If $||(I-PL)||$ is decreased it may decrease the mean error norm upper bound, as $0 < ||(I-PL)|| < 1$. However, it may be counteracted by an increase in $||PL||$ as there is no bounding on it. This can increase the mean error norm upper bound.

4.3.5 Implementation

The model-less control is first simulated on the ARMAX model found in Section 4.2.2 then is implemented on the single cylinder engine. Four values of K are used to

compare to the results predicted in Fig. 4.15. The four values are $K = 0.9$, 1.12, 1.3 and 1.8. From Fig. 4.15 the optimal convergence time should occur with $K = 1.12$ and $K = 0.9$ and $K = 1.3$ should have similar convergence time. The $K = 1.8$ case should be close to instability. Then these cases are experimentally implemented on the CFR engine. Fig. 4.16 shows the iteration error norm for the four cases for both experimental and simulated results. In Fig. 4.16d the number of iterations plotted was increased to 30 for the simulation to show that the system was stable as this is not clear when only viewing 20 iterations. The other K values behaved similarly, as expected. From inspection the convergence time of Figs. 4.16a and 4.16b are the same. Fig. 4.16c, however, has longer convergence time and has a unique aspect of an increase in CA50 error norm from the first to second iteration for the simulation results. This is thought to be a result of the noise feeding through the control as given in eqn. 4.85. The close similarity of experiment and simulation indicates two things. One, the ARMAX model used in the simulation seems to captures the system response well. Two, since this system model (here ARMAX) capture the dynamics, an ILC control can be tuned in simulation and directly implemented on the engine without further tuning.

The controller performance evaluations for the experimental results are given in Tables 4.4 and 4.5. The results of the actual engine performance mimic the ARMAX model well as shown in Fig. 4.16. The major discrepancies are the lack of second iteration increase in CA50 error norm observed in Fig. 4.16c, and the CA50 convergence in $K = 1.8$ is more prominent for experimental results as shown in Fig. 4.16c compared to the simulation. These are likely a result of the system's noise variance being not as large as predicted by the ARMAX modeling therefore the noise that is fed into the input is less. Comparing the results in Tables 4.4 and 4.5, the best K value was 0.9 with 1.12 being slightly less optimal due to the noise feedback as shown in eqn. 4.91. Fig. 4.17 gives the control inputs and outputs for the $K = 1.12$

case. From this figure the large input variance can be seen which is the most probable reason for the $K = 0.9$ outperforming the $K = 1.12$. An experimental test is done with $K = 2$ but the system is unstable, as expected, and all inputs hit saturation after 2 iterations so the results will not be shown.

Table 4.4: Experimental model-less ILC performance results for CA50 error norm convergence.

ILC	mean($\|\|e_{\text{CA50}}\|\|_2$)	std($\|\|e_{\text{CA50}}\|\|_2$)	$j_{conv,\,\text{CA50}}$
$K = 0.9$	5.13	0.794	2
$K = 1.12$	5.21	0.406	3
$K = 1.3$	6.31	0.573	5
$K = 1.8$	18.9	3.18	N/A

Table 4.5: Experimental model-less ILC performance results for IMEP error norm convergence.

ILC	mean($\|\|e_{\text{IMEP}}\|\|_2$)	std($\|\|e_{\text{IMEP}}\|\|_2$)	$j_{conv,\,\text{IMEP}}$
$K = 0.9$	40.4	5.00	2
$K = 1.12$	43.8	6.67	3
$K = 1.3$	43.4	4.70	4
$K = 1.8$	98.9	21.0	N/A

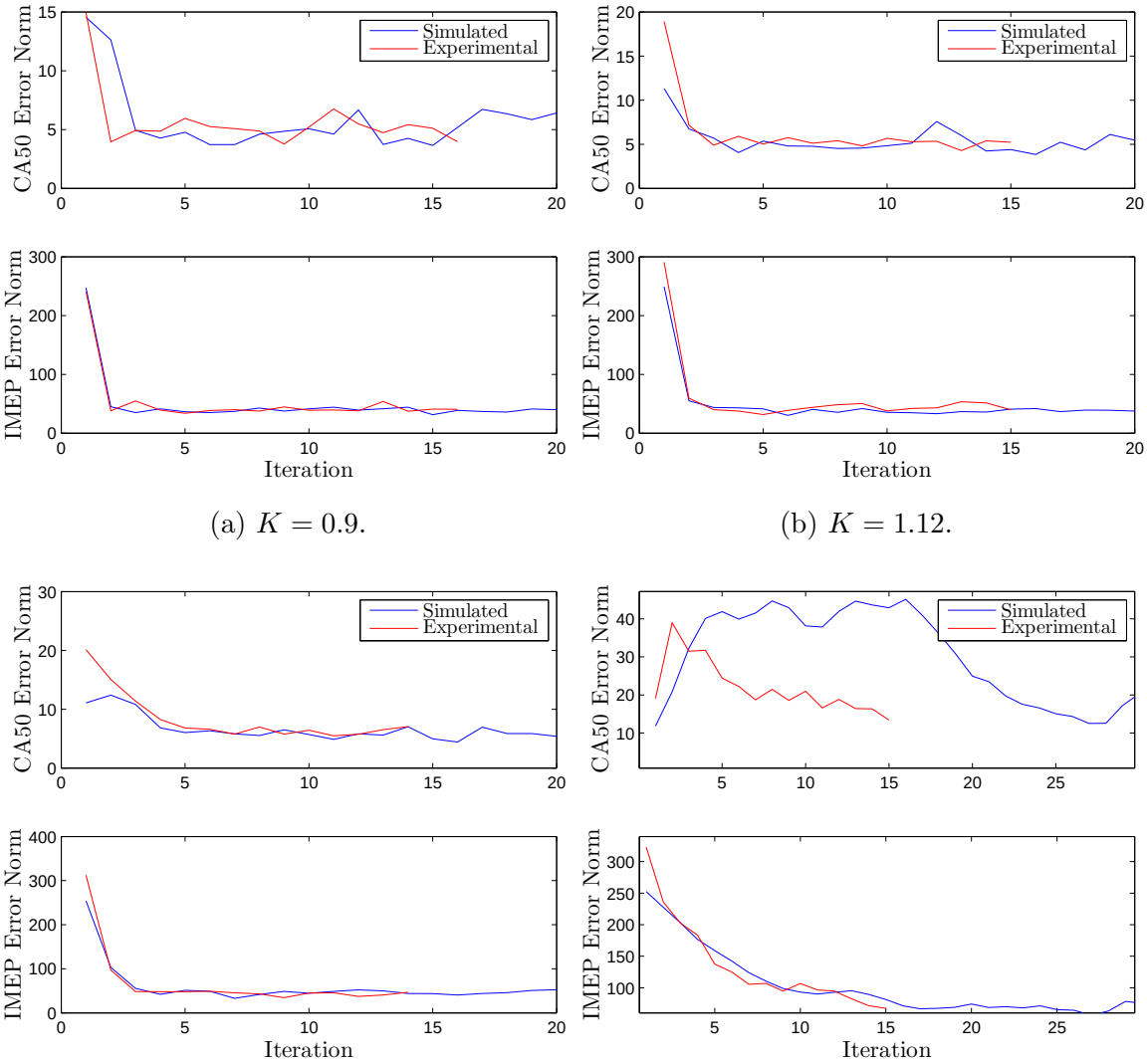

(a) $K = 0.9$.

(b) $K = 1.12$.

(c) $K = 1.3$.

(d) $K = 1.8$.

Figure 4.16: Simulation and experimental error norm using model-less control for varying values of K for operating conditions given in Table 3.7.

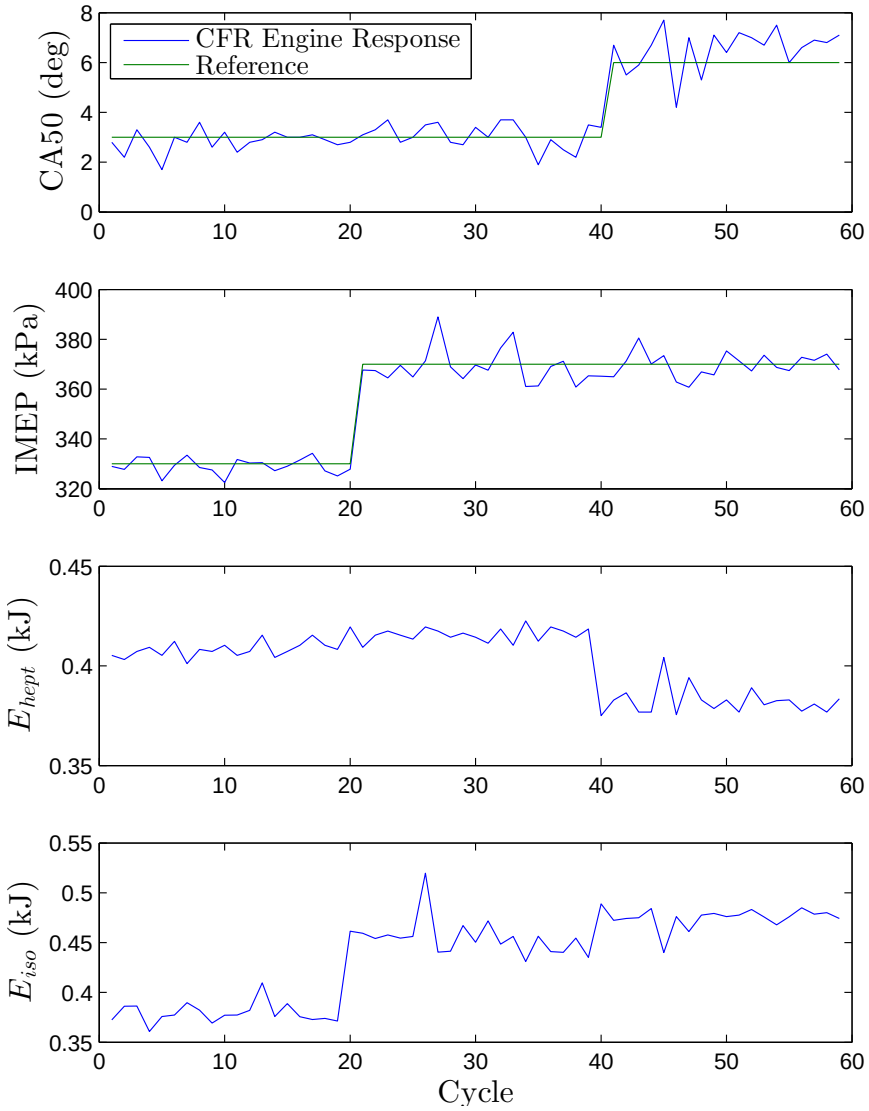

Figure 4.17: Experimental final iteration control responses with $K = 1.12$ for operating conditions given in Table 3.7.

4.4 Filter Design

For both the norm optimal and model-less control, noise has a prominent effect on convergence time and mean converged iteration error norm. To mitigate this the use of filters coupled with the ILC is investigated. A common implementation for ILC filters is in the form a Q filter Bristow et al. [2006], denoted Q_f here so as not to be confused with the Q weighting matrix in Section 4.3.1. The implementation is:

$$\mathbf{u}_{j+1} = Q_f(\mathbf{u}_j + L\mathbf{e}_j) \tag{4.93}$$

with L being a learning matrix. This has the effect of turning the ILC off for frequencies chosen by the Q_f and have perfect tracking for frequencies not affected by the Q_f Bristow et al. [2006]. The learning and forgetting matrices, L_e and L_u respectively, in eqn. 4.34 are:

$$L_u = Q_f \tag{4.94}$$

$$L_e = Q_f\, L \tag{4.95}$$

where L is designed for optimal stability or monotonic convergence as in Sections 4.3.1 and 4.3.2. Since $L_u \neq I$, the system is no longer guaranteed to converge to zero error Ahn et al. [2007a]. The effects on stability are found by re-writing eqn. 4.35 as

$$\mathbf{u}_{j+1} = Q_f(I - L\,P)\mathbf{u}_j + Q_f\, L(\mathbf{y}_r - \mathbf{d}_j)) \tag{4.96}$$

Similarly, if $\rho(Q_f(I - L\,P)) \leq 1$ the system is stable. If the filter and learning gain are causal, i.e. lower triangular and Toeplitz, P, L and Q_f commute Bristow et al. [2006]. Then applying Gelfand's formula Lax [2002] the following result is obtained

$$\rho(Q_f(I - L\,P)) \leq \rho(Q_f)\,\rho((I - L\,P)) \tag{4.97}$$

The eigenvalues of a causal Q_f are the first coefficients of the filter. Therefore $\rho(Q_f)$ is likely to be less than 1 if the filter has unity gain, which is the sum of all the coefficients, and is stable. Using these two, if L is designed to be stable and causal, the system with a causal filter is guaranteed to be stable. This can be extended to non-causal learning matrices as long as LP is lower triangular and Toeplitz, thereby keeping the commutativity property between Q_f and $I - LP$.

The application of a causal filter introduces a phase-lag and thereby nullifies one of the major advantages of an ILC, the ability to react to future inputs without a delay. With an ILC system, each iteration is considered as a whole thus allowing the use of non-causal filters that have no phase lag. The disadvantage is the lower triangular property is lost thus breaking the commutativity property making the convergence criteria more complicated Bristow et al. [2006]. This is done by comparing the asymptotic error, e_∞, assuming the disturbance is constant between iterations, as Bristow et al. [2006]

$$\mathbf{e}_\infty = [I - P[I - Q_f(I - LP)]^{-1}Q_f L](\mathbf{y}_d - \mathbf{d}) \tag{4.98}$$

with the iteration error, giving

$$\mathbf{e}_\infty - \mathbf{e}_{j+1} = PQ_f(I - LP)P^{-1}(\mathbf{e}_\infty - \mathbf{e}_{j+1}) \tag{4.99}$$

Then taking the 2-norm of the system the following is obtained

$$||\mathbf{e}_\infty - \mathbf{e}_{j+1}|| = ||PQ_f(I - LP)P^{-1}(\mathbf{e}_\infty - \mathbf{e}_{j+1})|| \tag{4.100}$$

$$||\mathbf{e}_\infty - \mathbf{e}_{j+1}|| = ||PQ_f(I - LP)P^{-1}||\,||(\mathbf{e}_\infty - \mathbf{e}_{j+1})|| \tag{4.101}$$

From eqn. 4.101, the error will monotonically converge to $\mathbf{e}_\infty$ if $||PQ_f(I - LP)P^{-1}|| < 1$ Bristow et al. [2006]. This assumes that the P matrix is invertible, which is not the case for a system with input delay like the one for the CFR engine. The alternative is to check stability and optimal design by testing the filters on the ARMAX model since, in Sections 4.3.1 and 4.3.2, the ARMAX model predicted the engine performance well.

4.4.1 Gaussian

A Gaussian filter is the first non-causal filter to be tested. This is a common filter used in image processing Haddad and Akansu [1991]. It involves weighting the future and past inputs with a Gaussian function as:

$$w(x) = a\, e^{\frac{-x^2}{\beta}} \tag{4.102}$$

where a is the scaling value, which is set to ensure the filter gain is unity, and β is used to determine how quickly the system responds. The Gaussian function is

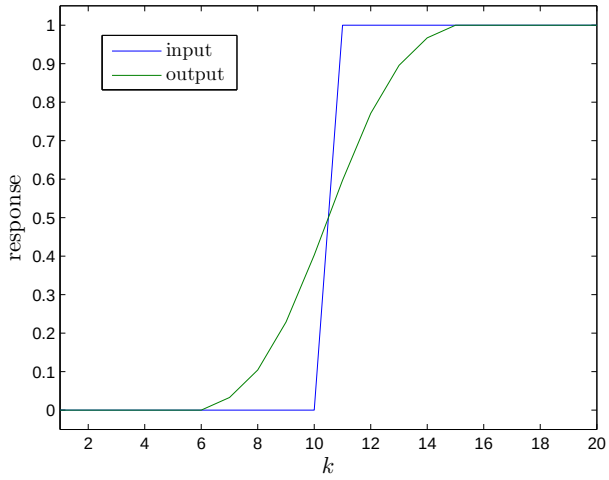

Figure 4.18: Gaussian filter step response with $O = 9$ and $\beta = 9$.

approximated with an O^{th} order filter as:

$$\begin{aligned} y(k) =& w(n)x(k-n) + w(n-1)x(k-(n-1)) + ... \\ & ... + w(1)x(k-1) + w(0)x(k) + w(1)x(k+1) + ... \\ & ... + w(n-1)x(k+(n-1)) + w(n)x(k-n) \end{aligned} \tag{4.103}$$

with y being the filter output, x being the filter input and n being a function of the filter's order, O, as $n = (O-1)/2$. The filter's step response is shown in Fig. 4.18. The filter response is shown to react to the step before it occurs, thereby minimizing the total error; this is a non-casual filter property.

The filter is then tested in simulation with the model-less control using the optimal gain of $K = 1.12$ on the ARMAX model. The filter is compared to the system without a filter and to filters where the parameters are O and β. Choosing a base point of $\beta = 9$ and $O = 9$, β is increased then decreased with respect to the base point and the same procedure is done with the filter order. The results are shown in Fig. 4.19. Note: the order, O, must always be odd for the Gaussian filter so that n is always a

whole number. The controller performance evaluations are given Tables 4.6 and 4.7. The addition of the filter has minimal effects on the converged performance shown in Tables 4.6 ans 4.7. Varying the filter parameters also does not significantly affect ILC convergence time as shown in Fig 4.19. The base point is chosen to test on the engine as varying filter parameters did not effect performance.

Table 4.6: Simulation model-less ILC performance results for CA50 error norm convergence with Gaussian filter.

ILC	mean($\|\|e_{\text{CA50}}\|\|$)	std($\|\|e_{\text{CA50}}\|\|$)	$j_{conv,\,\text{CA50}}$
Filter less	5.15	1.02	4
$\beta = 9$, O=9	4.86	1.06	2
$\beta = 6$, O=9	4.86	0.96	4
$\beta = 12$, O=9	4.97	1.07	3
$\beta = 9$, O=7	4.89	1.01	3
$\beta = 9$, O=15	5.05	1.16	4

Table 4.7: Simulation model-less ILC performance results for IMEP error norm convergence with Gaussian filter.

ILC	mean($\|\|e_{\text{IMEP}}\|\|$)	std($\|\|e_{\text{IMEP}}\|\|$)	$j_{conv,\,\text{IMEP}}$
Filter less	39.4	3.95	3
$\beta = 9$, O=9	42.0	3.26	3
$\beta = 6$, O=9	40.4	3.32	3
$\beta = 12$, O=9	43.2	3.24	3
$\beta = 9$, O=7	41.1	3.42	3
$\beta = 9$, O=15	42.5	3.34	5

4.4.2 Zero-Phase

A zero-phase filter is a filter, for example an infinite impulse response filter, where after the first pass the output is reversed and put through the filter again. Then the output of the second pass is reversed and considered the output of the zero-phase filter. The benefit of this is the phase lag cancels itself through the second pass. As a result of two passes being performed, the magnitude response is squared Mitra [2006]. A plot of the step response of a zero-phase 8^{th} order Butterworth filter run forward and

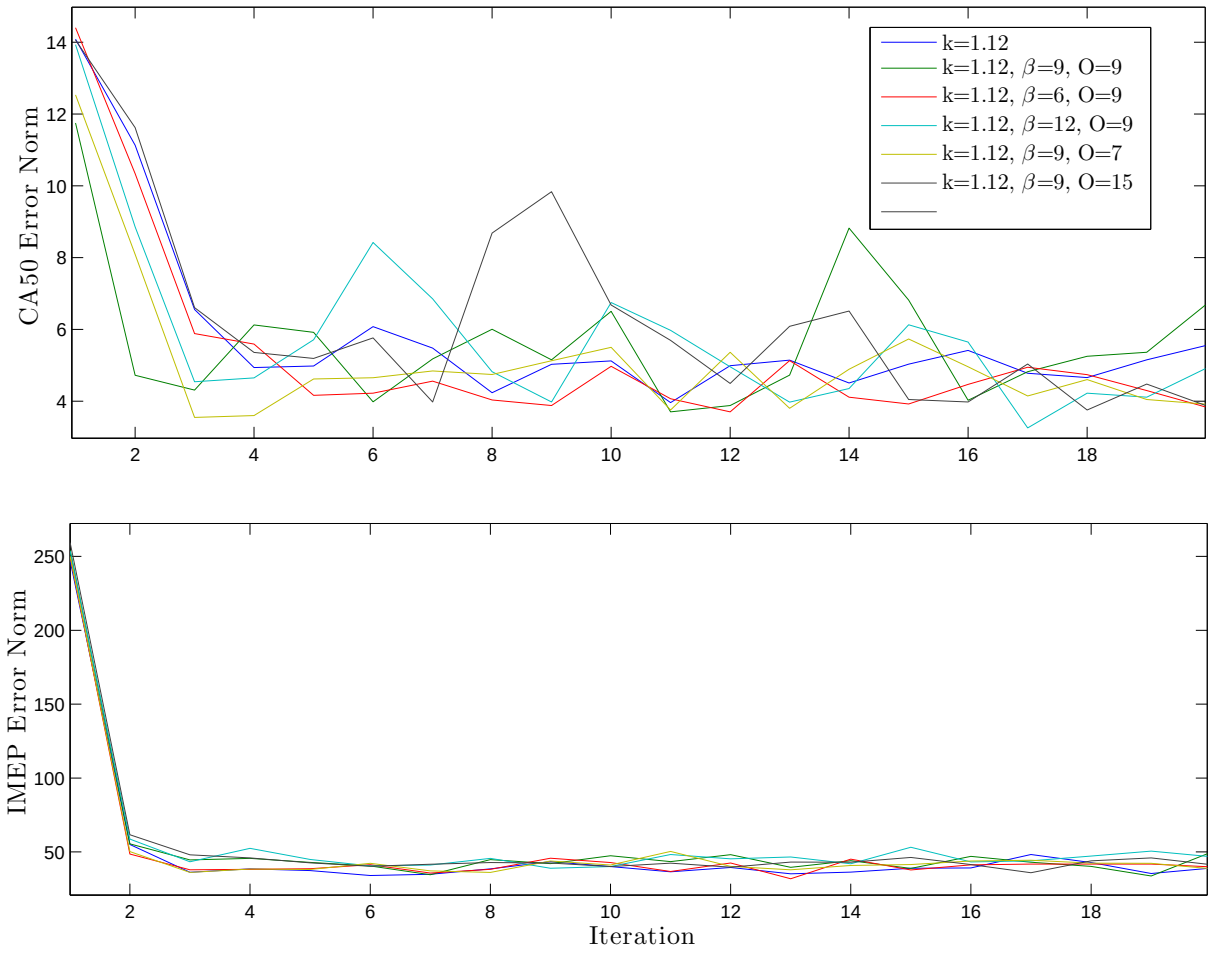

Figure 4.19: ARMAX simulation iteration error norm for model-less ILC with Gaussian filter with varying β and order.

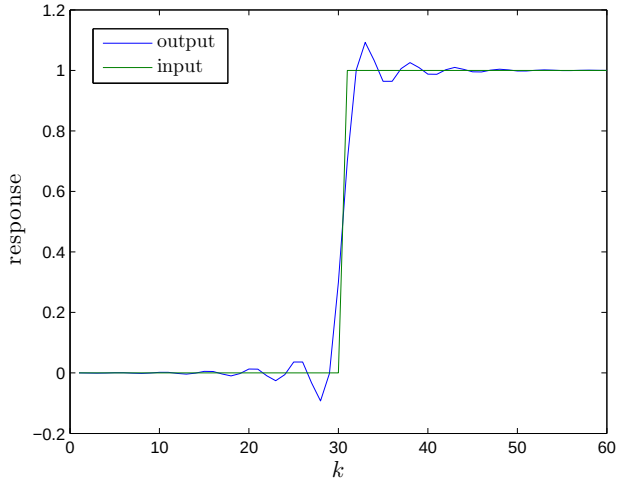

Figure 4.20: Zero-phase 8$^{\text{th}}$ order Butterworth filter step response.

backwards is shown in Fig. 4.20. Comparing this figure to Fig. 4.18, the overshoot and subsequent ripples are the disadvantage of using a zero-phase Butterworth compared to a Gaussian filter. The benefit of a zero-phase Butterworth filter is the ability to directly choose the cut-off frequency for the Q_f. To select the cut-off frequency, a periodogram of the CA50 error is calculated as it has the highest noise levels. The first iteration error is compared to the final iteration error periodograms of the model-less ILC CFR engine response in Fig. 4.21. The final iterations error is caused by the noise disturbance only, as the system error has converged to zero as seen in eqn. 4.84. Therefore the periodogram of the final iteration error contains only frequencies of the noise. This is in contrast to the first iteration error where the system has not converged and the frequencies for the learning filter to update the input are present. The filter should not cut out any frequencies that are present in the first iteration periodogram but not in the final, as these are the frequencies that are being utilized in the control while all others are from the noise of the system. By comparing Figs. 4.21a and 4.21b the control seems to be dominant in the 0 to 0.2 $\sim$ 0.4 normalized frequency range.

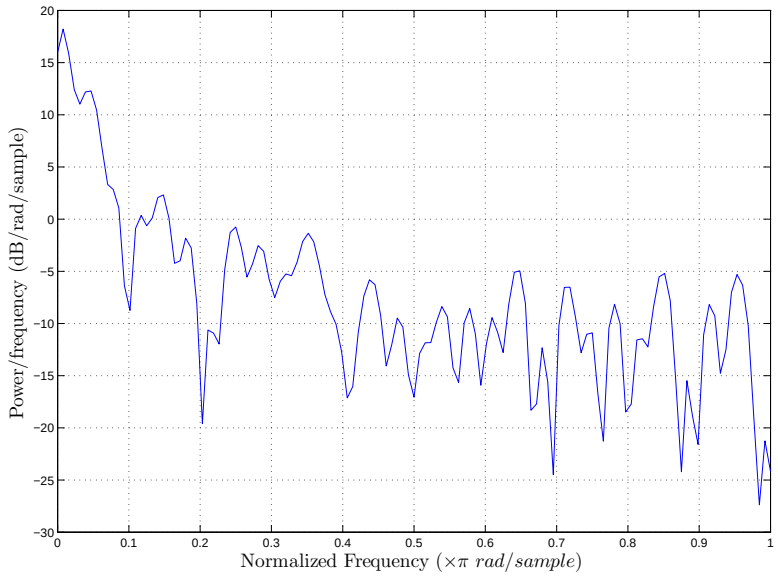

(a) First iteration.

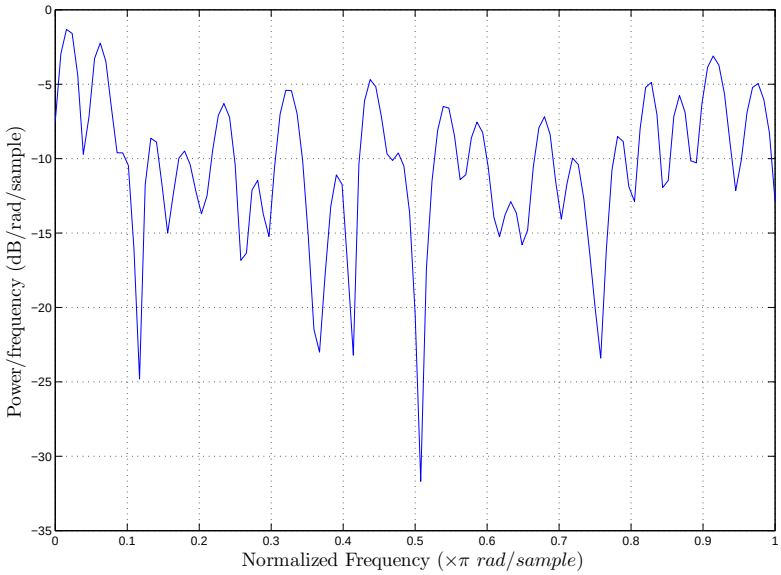

(b) Final iteration.

Figure 4.21: Periodogram of experimental CA50 iteration error using model-less ILC with $K = 1.12$ for first and final iteration with sampling per cycle.

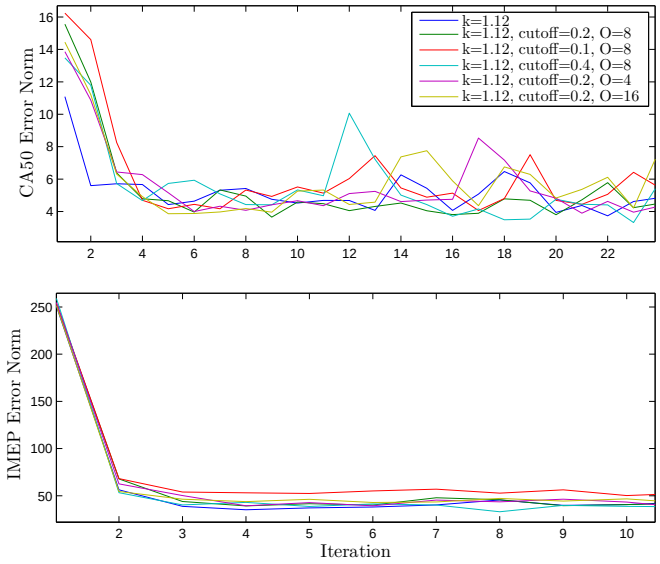

Figure 4.22: ARMAX simulation iteration error norm for model-less ILC with zero-phase Butterworth filter with varying cut-off frequency and order.

Similar to Section 4.4.1, the zero-phase Butterworth filter was tested in simulation using the model-less ILC with the optimal gain on the ARMAX model. The zero-phase Butterworth filter is created from a low-pass Butterworth filter of order O. It is tested using a base point with a cut-off normalized frequency, f_{cut}, of 0.2 with an order, O of 8. The filter's parameters, cut-off frequency and order, are varied to find optimal values. The controller without the filter is also given for comparison. The results are shown in Fig. 4.22 with controller performance evaluation given in Tables 4.8 and 4.9. For CA50, the application of the filter is not significant. For IMEP, however, the filter with cut-off frequency of 0.4 seems to out-perform the others. By inspecting Fig. 4.22 the convergence time for all is relatively similar. The optimal filter parameters are taken as cut-off frequency of 0.4 and order of 8.

Table 4.8: Simulation model-less ILC performance results for CA50 error norm convergence with zero-phase Butterworth filter.

ILC	mean($\|\|e_{\text{CA50}}\|\|$)	std($\|\|e_{\text{CA50}}\|\|$)	$j_{conv,\,\text{CA50}}$
Filter less	5.25	1.12	2
$f_{cut} = 0.2$, O=8	5.11	1.13	4
$f_{cut} = 0.1$, O=8	5.51	0.98	4
$f_{cut} = 0.4$, O=8	4.89	1.12	3
$f_{cut} = 0.2$, O=4	4.90	0.9	5
$f_{cut} = 0.2$, O=16	5.08	1.08	4

Table 4.9: Simulation model-less ILC performance results for IMEP error norm convergence with zero-phase Butterworth filter.

ILC	mean($\|\|e_{\text{IMEP}}\|\|$)	std($\|\|e_{\text{IMEP}}\|\|$)	$j_{conv,\,\text{IMEP}}$
Filter less	39.4	3.54	3
$f_{cut} = 0.2$, O=8	43.2	3.22	3
$f_{cut} = 0.1$, O=8	55.0	3.23	3
$f_{cut} = 0.4$, O=8	38.0	3.46	3
$f_{cut} = 0.2$, O=4	42.6	3.31	4
$f_{cut} = 0.2$, O=16	44.1	3.29	3

4.4.3 Implementation

The optimal filters are then implemented on the CFR engine. Each optimal filter, Gaussian and zero-phase Butterworth, is tested with each control style, model-less and norm optimal. Previously, the r was increased for the norm optimal to minimize the noise effects. Here the smallest r value, which is 1, is used with the filter. The optimal gain, $K = 1.12$, for the model-less control is used with filter. This is chosen over $K = 0.9$, even though it had similar performance, since the better performance of the lower gain is due to the increased noise transfer occurring at the higher gain as given in eqn. 4.84, which should be reduced by the filter. This gives a total of four experiments. The results of these experiments' error norms are given in Fig. 4.23 with the ILC performance evaluations in Tables 4.10 and 4.11. The convergence time for all are similar. The standard deviations of the error norm for the zero-phase Butterworth filter results are lower than the Gaussian filters' indicating that the noise

is not affecting the error as much with the zero-phase Butterworth filter and the final iteration is more consistent. For CA50 mean error norm, all values are within the standard deviation of each other and are therefore considered relatively equal. The IMEP error norm is considerably lower for the zero-phase Butterworth filter results with the norm-optimal with zero-phase Butterworth filter out-performing the rest.

Table 4.10: Experimental ILC performance results for CA50 error norm convergence with filter.

ILC	mean($\|\|e_{\text{CA50}}\|\|$)	std($\|\|e_{\text{CA50}}\|\|$)	$j_{conv,\,\text{CA50}}$
model-less Gaussian	4.43	0.578	3
model-less zero-phase Butterworth	4.38	0.460	3
norm-optimal Gaussian	4.41	0.533	2
norm-optimal zero-phase Butterworth	4.28	0.336	3

Table 4.11: Experimental ILC performance results for IMEP error norm convergence with filter.

ILC	mean($\|\|e_{\text{IMEP}}\|\|$)	std($\|\|e_{\text{IMEP}}\|\|$)	$j_{conv,\,\text{IMEP}}$
model-less Gaussian	44.3	3.33	2
model-less zero-phase Butterworth	38.3	4.92	3
norm-optimal Gaussian	43.3	3.80	2
norm-optimal zero-phase Butterworth	34.7	3.22	2

The final iteration's control signals are given in Fig. 4.24 and the difference between the filters can be noticed. The difference of the control strategies, i.e. model-less and norm-optimal, are not seen as they primarily affect the convergence and not the final iteration. The filters' effects can be seen in the system inputs, E_{iso} and E_{hept} in Fig. 4.24. With the Gaussian filter the inputs are smooth and relatively constant while the zero-phase Butterworth has ripples throughout the signal. With both types of filters, the output reacts to the step before it happens more prominently compared to the case without a filter. This is one of the benefits of ILC as it allows the error caused by the step to be distributed before and after when the step occurs thereby minimizing the maximum error observed.

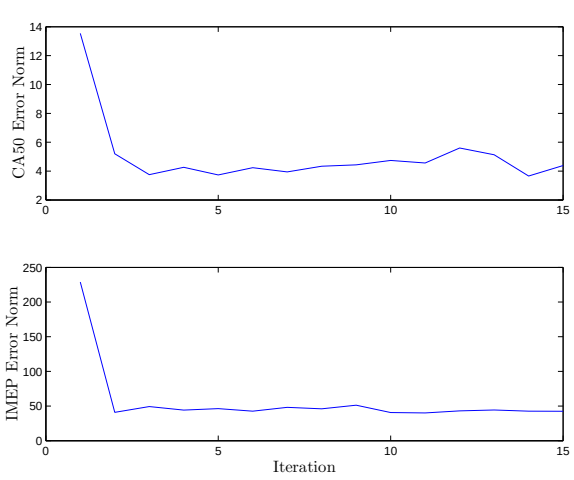

(a) $K = 1.12$ and Gaussian filter.

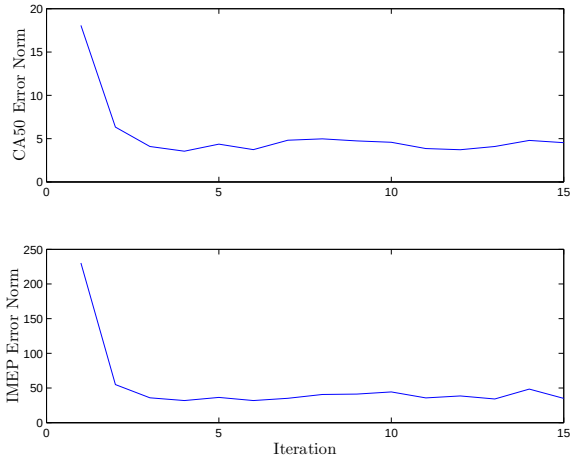

(b) $K = 1.12$ and zero-phase Butterworth filter.

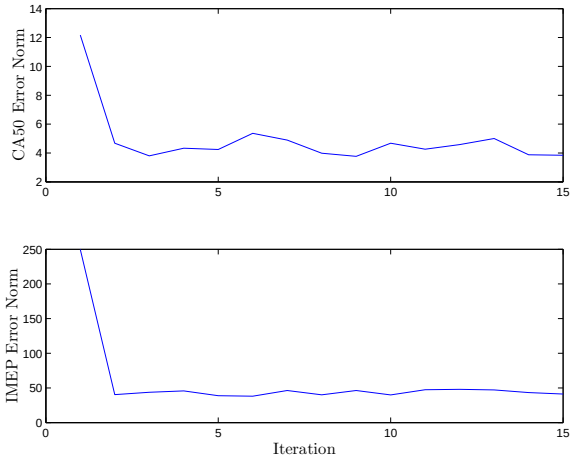

(c) $r = 1$ and Gaussian filter.

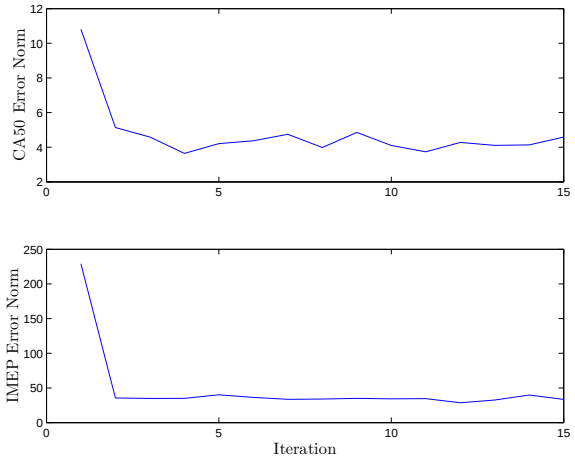

(d) $r = 1$ and zero-phase Butterworth filter.

Figure 4.23: Model-less and norm optimal ILC experimental iteration error norms with Gaussian and zero-phase Butterworth filter.

In comparison to the rest, including results from ILCs without filters, the best three ILC setups are the model-less with zero-phase Butterworth, norm-optimal with $r = 1$ with zero-phase Butterworth filter, and norm-optimal with $r = 1000$ shown in Fig. 4.25. The performance of each is given in Tables 4.12 and 4.13. These ILCs' performances will be tested for robustness with changes in operating conditions and fuel selection in the next chapter.

Table 4.12: Experimental ILC base point performance results for CA50 error norm convergence.

ILC	mean($\|\|e_{\text{CA50}}\|\|$)	std($\|\|e_{\text{CA50}}\|\|$)	$j_{conv,\,\text{CA50}}$
$r = 1000$	5.36	0.494	3
model-less zero-phase Butterworth	4.38	0.460	3
norm-optimal zero-phase Butterworth	4.28	0.336	3

Table 4.13: Experimental ILC base point performance results for IMEP error norm convergence.

ILC	mean($\|\|e_{\text{IMEP}}\|\|$)	std($\|\|e_{\text{IMEP}}\|\|$)	$j_{conv,\,\text{IMEP}}$
$r = 1000$	37.7	6.64	2
model-less zero-phase Butterworth	38.3	4.92	3
norm-optimal zero-phase Butterworth	34.7	3.22	2

4.5 PI Comparison

For reference purposes the ILC results are compared to a PI controller which is implemented as:

$$e(k) = y_d(k) - y(k) \tag{4.104}$$

$$u(k) = K_p\, e(k) + K_i \sum_{i=0}^{k} e(i) \tag{4.105}$$

where $u(k)$ and $y(k)$ are defined in eqn. 4.32 and K_p and K_i are 2×2 matrices.

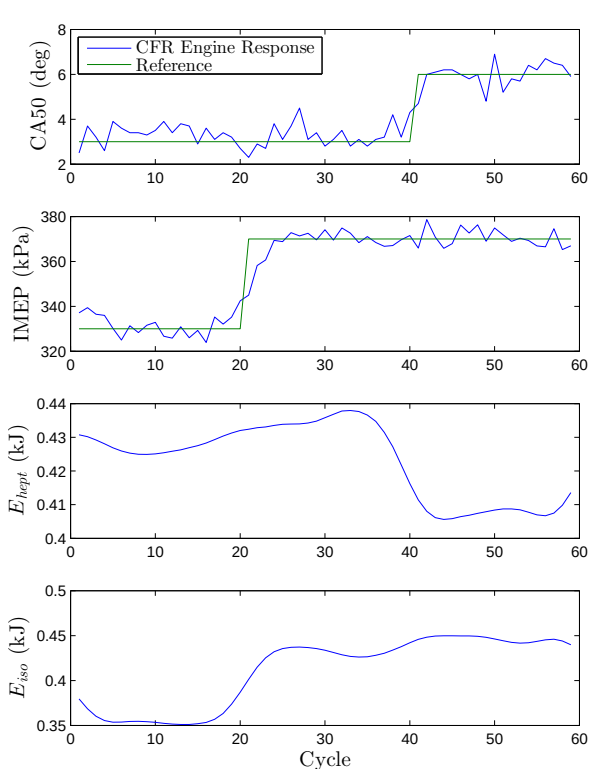

(a) $K = 1.12$ and Gaussian filter.

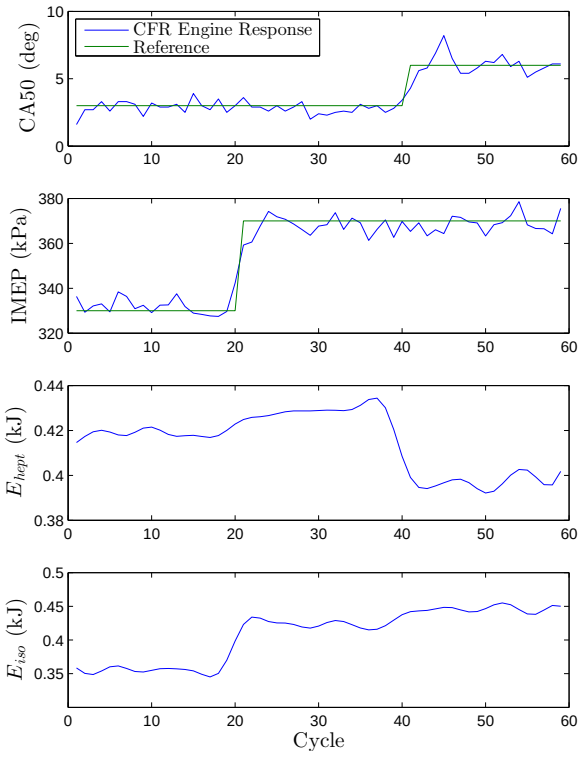

(b) $K = 1.12$ and zero-phase Butterworth filter.

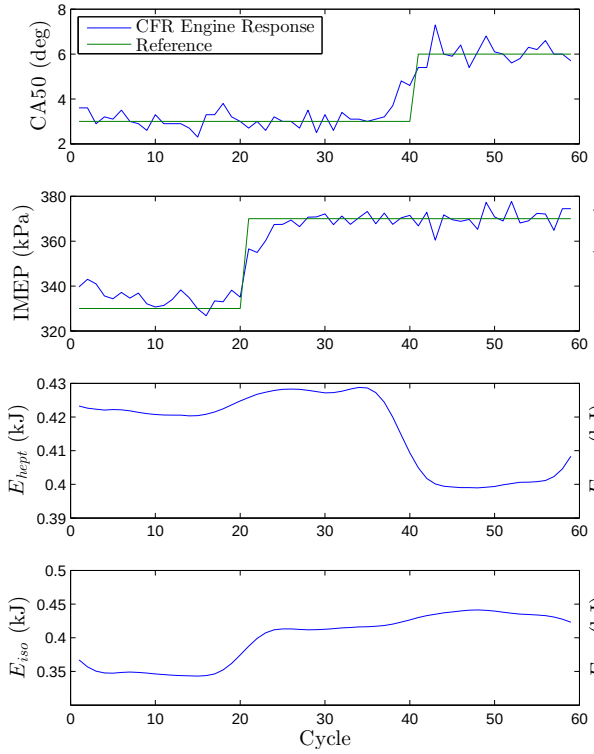

(c) $r = 1$ and Gaussian filter.

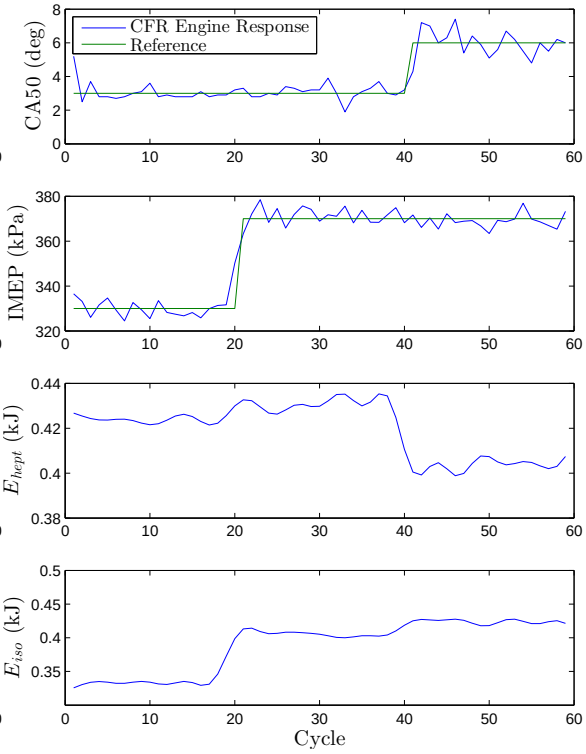

(d) $r = 1$ and zero-phase Butterworth filter.

Figure 4.24: Model-less and norm optimal ILC experimental final iteration control responses with Gaussian and zero-phase Butterworth filter.

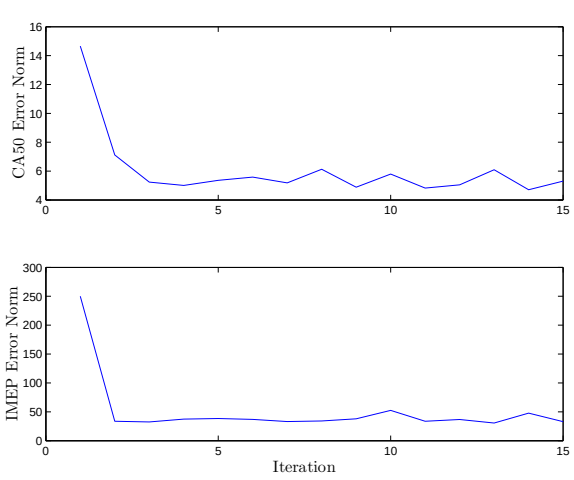

(a) $r = 1000$

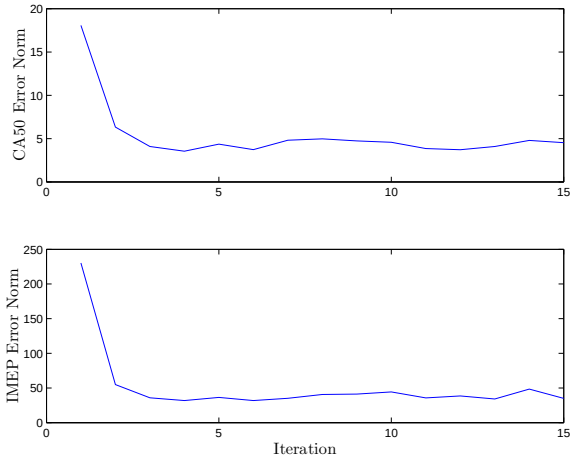

(b) $K = 1.12$ and zero-phase Butterworth filter.

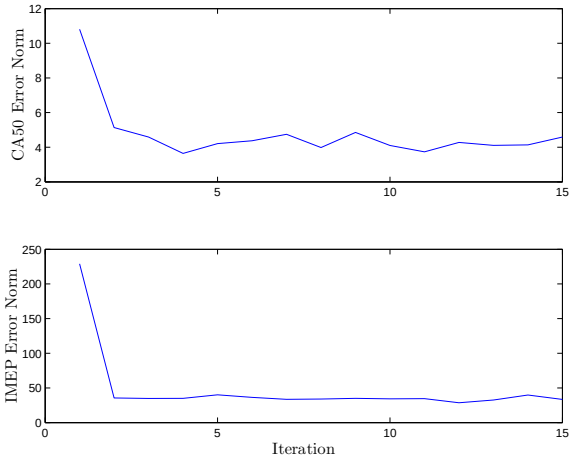

(c) $r = 1$ and zero-phase Butterworth filter.

Figure 4.25: Model-less and norm optimal ILC experimental iteration error norms base case.

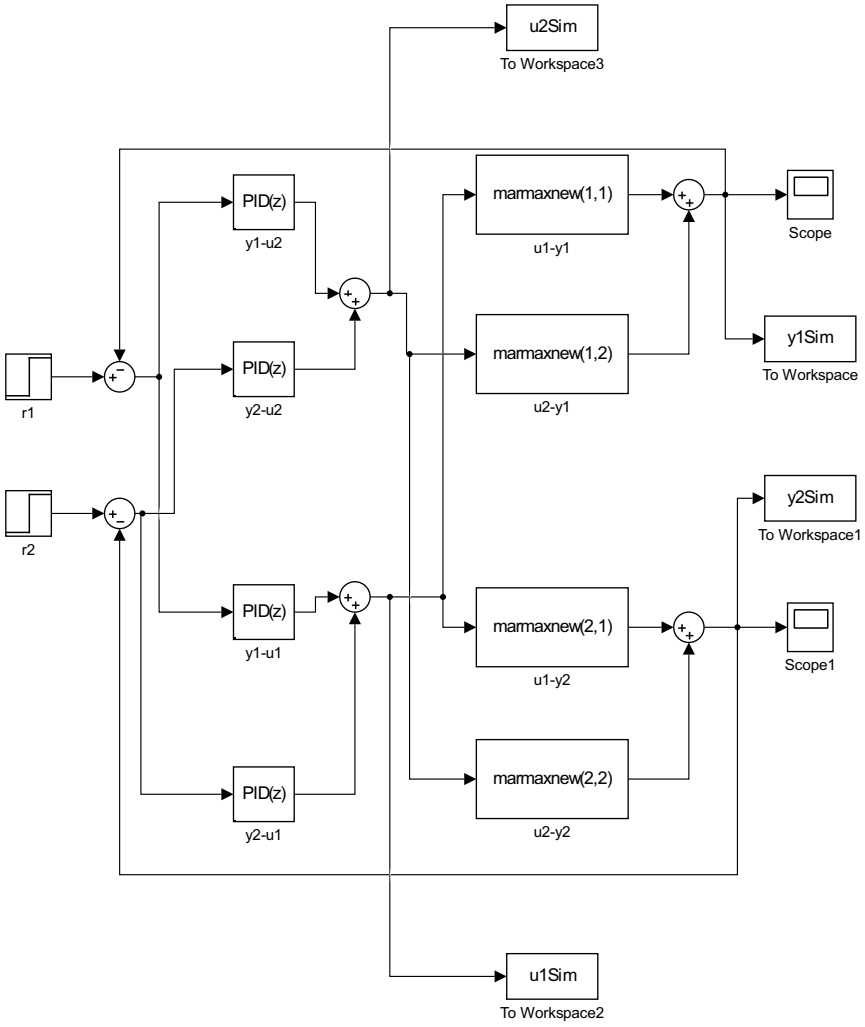

Figure 4.26: Simulink model of PI control with ARMAX model.

Simulation is used to tune K_p and K_i using a Simulink model with the ARMAX model as shown in Fig. 4.26. The gains are tuned manually for near deadbeat response for each step (without noise), then noise is added and the tuning is repeated. The simulation response is shown in Fig. 4.27 with the tuned gains of:

$$K_p = \begin{bmatrix} -0.012 & 0.0006 \\ 0.012 & 0.0012 \end{bmatrix}, \; K_i = \begin{bmatrix} -0.010 & 0.0008 \\ 0.008 & 0.0010 \end{bmatrix} \tag{4.106}$$

Note: The gains corresponding to E_{hept} with CA50 are negative due to this response having a negative sensitivity. When the PI controller is implemented on the CFR engine using the gains in eqn. 4.106, the system is unstable. The gains have to be manually tuned to the following values

$$K_p = \begin{bmatrix} -0.0050 & 0.0001 \\ 0.010 & 0.0003 \end{bmatrix}, \; K_i = \begin{bmatrix} -0.006 & 0.0003 \\ 0.003 & 0.0010 \end{bmatrix} \tag{4.107}$$

which gives the response found in Fig. 4.28. This indicates that the ARMAX model is not sufficient for feedback control design. The ILC is The error norms for CA50 and IMEP are 5.38 and 62.6, respectively. These are significantly higher than any of the converged mean error norms for an ILC with filter, which had maximum error norms of 4.43 and 44.3 for CA50 and IMEP respectively, and marginally higher than the optimal ILCs without filters, e.g. $K = 1.12$ for model-less and $r = 1000$ for norm-optimal, which had maximum error norms of 5.36 and 43.8 for CA50 and IMEP respectively. With convergence occurring in less than 4 iterations, this shows the utility of the application of an ILC for repetitive control of an HCCI engine.

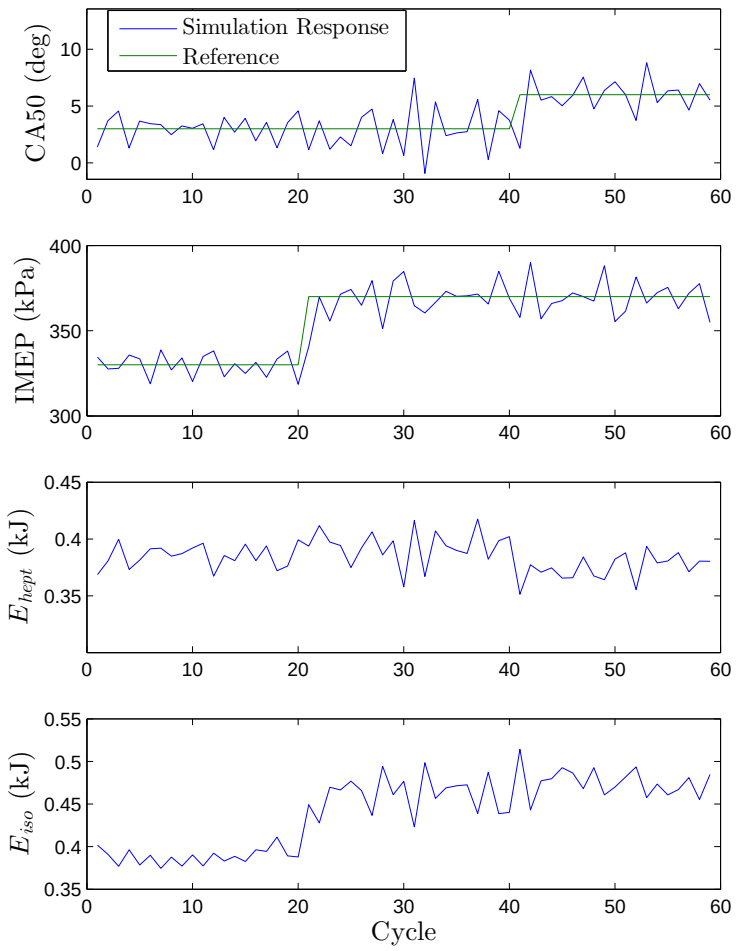

Figure 4.27: Simulated PI control for operating conditions given in Table 3.7.

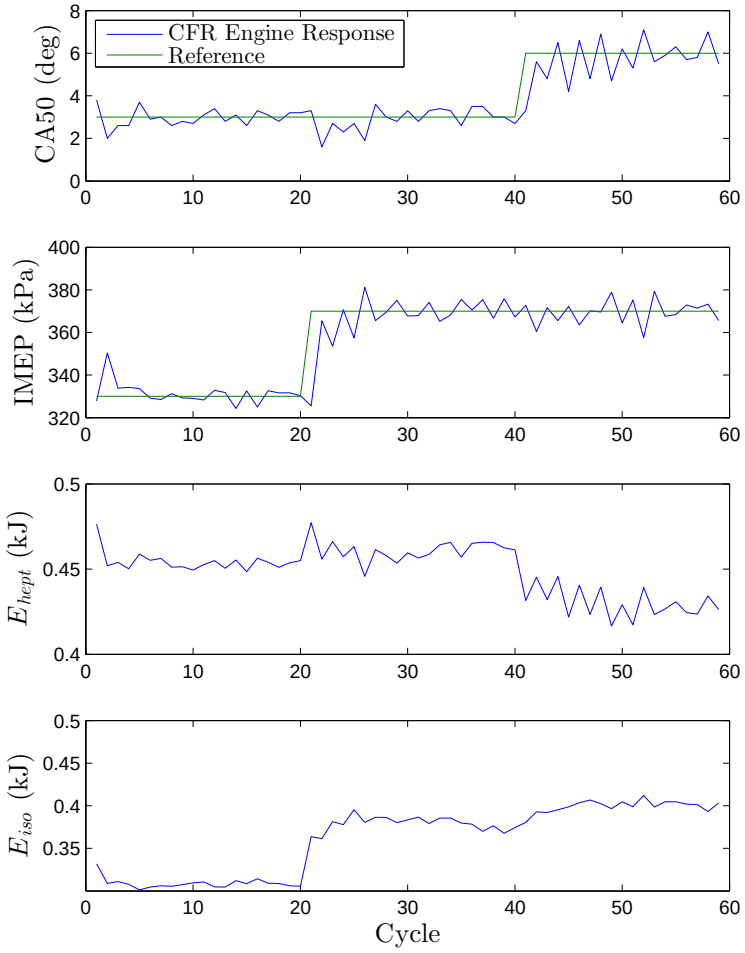

Figure 4.28: Experimental PI control responses with adjusted gains for operating conditions given in Table 3.7.

4.6 Summary

A steady-state domain exploration and system identification is performed using energy of iso-octane and n-heptane as inputs and CA50 and IMEP of HCCI combustion as outputs for a CFR engine. A repeated step response is input and iterative learning control is used on the sequence of these iterations.

The domain exploration found that CA50 and IMEP are approximately linear within a prescribed operating region. The system identification found a dynamic model that is able to predict system response with good accuracy. Also the Markov parameters are found from the system identification.

With the dynamic model, a norm-optimal ILC is designed. The norm-optimal ILC requires a selection for weighting matrices. This ILC is then simulated on the dynamic model for selecting the best ILC then tested on the engine. The experimental results agreed well with the simulation. Then a new method for designing an ILC was developed, which reduces the multi-input multi-output control problem to one requiring a single gain selection. The stability of the system to this gain was investigated as well as its effects on noise transfer. The method was then simulated on the dynamic model and experimentally tested for varying values of the gain. The simulation, once again, agrees well with the experimental results.

To attenuate the noise in the system, two non-causal filter are implemented on the ILCs. Since the dynamic model agrees with the experimental results, the filters are optimized in simulation. The best of each filter type are chosen then tested experimentally on the engine. The three best ILCs are then chosen to be tested further.

Finally a PI controller is designed and simulated using the dynamic model. The simulation is used to tune the PI gains. The gains have to be re-tuned for actual engine implementation. The ILC's converged responses outperformed the PI results.

Chapter 5

Control Robustness

This Chapter tests the robustness of the iterative learning controllers designed in the previous chapter to changes in intake temperature and compression ratio. Then biofuels are added to the primary reference fuels and the robustness of the iterative learning controllers to these changes are compared to a traditional feedback controller.

5.1 Operating Parameters

The ILC is now tested on changes in operating conditions to check how robust it is. To have a robust controller is ideal for engine operation as they are subject to varying conditions Hrovat and Sun [1997]. The changes in operating conditions affect the Markov parameters of the system. This will affect how quickly the system converges or if it converges at all. If the noise variance is affected by the operating conditions then the final iteration error will be affected. This can be seen in eqn. 4.91 where an increase in λ will increase the maximum bound of $E(||\mathbf{e}_\infty||)$. From this equation, the system plant, P can also affect the maximum bound for $E(||\mathbf{e}_\infty||)$ if $||PL||$ or $||I - PL||$ is larger as a result of the operating change.

The operating conditions that are varied are intake temperature, T_{int}, and compression ratio, CR. The ILC is designed at a base point with $T_{int} = 100$ °C and CR=11 as in Table 3.7. The operating conditions are then varied around this point,

with testing done at $T_{int} = 50$ °C, $T_{int} = 150$ °C, CR=10, and CR=12. For each operating change steady-state and a PRBS test is performed, similar to Section 4.1, so that the system changes can be observed. Complete results are given in Appendix C, with only selected results in this chapter.

5.1.1 ILC Intake Temperature Variation

The first operating condition investigated is the intake temperature variation. Intake temperature has been known to strongly effect HCCI combustion timing Shahbakhti [2009] and has even been investigated to be used as an input for an HCCI control strategy Martinez-Frias et al. [2000]. Combustion is affected by intake temperature because the combustion reactions are sensitive to temperature Warnatz et al. [2006].

Setting $T_{int} = 50$ °C, the Markov parameters of the engine from the PRBS testing are shown in Fig. 5.1. Comparing this to Fig. 4.9 the only noticeable difference is the decrease in response between CA50 and E_{iso}. This implies that the effect λ has on combustion timing is enhanced as T_{int} is decreased or the effect that ON has on combustion timing is reduced. The IMEP's responses to the inputs is not affected since the thermal efficiency of the cycle has not been greatly affected therefore the energy inputs should have the same correlations with the energy output.

The results of the three best ILC cases from Chapter 4 are now applied to the the CFR engine with an intake temperature of 50 °C and are shown in Fig. 5.2 with the base cases also shown. One characteristic of the ILC's control under these conditions is the variation of the converged error norm. The standard deviation of $||e_{\text{CA50}}||$, given in Table 5.1, is over 3 times larger than the standard deviation observed at $T_{int} = 100$ °C as given in Table 4.12. This maybe due to an anomaly with the engine knocking every few thousand cycles that is observed when the engine has not warmed up and could be attributed to the fuel not completely evaporating therefore having inconsistent combustion. By lower the intake temperature, the fuel has a lower vapor

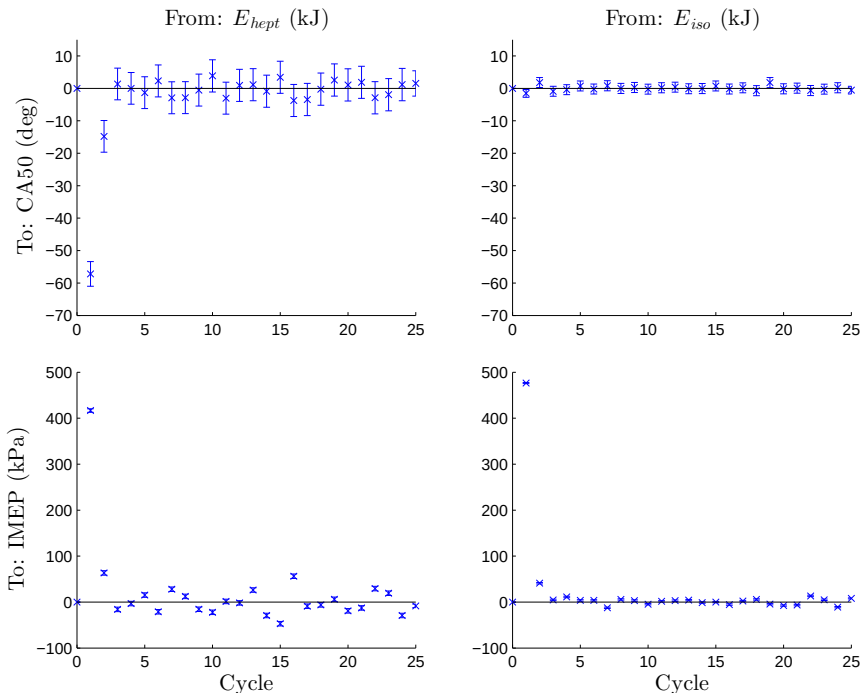

Figure 5.1: $T_{int} = 50$ °C Markov parameters for operating point 1 given in Table 3.8 with 95% confidence intervals found from linear regression of PRBS data.

pressure therefore less fuel would evaporate and increase combustion inconsistencies (which is consistent with what is observed). The steady-state standard deviations of the noise for CA50 and IMEP are 0.66 deg and 4.7 kPa respectively at $T_{int} = 50$ °C compared to 0.47 deg and 3.9 kPa at $T_{int} = 100$ °C which is consistent with the increased deviation of error norm. The IMEP is also affected by the combustion inconsistency. This inconsistency increases the mean of error norms when compared to the base point which is consistent with eqn. 4.91.

Table 5.1: Experimental ILC performance results for CA50 error norm convergence with $T_{int} = 50$°C.

ILC	mean($\|\|e_{\text{CA50}}\|\|$)	std($\|\|e_{\text{CA50}}\|\|$)	$j_{conv,\,\text{CA50}}$
$r = 1000$	8.27	3.44	2
model-less zero-phase Butterworth	7.18	1.43	2
norm-optimal zero-phase Butterworth	6.72	1.33	3

When the intake temperature is increased to 150 °C, the Markov parameters

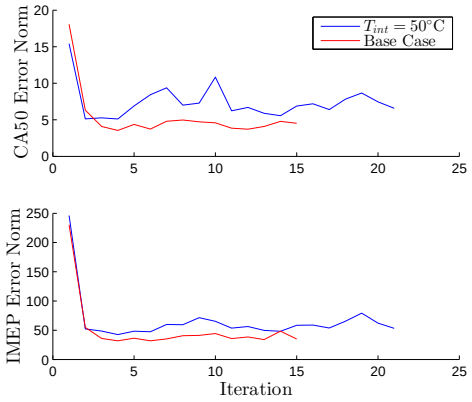

(a) $K = 1.12$ with zero-phase Butterworth filter

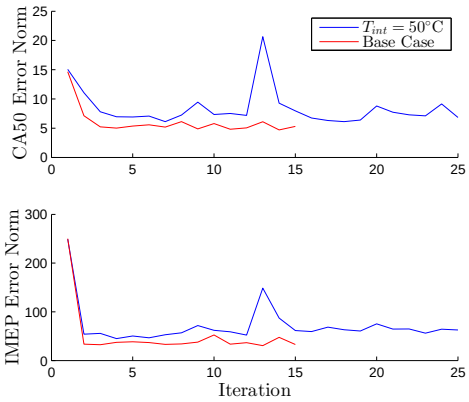

(b) $r = 1000$

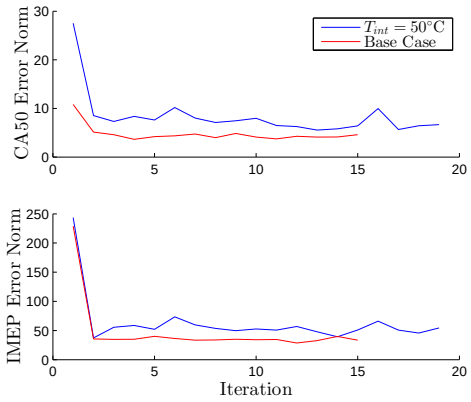

(c) $r = 1$ with zero-phase Butterworth filter

Figure 5.2: ILC iteration error norm at $T_{int} = 50$ °C compared to base case operating point ($T_{int} = 100$ °C).

Table 5.2: Experimental ILC performance results for IMEP error norm convergence with $T_{int} = 50°\text{C}$.

ILC	mean($\|\|e_{\text{IMEP}}\|\|$)	std($\|\|e_{\text{IMEP}}\|\|$)	$j_{conv,\,\text{IMEP}}$
$r = 1000$	69.4	22.6	2
model-less zero-phase Butterworth	58.7	8.50	2
norm-optimal zero-phase Butterworth	51.5	7.06	2

corresponding E_{iso} to CA50 increase as seen in Fig. 5.3. This is consistent with what is observed with the decrease in intake temperature. When the temperature is increased, E_{iso} has a stronger effect on delaying ignition timing. IMEP was not affected by the increase in intake temperature which is consistent with the explanation that efficiency has not been changed by changing the intake temperature. Inspecting the ILC results in Fig. 5.4, IMEP seems to be similar to the base point but CA50 takes longer to converge especially for the model-less with zero phase filter. The converged mean error norm and standard deviation are similar to the base point with the exception of CA50 norm-optimal without a filter which had a larger standard deviation but this is considered insignificant and is attributed to a statistical fluctuation. When looking at the standard deviation of the steady-state operating conditions, which are 0.45 deg and 3.4 kPa for CA50 and IMEP respectively, they are similar to the base point steady-state noise standard deviations.

Table 5.3: Experimental ILC performance results for CA50 error norm convergence with $T_{int} = 150°\text{C}$.

ILC	mean($\|\|e_{\text{CA50}}\|\|$)	std($\|\|e_{\text{CA50}}\|\|$)	$j_{conv,\,\text{CA50}}$
$r = 1000$	5.22	1.03	3
model-less zero-phase Butterworth	4.43	0.811	7
norm-optimal zero-phase Butterworth	4.99	0.501	2

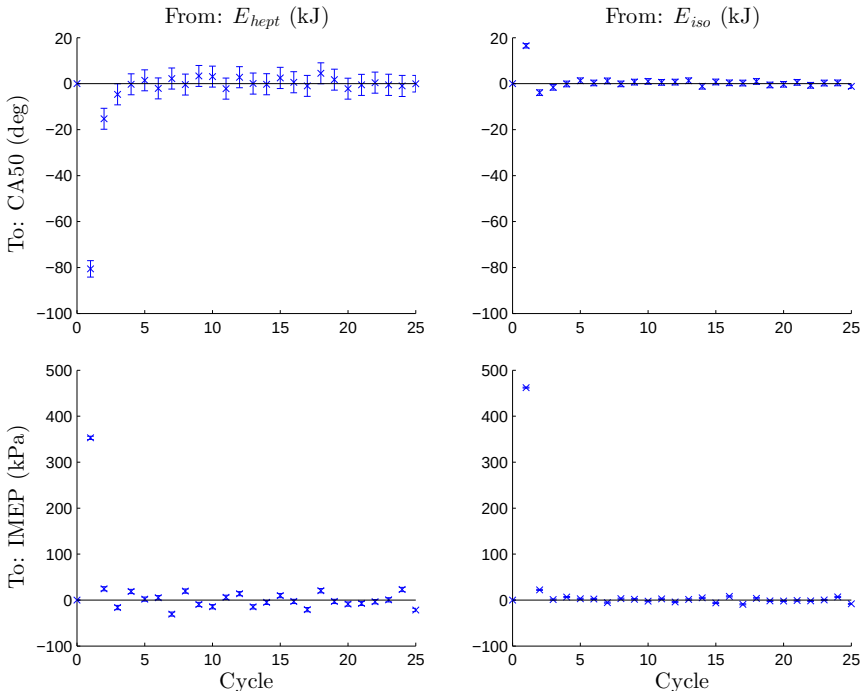

Figure 5.3: $T_{int} = 150$ °C Markov parameters for operating point 2 given in Table 3.8 with 95% confidence intervals found from linear regression of PRBS data.

Table 5.4: Experimental ILC performance results for IMEP error norm convergence with $T_{int} = 150$°C.

ILC	mean($\|\|e_{\text{IMEP}}\|\|$)	std($\|\|e_{\text{IMEP}}\|\|$)	$j_{conv,\,\text{IMEP}}$
$r = 1000$	37.1	4.14	2
model-less zero-phase Butterworth	36.7	4.25	3
norm-optimal zero-phase Butterworth	33.4	3.06	3

5.1.2 ILC Compression Ratio Variation

A CFR engine is designed so the compression ratio can easily be changed. By testing different compression ratios, the performance of the ILC can be investigated since compression ratio is usually fixed on an engine. The compression ratio, CR, is reduced from the base case of 11:1 to 10:1. From the ideal gas law and assuming an isentropic process, the following relationships can be found:

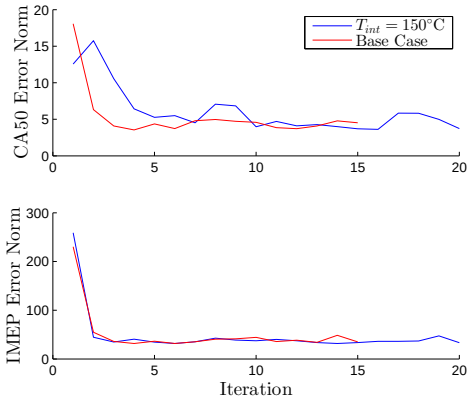

(a) $K = 1.12$ with zero-phase Butterworth filter

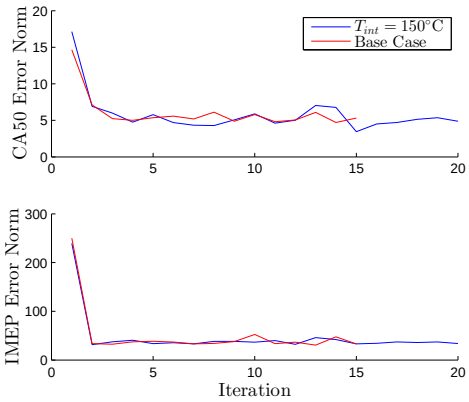

(b) $r = 1000$

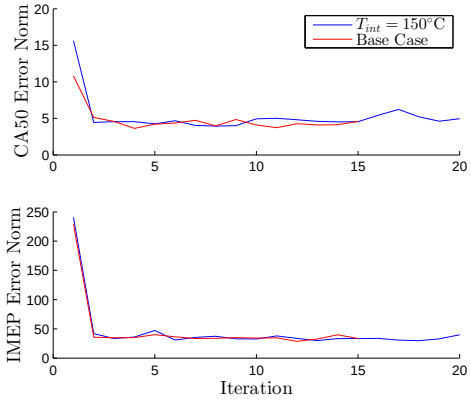

(c) $r = 1$ with zero-phase Butterworth filter

Figure 5.4: ILC iteration error norm at $T_{int} = 150$ °C compared to base case operating point ($T_{int} = 100$ °C).

$$\frac{p_2}{p_1} = (\mathrm{CR})^{\gamma}\,,\ \frac{T_2}{T_1} = (\mathrm{CR})^{\gamma-1} \tag{5.1}$$

where γ is the ratio of specific heats, p and T are the in-cylinder pressure and temperature, and subscript 1 indicates start of compression, BDC, and subscript 2 is any other point in the process. This indicates that decreasing CR decreases both pressure and temperature of the in-cylinder charge, thereby slowing the HCCI reaction. This not equivalent to a decrease only in intake temperature as many reaction rates are affected by the constituents partial pressures Warnatz et al. [2006].

The Markov parameters for the CR=10 system are shown if Fig. 5.5. From this the sensitivity between E_{iso} and CA50 is relatively unchanged, which is not the case when intake temperature was decreased. Another point to notice from this figure is the decrease in both IMEP plots. The thermal efficiency, η, of the Otto cycle Heywood [1988] is:

$$\eta = 1 - \left(\frac{1}{\mathrm{CR}^{(\gamma-1)}}\right) \tag{5.2}$$

The thermal efficiency decreases when CR is decreased, which thereby decreases the IMEP for a given amount of energy input into the system. This explains the decrease in IMEP sensitivity between E_{hept} and E_{iso} compared to the base case in Fig. 4.25.

The results of applying the ILC to the engine with CR=10 are shown in Fig. 5.6. The system takes longer to converge, as expected with changing the plant. The mean and standard deviations, listed in Tables 5.5 and 5.6, for the converged error norm are lower than compared to the base point for both CA50 and IMEP. By looking at

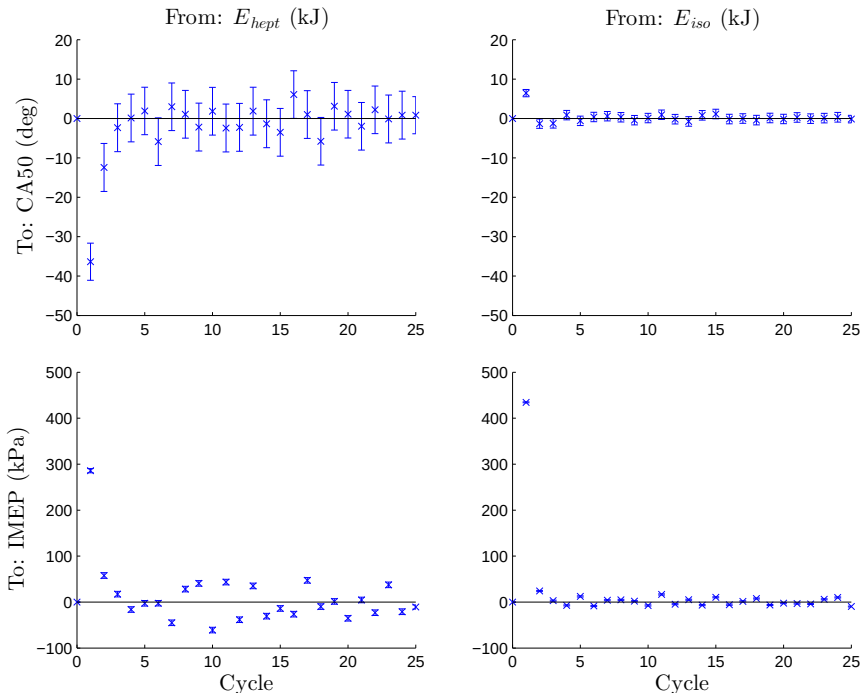

Figure 5.5: CR=10 Markov parameters for operating point 3 given in Table 3.8 with 95% confidence intervals found from linear regression of PRBS data.

the standard deviation of the steady-state operation, 0.37 deg and 3.0 kPa for CA50 and IMEP respectively, the noise is less than the base point values which is consistent with the results seen in the error norm standard deviations.

Table 5.5: Experimental ILC performance results for CA50 error norm convergence with CR=10.

ILC	mean($\|\|e_{\text{CA50}}\|\|$)	std($\|\|e_{\text{CA50}}\|\|$)	$j_{conv,\,\text{CA50}}$
$r = 1000$	3.98	0.925	3
model-less zero-phase Butterworth	3.86	0.579	6
norm-optimal zero-phase Butterworth	3.82	0.579	3

The compression ratio is then increased to 12. The Markov parameters are shown in Fig. 5.7. From the changes between Figs. 4.9 and 5.5, the CA50 sensitivities are expected to remain unchanged and the IMEP sensitives are expected to increase however both CA50 and IMEP Markov parameters are similar to the ones found for the base point. This maybe from the idealized thermal efficiency increasing more from

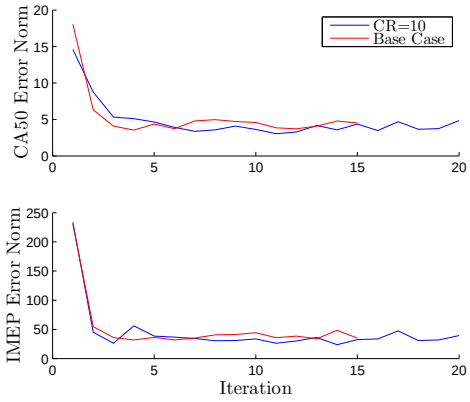

(a) $K = 1.12$ with zero-phase Butterworth filter

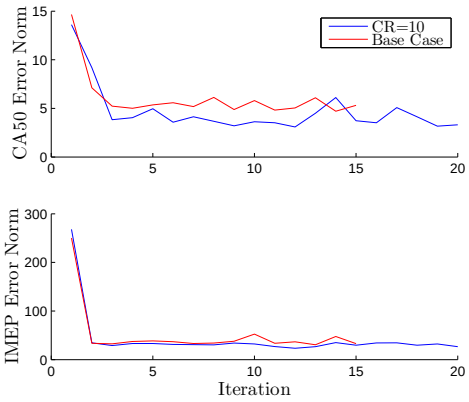

(b) $r = 1000$

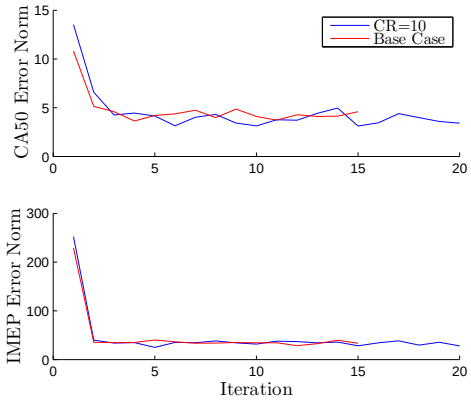

(c) $r = 1$ with zero-phase Butterworth filter

Figure 5.6: ILC iteration error norm at CR=10 compared to base case operating point (CR=11).

Table 5.6: Experimental ILC performance results for IMEP error norm convergence with CR=10.

ILC	mean($\|\|e_{\text{IMEP}}\|\|$)	std($\|\|e_{\text{IMEP}}\|\|$)	$j_{conv,\,\text{IMEP}}$
$r = 1000$	30.1	3.9	3
model-less zero-phase Butterworth	33.3	6.35	3
norm-optimal zero-phase Butterworth	33.7	3.76	3

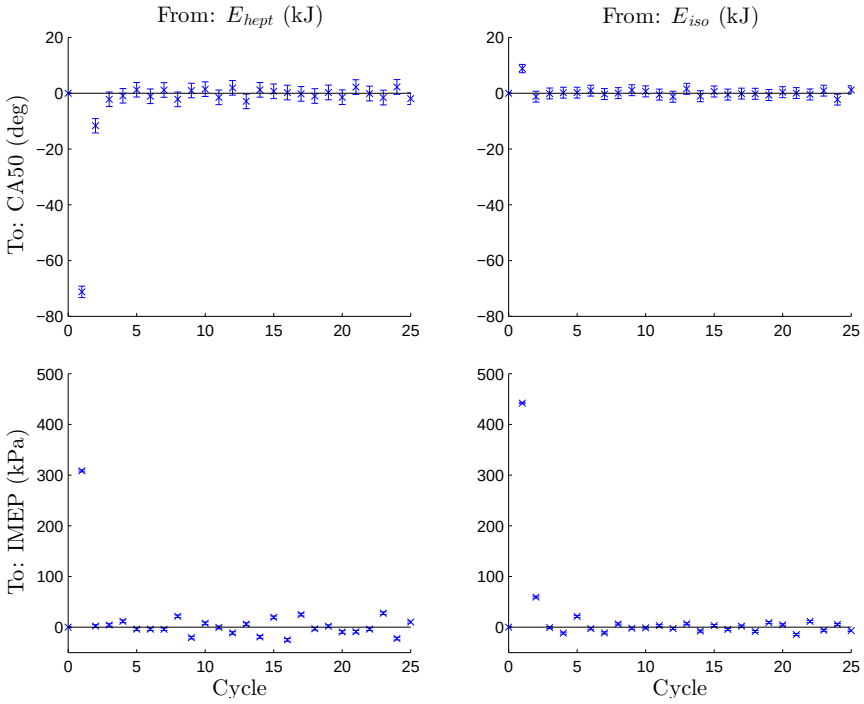

Figure 5.7: CR=12 Markov parameters for operating point 4 given in Table 3.8 with 95% confidence intervals found from linear regression of PRBS data.

CR=10 to CR=11 than from CR=11 to CR=12 due to the non-linearity of eqn. 5.2.

Since the plant, P, at CR=12 is similar to the base point plant CR=11 given in Fig. 4.9, the system is expected to behave similarly for convergence. Fig. 5.8 shows the results of the ILC system. Tables 5.7 and 5.8 are the converged properties. All properties of the converged system are similar to the base point. Looking at the steady-state noise standard deviations, which are 0.44 deg and 3.6 kPa for CA50 and IMEP respectively, the noise level are similar to the base point given in Section 4.1. The convergence is slower compared to the base point but this is attributed to the

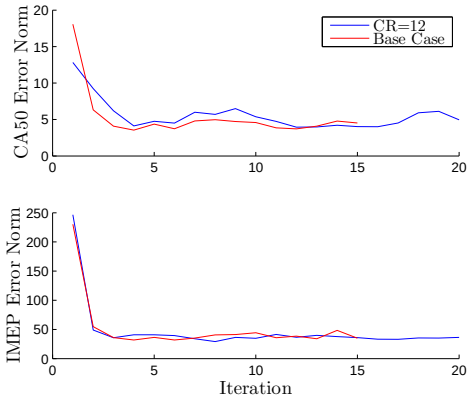

(a) $K = 1.12$ with zero-phase Butterworth filter

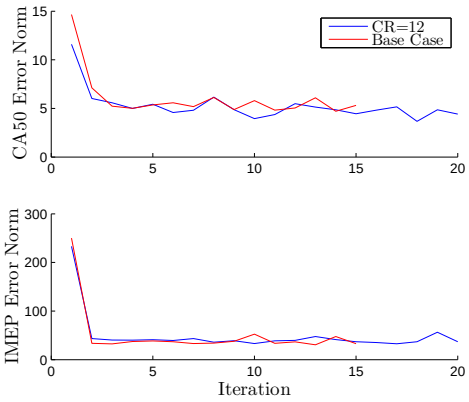

(b) $r = 1000$

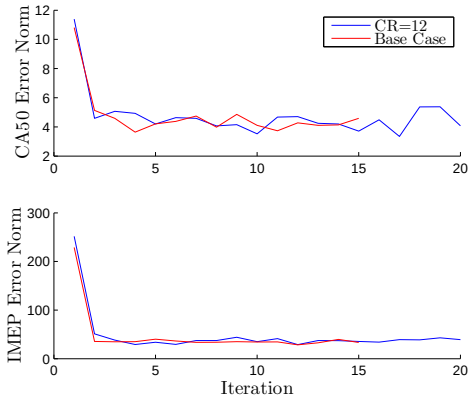

(c) $r = 1$ with zero-phase Butterworth filter

Figure 5.8: ILC iteration error norm at CR=12 compared to base case operating point (CR=11).

small differences in the system plant.

For operating condition variation of intake temperature and compression ratio, the ILC converges and reaches a trajectory that has a small error norm- mostly a function of the system noise. The change in plant, P, mostly affects the time to convergence, which has not increased by more than 4 iterations for all cases listed in Tables 5.1 to 5.8.

Table 5.7: Experimental ILC performance results for CA50 error norm convergence with CR=12.

ILC	mean($\|\|e_{\text{CA50}}\|\|$)	std($\|\|e_{\text{CA50}}\|\|$)	$j_{conv,\,\text{CA50}}$
$r = 1000$	4.65	0.542	4
model-less zero-phase Butterworth	4.71	0.794	4
norm-optimal zero-phase Butterworth	4.34	0.675	2

Table 5.8: Experimental ILC performance results for IMEP error norm convergence with CR=12.

ILC	mean($\|\|e_{\text{IMEP}}\|\|$)	std($\|\|e_{\text{IMEP}}\|\|$)	$j_{conv,\,\text{IMEP}}$
$r = 1000$	39.6	6.97	2
model-less zero-phase Butterworth	36.3	2.54	3
norm-optimal zero-phase Butterworth	37.3	3.79	3

5.2 Biofuels

To simulate HCCI combustion timing and combustion, detailed chemical kinetic structure must be found Warnatz et al. [2006]. This is needed for each fuel and can be difficult and time consuming to obtain. An alternative is to implement control, such as ILC, that treats the change in fuel as a disturbance so that the engine can run on different fuels without loss in performance. This allows new fuels, like biofuels created in a carbon neutral manner, to be run on an HCCI engine.

5.2.1 ILC Ethanol/Iso-Octane Blend Variation

The first biofuel to be tested is ethanol. From Kalghatgi and Head [2004] the CA50 can be predicted from the RON and MON of the fuel, for select fuels. Ethanol has a RON of 107 and MON of 89 Stradling et al. [2009] which has a delayed combustion timing compared to iso-octane Kalghatgi and Head [2004] assuming the operating condition is closer to or beyond the RON operating conditions. A 10% ethanol/90% iso-octane, by volume, mixture is created and denoted by $E_{eth/iso}$. This mixture is used as one of the inputs into the system, replacing E_{iso}, while E_{hept} remains the

other input. A PRBS is implemented and the Markov parameters are found as shown in Fig. 5.9. One of the most predominate changes is the large increase in the first Markov parameter for $E_{eth/iso}$ to CA50 compared to E_{iso}, as expected from Kalghatgi and Head [2004].

The ILC are then tested using the new fuel, $E_{eth/iso}$, as an input. The error norm results are shown in Fig. 5.10 with the evaluations given in Tables 5.9 and 5.10. For each of the ILC control structures, the CA50 error norm increases from the first to the second iteration. Since the noise steady-state standard deviation for this system are 0.46 deg and 3.1 kPa for CA50 and IMEP respectively, compared to the base point of 0.47 deg and 3.9 kPa for CA50 and IMEP respectively, this error norm increase is not thought to be a product of the noise; instead the system changes from monotonic convergence to only asymptotically convergent when the input fuel is changed. From Tables 5.9 and 5.10, the ILCs have decreased in performance. The most notable change is the j_{conv} values which has increased significantly from the base point. This is not unexpected as discussed above, changing the plant is expected to change the convergence performance. The mean and standard deviation of the error norms for both CA50 and IMEP increased from the base point except for the standard deviations of IMEP error norm which decreased for the norm-optimal control without a filter . The increase in mean error norm is explained through eqn. 4.91 where the drastic change in P has increased both $||PL||$ and $||I - PL||$. The final iteration control responses for the norm optimal with zero-phase Butterworth filtering are shown in Fig. 5.11. Comparing this to Fig. 4.24d, a difference in input signals can be noted while the output signals are similar between the two figures. This is a benefit of having an ILC, that even if the plant changes, the input can be relearned without a significant decrease in performance so long as the ILC remains stable.

The PI controller designed in Section 4.5 is then tested on the single cylinder engine. The response is shown in Fig. 5.12. The error norms are 6.29 and 76.7 for

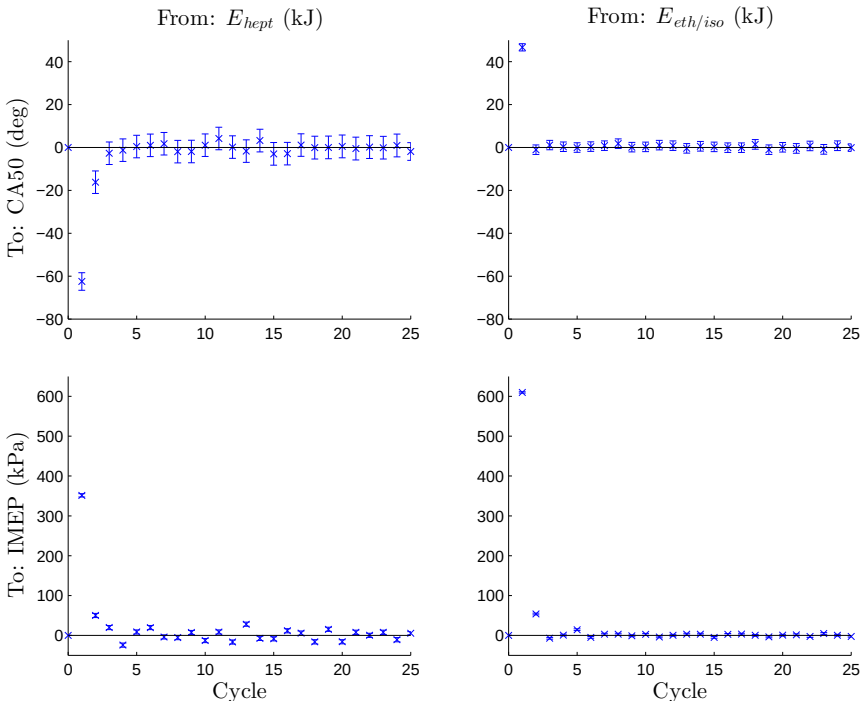

Figure 5.9: Markov parameters for operating conditions with ethanol/iso-octane blend and given in Table 3.7 with 95% confidence intervals found from linear regression of PRBS data.

CA50 and IMEP respectively. This is a 17% and 22.5% increase from the base point PI error norm, for CA50 and IMEP respectively. In contrast norm-optimal control has a 13% and 7% increase in error norm from the base point, for CA50 and IMEP respectively. The PI only has a lower CA50 error norm than the $r = 1000$ case.

Table 5.9: Experimental ethanol/iso-octane blend ILC performance results for CA50 error norm convergence.

ILC	mean($\|\|e_{\text{CA50}}\|\|$)	std($\|\|e_{\text{CA50}}\|\|$)	$j_{conv,\,\text{CA50}}$
$r = 1000$	6.61	1.14	4
model-less zero-phase Butterworth	5.62	1.27	9
norm-optimal zero-phase Butterworth	4.85	0.483	8

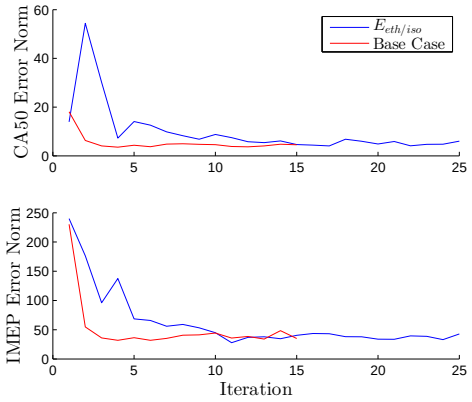

(a) $K = 1.12$ with zero-phase Butterworth filter

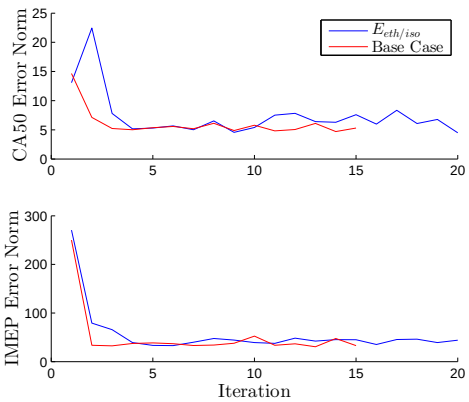

(b) $r = 1000$

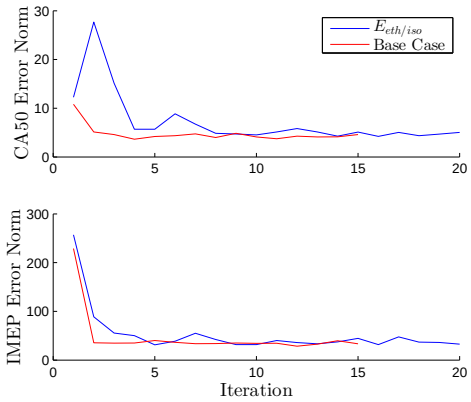

(c) $r = 1$ with zero-phase Butterworth filter

Figure 5.10: ILC iteration error norm with ethanol/iso-octane blend and operating conditions given in Table 3.7.

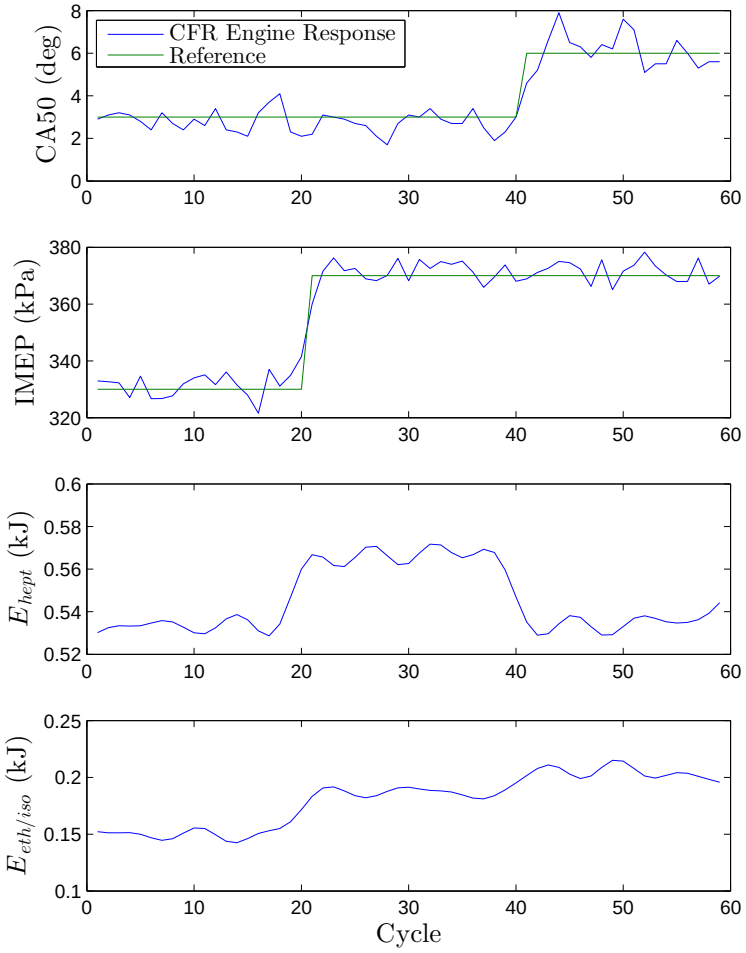

Figure 5.11: Experimental ILC final iteration control responses for $r = 1$ with zero-phase Butterworth filter with ethanol/iso-octane blend.

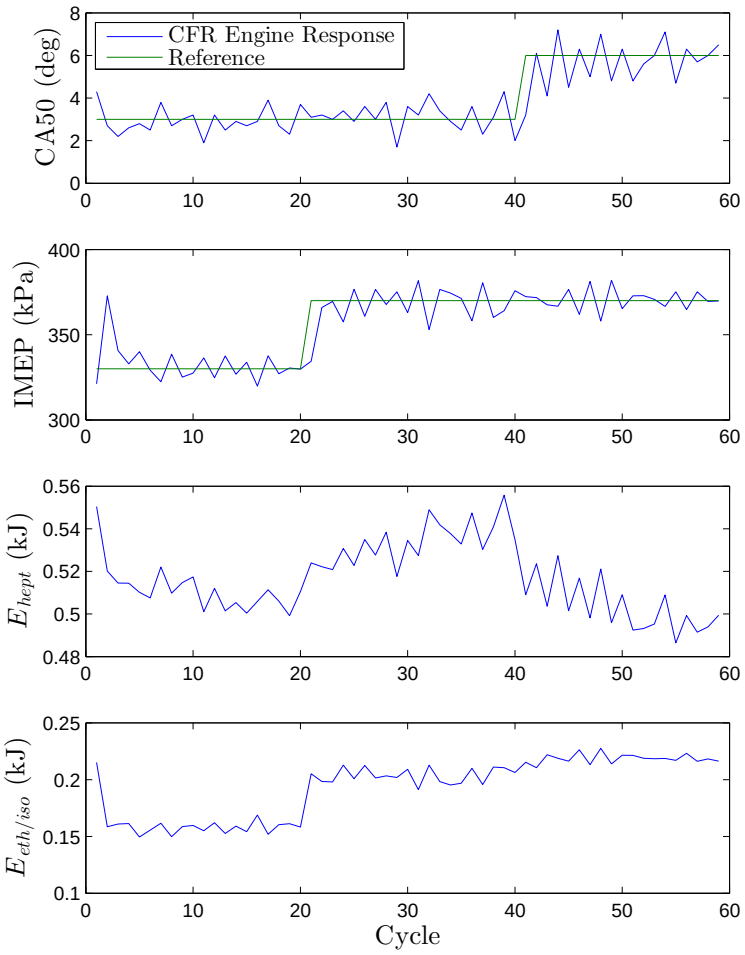

Figure 5.12: Experimental PI control engine response with ethanol/iso-octane blend.

Table 5.10: Experimental ethanol/iso-octane blend ILC performance results for IMEP error norm convergence.

ILC	mean($\|\|e_{\text{IMEP}}\|\|$)	std($\|\|e_{\text{IMEP}}\|\|$)	$j_{conv,\,\text{IMEP}}$
$r = 1000$	42.6	4.15	4
model-less zero-phase Butterworth	37.9	4.57	11
norm-optimal zero-phase Butterworth	37.1	5.13	5

5.2.2 ILC Biodiesel/n-Heptane Blend Variation

A biodiesel fuel is now tested. As in Section 5.2.1, the biodiesel is mixed with the PFR n-heptane with 10% biodiesel and 90% n-heptane blend, denoted $E_{bio/hept}$. The biodiesel is the Milligan Biofuels Inc. Diesel Fuel Conditioner which is a canola oil derivative. From the technical data sheet, the cetane number of this fuel is 60.7. Cetane number is similar to octane number but is used to determine fuel quality for diesel engines therefore higher cetane number fuels are more reactive and have shorter combustion delays Lichty [1951]. This correlates with Szybist and Bunting [2005] that found lower cetane number required a higher intake temperature for HCCI operation. From these, the expectation is that the addition of the biofuel should raise the sensitivity of CA50 to $E_{bio/hept}$ compared to E_{hept}. A PRBS is implemented on the single cylinder engine with the Markov parameters from the test shown in Fig. 5.13. Comparing this to Fig. 4.9, CA50 has a higher sensitivity to E_{hept}. This maybe from the n-heptane having a similar cetane number, 56, to the biodiesel, the relatively low concentration of biodiesel, the reduced evaporation rate of the diesel or some combustion property of the biodiesel that cannot be identified without the chemical kinetics.

The ILCs are then used with the new fuel mixture. The error norms are shown in Fig. 5.14 and the convergence performance evaluations are given in Tables 5.11 and 5.12. With the Markov parameters in Fig. 5.13 being similar to the base point Markov parameters shown in Fig. 4.9, and the steady-state noise standard deviations

being 0.46 deg and 3.55 kPa for CA50 and IMEP respectively, which are similar to the base point values, the performance should be similar. This is found to be the case. The mean error norms and IMEP error norms standard deviations are very similar to the base point values. The standard deviations are slightly larger for CA50 compared to the base point. The convergence times are also similar to the base point. This indicates that the addition biodiesel has little effect on the system plant. This is confirmed by comparing the control signals for $r = 1$ with zero-phase Butterworth filter and $E_{bio/hept}$ as an input shown in Fig. 5.15 to the control signals for $r = 1$ with zero-phase Butterworth filter and E_{hept} as an input shown in Fig. 4.24d. The converged inputs are similar between the two, which is in contrast to when ethanol was added to the system.

The PI controller developed in Section 4.5 was also implemented with the new fuel. The responses for the PI control are shown in Fig. 5.16. The error norms for this system are 6.73 and 67.4 for CA50 and IMEP respectively. These are much higher than any of the ILC results in Tables 5.11 and 5.12. This may be due to the large error caused by the initial conditions of the system, which highlights another benefit of ILC in that initial conditions are easily corrected for and do not affect the converged response as greatly as a feedback controller.

Table 5.11: Experimental biodiesel/n-heptane blend ILC performance results for CA50 error norm convergence.

ILC	mean($\|\|e_{\text{CA50}}\|\|$)	std($\|\|e_{\text{CA50}}\|\|$)	$j_{conv,\,\text{CA50}}$
$r = 1000$	4.26	0.763	4
model-less zero-phase Butterworth	4.17	0.58	2
norm-optimal zero-phase Butterworth	4.26	1.12	3

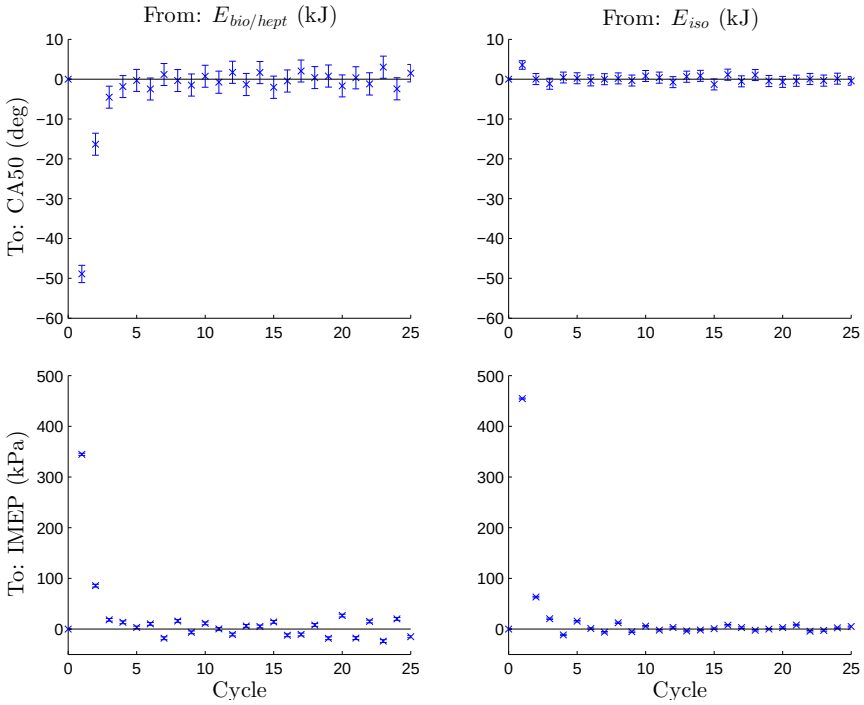

Figure 5.13: Markov parameters for operating conditions with biodiesel/n-heptane blend and given in Table 3.7 with 95% confidence intervals found from linear regression of PRBS data.

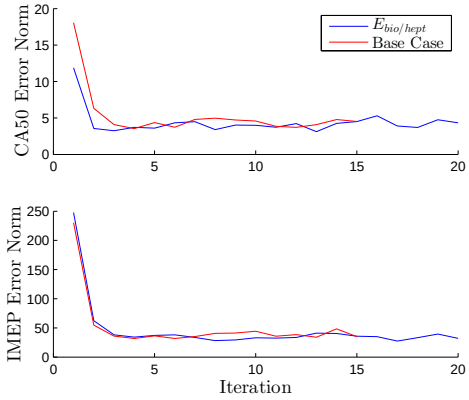

(a) $K = 1.12$ with zero-phase Butterworth filter

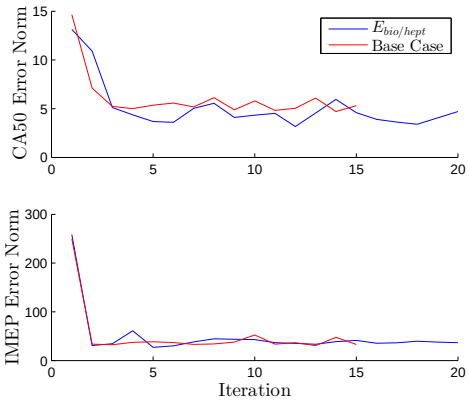

(b) $r = 1000$

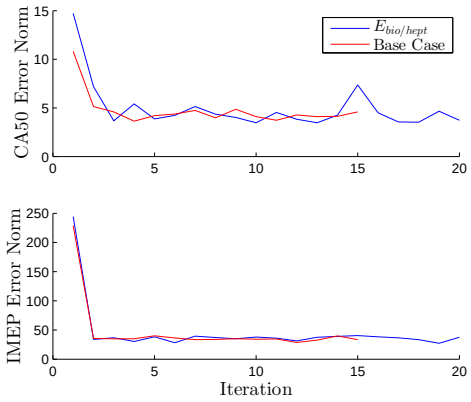

(c) $r = 1$ with zero-phase Butterworth filter

Figure 5.14: ILC iteration error norm with biodiesel/n-heptane blend and operating conditions given in Table 3.7.

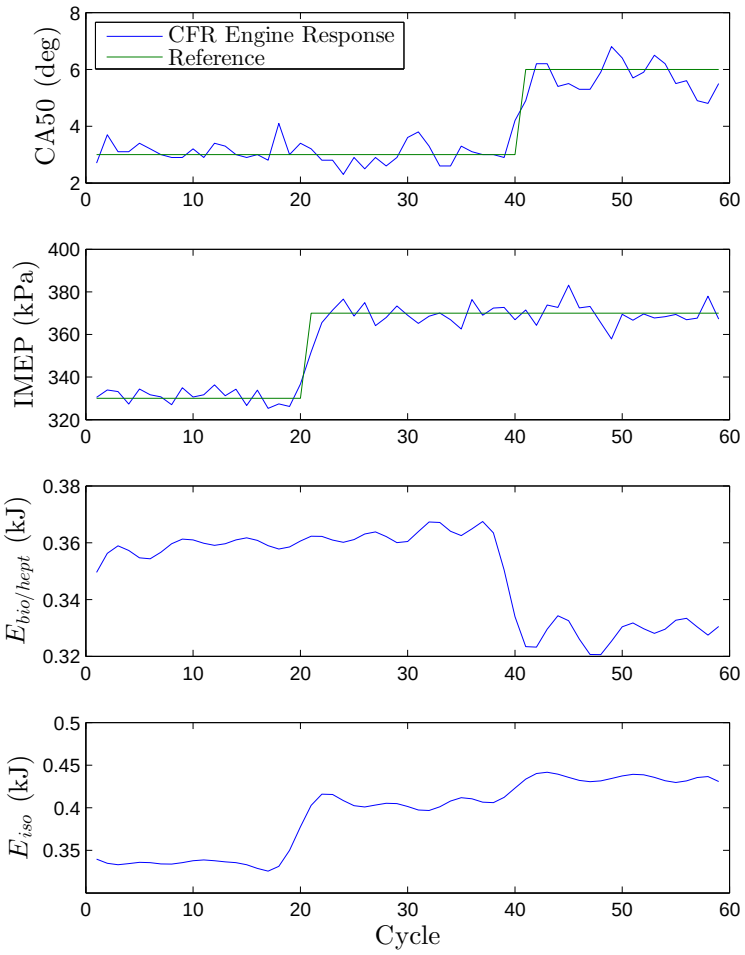

Figure 5.15: Experimental final iteration ILC control responses for $r = 1$ with zero-phase Butterworth filter with biodiesel/n-heptane blend.

Table 5.12: Experimental biodiesel/n-heptane blend ILC performance results for IMEP error norm convergence.

ILC	mean($\|\|e_{\text{IMEP}}\|\|$)	std($\|\|e_{\text{IMEP}}\|\|$)	$j_{conv,\,\text{IMEP}}$
$r = 1000$	37.7	2.81	2
model-less zero-phase Butterworth	34.9	4.12	3
norm-optimal zero-phase Butterworth	35.9	3.83	2

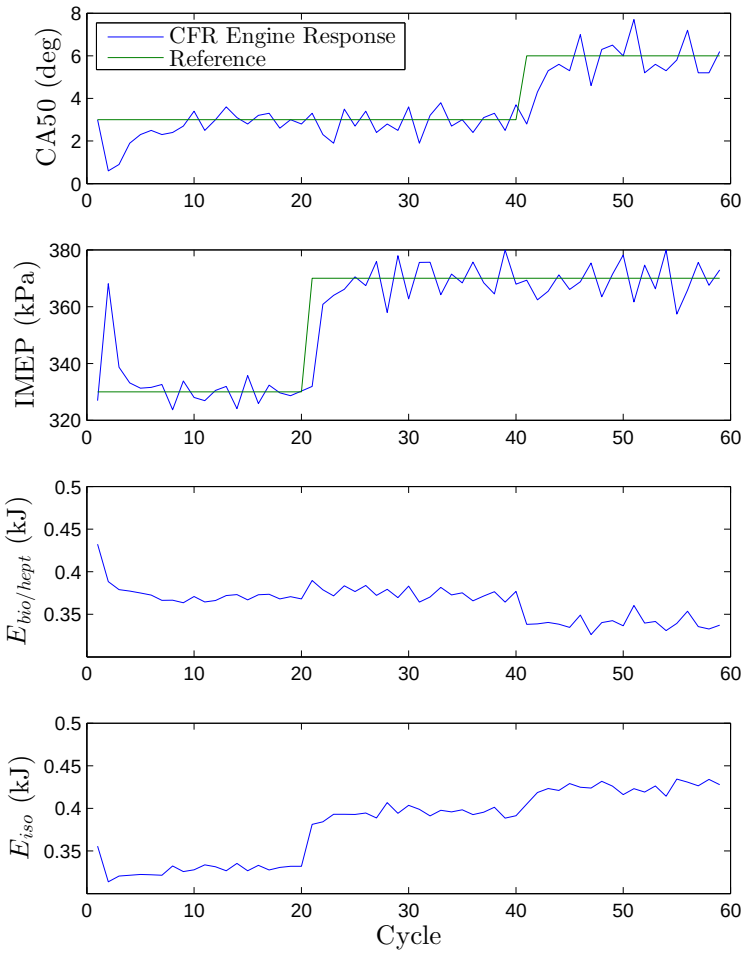

Figure 5.16: Experimental PI control engine response with biodiesel/n-heptane blend.

5.3 Summary

Three ILC control strategies are tested for robustness to changes in engine operation. The ILC's are developed at a base point engine operating point described in Chapter 4 and are not modified for the changing conditions. First the intake temperature and compression ratio are varied and a system identification is performed to find the Markov parameters to find how the different operating conditions affect the system response. It is found that intake temperature affects the CA50 response while compression ratio affects IMEP. The ILCs are then implemented on the engine with each operating change. All ILCs are able to converge and converged performance is mostly affected by any changes in noise variance from operating conditions. The convergence times are longer for different operating conditions but this was expected as the learning filter is not optimized for the new operating conditions.

Then the input fuels are changed. Ethanol is added to the iso-octane input fuel then biodiesel is added to the n-heptane fuel. A system identification for each fuel is done to find the Markov parameters for each biofuel addition. The ethanol is found to change the CA50 response while the biodiesel had relatively no effect. The ILCs are then tested with each new fuel addition. They all converged and have similar converged performance to the base point. The convergence times are longer with the addition of ethanol while the addition of biodiesel has little affect on the convergence time. This is explained by the large change in system plant observed by the addition of ethanol compared to the base point while the addition of biodiesel has little change in system plant. The PI controller designed in Chapter 4 is also implemented with the biofuel additions. It is found that the systems were stable but the ILCs still outperformed the PI controllers.

ILC has been found to be robust to variations on intake temperature, compression ratio and the addition of biofuel. ILC is able to control CA50 and IMEP during

repetitive operation of an HCCI and the converged iteration trajectory outperforms a PI controller.

Chapter 6

Conclusions

Conclusions and future work are described in this chapter.

6.1 Conclusions

The goal of this study is to design an ILC that can control the combustion timing and load of a single cylinder engine using a dual-fuel system operating in HCCI. A system identification is done to find the dynamics of the system and a model that can be used to design the ILC and simulate the ILC response. The model found from the system identification is used to design an ILC norm-optimal control scheme. The ILC norm-optimal is simulated using the model to find the optimal weightings of the ILC norm-optimal and is then implemented on the engine. The ILC norm-optimal performs well but the noise of the system is found to affect the final results. The simulation also agreed well with experimental results. Next an ILC model-less control strategy is designed for MIMO ILC, that only requires the selection of a single gain for controller performance. This method involves using the steady-state sensitivities of the system. The stability of the system as a function of the gain is investigated. The ILC model-less control is tested on the model and the engine, and once again the model and the experimental results match well.

With both ILC designs (norm-optimal ILC and model-less ILC), the noise affected

the end results. To account for this two filters for noise attenuation are investigated. Since ILC considers one iteration of the repetitive process at a time the use of non-causal filters is possible. Since the model simulation matches the experimental results, the simulated model is used to find the optimal filter parameters for both filters. A Gaussian and zero-phase Butterworth filter are used to attenuate noise. Once the filter parameters are chosen, they are tested with both model-less and a norm-optimal ILC on the engine. The three best ILC designs are found to be: the model-less with zero-phase filtering; low weighting ILC norm-optimal with zero-phase filtering; and a medium weighting ILC norm-optimal without filtering.

A PI controller is also designed and tuned for the system. The ILC, compared to the PI control, is found to have better final iteration reference trajectory tracking.

The three chosen ILC designs are then tested by varying the operating conditions from the base case. The control is developed for the base case then tested for varying operating conditions to test the robustness of control. Four operating points are chosen with respect to the base point that the ILC is designed and initially tested on: increase intake temperature, decrease intake temperature, increase compression ratio and decrease compression ratio. Each ILC is found to converge for each operating condition. The final iteration error is found to be function of changes in noise variance from the change in operating condition.

Then the three chosen ILC designs are also tested with changes in fuel (input variation). Two different tests are performed, one with and ethanol mixture and the other with a biofuel mixture. All three ILC designs converged, with biofuel performing similar to the base point. The PI controller designed on the base point is also tested with the new fuel tests. The PI controller is stable for both fuels but the ILC final iteration are found to provide better reference trajectory tracking.

In summary, this study found that ILC outperforms PI control and is robust to changes in intake temperature, compression ratio and the addition of biofuels with

little changes in the final iteration reference tracking error.

6.2 Future Work

- A Kalman filter has been designed for ILC by Ahn et al. [2007a] and could have large improvements for final iteration error without the need for non-causal filters.
- Investigate the use of higher order ILC application for improved learning and decreased noise effects.
- Explore the ILC stability to operating conditions and fuel mixtures.
- Test additional operating condition parameters robustness, such as engine speed, intake pressure and EGR.
- Implement a feedback controller in tandem with an ILC to improve first iteration error and single iteration disturbances as described in Bristow et al. [2006].

References

(2013). Biofuelnet Brochure.

Aceves, S. M., Flowers, D. L., Martinez-frias, J., Smith, J. R., Dibble, R., Au, M., and Girard, J. (2001). HCCI Combustion : Analysis and Experiments. *SAE Paper*, (724):2001–01–2077.

Aceves, S. M., Smith, J. R., Westbrook, C. K., and Pitz, W. J. (1999). Compression Ratio Effect on Methane HCCI Combustion. *Journal of Engineering for Gas Turbines and Power*, 121(3):569.

Ahn, H.-S., Chen, Y., and Moore, K. L. (2007a). *Iterative Learning Control*. Communications and Control Engineering. Springer London, London.

Ahn, H.-S., Moore, K. L., and Chen, Y. (2007b). Stability analysis of discrete-time iterative learning control systems with interval uncertainty. *Automatica*, 43(5):892–902.

Albahri, T. a. (2003). Structural Group Contribution Method for Predicting the Octane Number of Pure Hydrocarbon Liquids. *Industrial & Engineering Chemistry Research*, 42(3):657–662.

API (1968). API Technical Data Book on Petroleum Refining. Washington, DC.

Arrègle, J., Tormos, B., López, J. J., and García, A. (2009). Analysis of the Potential

of Biodiesel as an Alternative Fuel for Current and Future HSDI Engines. In *SAE Technical Paper*, pages 2009–01–0480.

ASTM (1968). Standard Test Method for Motor Octane Number of Spark-Ignition Engine Fuel.

Atkins, M. (2004). *Experimental Examination of the Effects of Fuel Octane and Diluent on HCCI Combustion*. Master's, Universty of Alberta.

Audet, A. D. (2008). *Closed Loop Control of HCCI using Camshaft Phasing and Dual Fuels*. Masters, University of Alberta.

Barton, K. L. and Alleyne, A. G. (2011). A norm optimal approach to time-varying ILC with application to a multi-axis robotic testbed. *IEEE Transactions on Control Systems Technology*, 19(1):166–180.

Bidarvatan, M. and Shahbakhti, M. (2013). Two-Input Two-Output Control of Blended Fuel HCCI Engines. Number 2013-01-1663.

Bristow, D., Tharayil, M., and Alleyne, A. (2006). A Survey of Iterative Learning Control. *IEEE Control Systems Magazine*, 26(3):96–114.

Cassell, J. (1854). *The popular educator*. Ludgate Hill, London, 4th volume edition.

Chang, J., Güralp, O., Filipi, Z., Assanis, D., Kuo, T.-w., Najt, P., and Rask, R. (2004). New Heat Transfer Correlation for an HCCI Engine Derived from Measurements of Instantaneous Surface Heat Flux. *SAE Technical Papers*, (724):SAE 2004–01–2996.

Chia-Jui Chiang, Chih-Cheng Chou, and Jian-Hong Lin (2012). Adaptive control of homogeneous charge compression ignition (HCCI) engines. In *2012 American Control Conference (ACC)*, number 21, pages 2066–2071. IEEE.

Dec, J. E., Yang, Y., and Dronniou, N. (2011). Boosted HCCI - Controlling Pressure-Rise Rates for Performance Improvements using Partial Fuel Stratification with Conventional Gasoline. *SAE International Journal of Engines*, 4(1):2011–01–0897.

Dooren, S. V. (2015). *Iterative Learning Control for Internal Combustion Engines*. Master's, Institute for Dynamic Systems and Control Swiss Federal Institute of Technology (ETH) Zurich.

Ebrahimi, K. and Koch, C. R. (2015). Model Predictive Control for Combustion Timing and Load Control in HCCI engines. *SAE*, 2015-01-08.

Eglof, Gusftav And Arsdell, P. M. V. (1941). Octane rating relationships of aliphatic, alicyclic, mononuclear aromatic. *Institute of Petroleum*, 27(210):121–138.

EPA, U. (2012). EPA and NHTSA Set Standards to Reduce Greenhouse Gases and Improve Fuel Economy for Model Years 2017-2025 Cars and Light Trucks. *EPA-420-F-051*.

F. H. Garner, E. B. Evans, C. H. Sprake, E. J. B. (1933). The Blending Octane Numbers of Pure Hydrocarbons and their Dependence upon Concentration. London, UK. World Petroleum Congress.

Fiorentino, A., Giardini, C., and Ceretti, E. (2015). Application of artificial cognitive system to incremental sheet forming machine tools for part precision improvement. *Precision Engineering*, 39:167–172.

Fiveland, S. B., Agama, R., Johansson, B., Christensen, M., Hiltner, J., Mauss, F., and Assanis, D. N. (2001). Experimental and simulated results detailing the sensitivity of natural gas hcci engines to fuel composition. *SAE Technical Papers*, 2001-01-36(August):1–12.

Flowers, D. L., Aceves, S. M., Martinez-Frias, J., and Dibble, R. W. (2002). Prediction of carbon monoxide and hydrocarbon emissions in iso-octane HCCI engine combustion using multizone simulations. *Proceedings of the Combustion Institute*, 29(1):687–694.

Franklin, G., Powell, J. D., and Emami-Naeini, A. (2015). *Feedback Control of Dynamic Systems*. Pearson, 7th edition.

Galkowski, K., Lam, J., Rogers, E., Xu, S., Sulikowski, B., Paszke, W., and Owens, D. (2003). LMI based stability analysis and robust controller design for discrete linear repetitive processes. *International Journal of Robust and Nonlinear Control*, 13(13):1195–1211.

Gauthier, G. and Boulet, B. (2005). Convergence analysis of terminal ILC in the z domain. In *Proceedings of the 2005, American Control Conference, 2005.*, pages 184–189. IEEE.

Golub, G. H. and Van Loan, C. F. (1996). *Matrix Computations*. 3rd edition.

Haddad, R. and Akansu, A. (1991). A class of fast Gaussian binomial filters for speech and image processing. *IEEE Transactions on Signal Processing*, 39(3):723–727.

Handford, D. (2009). *Direct Injection Assisted HCCI Combustion of Natural Gas*. Master of science, University of Alberta.

Heywood, J. (1988). *Internal Combustion Engine Fundamentals*. McGraw-Hill Science/Engineering/Math.

Hinkelbein, J., Sandikcioglu, C., Pischinger, S., Lamping, M., and Körfer, T. (2010). Control of the diesel combustion process via advanced closed loop combustion control and a flexible injection rate shaping tool. *SAE International Journal of Fuels and Lubricants*, 2(2):362–375.

Hosseini, V. (2008). *Reformer Gas Application in HCCI Combustion Engine*. PhD thesis, University of Alberta.

Hrovat, D. and Sun, J. (1997). Models and control methodologies for IC engine idle speed control design. *Control Engineering Practice*, 5(8):1093–1100.

Huang, B., Qi, Y., and Murshed, A. M. (2013). *Dynamic Modelling and Predictive Control in Solid Oxide Fuel Cells: First Principle and Data-Based Approaches*. John Wiley & Sons, Ltd, Chichester, UK.

Iida, M., Hayashi, M., Foster, D. E., and Martin, J. K. (2003). Characteristics of Homogeneous Charge Compression Ignition (HCCI) Engine Operation for Variations in Compression Ratio, Speed, and Intake Temperature While Using n-Butane as a Fuel. *Journal of Engineering for Gas Turbines and Power*, 125(2):472–478.

Jia, Q., Wang, Q., and Ma, P. (2010). Prediction of the enthalpy of vaporization of organic compounds at their normal boiling point with the positional distributive contribution method. *Journal of Chemical and Engineering Data*, 55:5614–5620.

Jian-Xin, X. and Tan, Y. (2003). *Linear and Nonlinear Iterative Learning Control*, volume 291 of *Lecture Notes in Control and Information Sciences*. Springer Berlin Heidelberg, Berlin, Heidelberg.

Kalghatgi, G. (2003). A Method of Defining Ignition Quality of Fuels in HCCI. *SAE International*.

Kalghatgi, G. T. and Head, R. A. (2004). The Available and Required Autoignition Quality of Gasoline - Like Fuels in HCCI Engines at High Temperatures. In *Spring Fuels and Lubricants Conference and Exhibition*, number 2004-01-1969.

Kapania, N. R. and Gerdes, J. C. (2015). Path tracking of highly dynamic autonomous

vehicle trajectories via iterative learning control. In *2015 American Control Conference (ACC)*, pages 2753–2758. IEEE.

Kaplan, W. (1984). *Advanced Calculus*. Addison-Wesley, Reading, MA, 3rd edition.

Kelly-Zion, P. L. and Dec, J. E. (2000). A computational study of the effect of fuel type on ignition time in homogeneous charge compression ignition engines. *Proceedings of the Combustion Institute*, 28(1):1187–1193.

Kirchen, P. (2004). *Thermokinetic Modeling of the HCCI Cycle: Predicting the Ignition Timing*. Master of science, University of Alberta.

Lapuerta, M., Rodríguez-Fernández, J., and Oliva, F. (2010). Determination of enthalpy of formation of methyl and ethyl esters of fatty acids. *Chemistry and Physics of Lipids*, 163:172–181.

Lax, P. D. (2002). *Functional Analysis*. Wiley-Interscience.

Lichty, L. C. (1951). *Internal Combustion Engines*. McGraw-Hill Book Company.

Ljung, L. (1999). System Identification: Theory for the User. In *Wiley Encyclopedia of Electrical and Electronics Engineering*, volume 19, pages 95–96. John Wiley & Sons, Inc., Hoboken, NJ, USA.

Martinez-Frias, J., Aceves, S. M., Flowers, D., Smith, J. R., and Dibble, R. (2000). HCCI Engine Control by Thermal Management. In *SAE International*, volume 2000-01-28.

Mathworks (2015). Matlab "Compare" Function Help.

Meng, D., Jia, Y., Du, J., and Yu, F. (2011). Robust learning controller design for MIMO stochastic discrete-time systems: An H-based approach. *International Journal of Adaptive Control and Signal Processing*, 25(7):653–670.

Mitra, S. K. (2006). *Digital Signal Processing: A Computer-Based Approach*. McGraw-Hill, 3rd edition.

Moffat, R. J. (1988). Describing the uncertainties in experimental results. *Experimental Thermal and Fluid Science*, 1(1):3–17.

Moore, K. L., Chen, Y., and Ahn, H.-S. (2006). Iterative Learning Control: A Tutorial and Big Picture View. In *Proceedings of the 45th IEEE Conference on Decision and Control*, pages 2352–2357. IEEE.

Najt, P. M. and Foster, D. E. (1983). Compression-Ignited Homogeneous Charge Combustion. *SAE Technical Paper 830264*.

Oakley, A., Zhao, H., Ladommatos, N., and Ma, T. (2001). Experimental Studies on Controlled Auto-ignition (CAI) Combustion of Gasoline in a 4-Stroke Engine. *Sae*, (2001-01-1030).

Parzer, H., Gattringer, H., Müller, A., and Naderer, R. (2015). Learning Robot Force/Position Control for Repetitive High Speed Applications with Unknown Non-Linear Contact Stiffness. *Pamm*, 15(1):65–66.

Poling, B. E. and Prausnitz, J. M. (2001). *THE PROPERTIES OF GASES AND LIQUIDS*. McGraw-Hill, 5th edition.

Powell, P. D. (2011). Calculating Determinants of Block Matrices.

Rapp, V. H., Cannella, W. J., Chen, J.-Y., and Dibble, R. W. (2013). Predicting Fuel Performance for Future HCCI Engines. *Combustion Science and Technology*, 185(April 2015):735–748.

Risberg, P., Kalghatgi, G., and Ångstrom, H.-e. (2003). Auto-ignition Quality of Gasoline-Like Fuels in HCCI Engines. *SAE Technical Paper*, 2003(724).

Schneider, D. (2010). Biofoolish. *IEEE Spectrum*, 47(1):48–50.

Shahbakhti, M. (2009). *Modeling and Experimental Study of an HCCI Engine for Combustion Timing Control*. Doctor of philosophy, University of Alberta.

Shibata, G. (2007). Auto-Ignition Characteristics of Hydrocarbons and Development of HCCI Fuel Index. 2007(724):776–790.

Shibata, G., Oyama, K., Urushihara, T., and Nakano, T. (2005). Correlation of Low Temperature Heat Release With Fuel Composition and HCCI Engine Combustion. *SAE Technical Paper*, 2005(724).

Slavinskaya, N. A. and Haidn, O. J. (2003). Modeling of n-Heptane and Iso-Octane Oxidation in Air. *Journal of Propulsion and Power*, 19(6):1200–1216.

Smith, M. L. and Stinson, K. W. (1952). *Fuels and Combustion*. McGraw-Hill Book Company.

Soderstrom, T. S. and Stoica, P. G. (1989). *System Identification*. Prentice Hall.

Son, T., Pipeleers, G., and Swevers, J. (2015). Robust Monotonic Convergent Iterative Learning Control. *IEEE Transactions on Automatic Control*, 32:1–1.

Stanglmaier, R. H. and Roberts, C. E. (1999). Homogeneous Charge Compression Ignition (HCCI): Benefits, Compromises, and Future Engine Applications. *SAE International*, (1999-01-3682).

Stradling, R., Antunez Martel, F.-J., Ariztegui, J., Beeckmann, J., Bjordal, S., Blosser, P., Canovas, J., Clark, A., Elliott, N., Farenback-Brateman, J., Gomez-Acebo, P., Matrinez Sanchez, P., and Scorletti, P. (2009). Volatility and vehicle driveability performance of ethanol / gasoline blends : a literature review. *CONCAWE Fuels*, Brussels(report no. 8/09).

Strandh, P., Bengtsson, J., Johansson, R., Tunestål, P., and Johansson, B. (2004). Cycle-to-Cycle Control of a Dual-Fuel HCCI Engine. In *SAE Technical Paper*, volume 01.

Szybist, J. P. and Bunting, B. G. (2005). Cetane Number and Engine Speed Effects on Diesel HCCI Performance and Emissions. In *SAE Technical Papers*, number SAE #2005-01-3723.

Taylor, C. F. and Taylor, E. S. (1961). *The Internal-Combustion Engine*. International Textbook Company.

Truedsson, I., Cannella, W., Johansson, B., and Tuner, M. (2014). Development of New Test Method for Evaluating HCCI Fuel Performance. *SAE International*, SAE Techni.

Tsai, J., Koch, C. R., and Saif, M. (2012). Cycle Adaptive Feedforward Approach Controllers for an Electromagnetic Valve Actuator. *IEEE Transactions on Control Systems Technology*, 20(3):738–746.

Vuilleumier, D., Kozarac, D., Mehl, M., Saxena, S., Pitz, W. J., Dibble, R. W., Chen, J. Y., and Mani Sarathy, S. (2014). Intermediate temperature heat release in an HCCI engine fueled by ethanol/n-heptane mixtures: An experimental and modeling study. *Combustion and Flame*, 161(3):680–695.

Wang, D., Ye, Y., and Zhang, B. (2014). *Practical Iterative Learning Control with Frequency Domain Design and Sampled Data Implementation*. Advances in Industrial Control. Springer Singapore, Singapore.

Wang, Y., Gao, F., and Doyle, F. J. (2009). Survey on iterative learning control, repetitive control, and run-to-run control. *Journal of Process Control*, 19(10):1589–1600.

Warnatz, J., Maas, U., and Dibble, R. W. (2006). *Combustion: Physical and Chemical Fundamentals, Modeling and Simulation, Experiments, Pollutant Formation*. Springer Berlin Heidelberg.

Yang, Y., Dec, J. E., Dronniou, N., and Simmons, B. (2010). Characteristics of Isopentanol as a Fuel for HCCI Engines. *SAE International Journal of Fuels and Lubricants*, 3(2):2010–01–2164.

Yeom, K., Jang, J., and Bae, C. (2007). Homogeneous charge compression ignition of LPG and gasoline using variable valve timing in an engine. *Fuel*, 86(4):494–503.

Zhao, H., Peng, Z., and Ladommatos, N. (2001). Understanding of controlled autoignition combustion in a four-stroke gasoline engine. *Proceedings of the Institution of Mechanical Engineers, Part D: Journal of Automobile Engineering*, 215(12):1297–1310.

Appendix A

Calibrations

A.1 Injector Pulse Width Calibrations

A.1.1 Iso-Octane and n-Heptane

The injector are calibrated for iso-octane and n-heptane by injecting 1000 times into a bottle and measuring the total mass injected for each pulse width with fuel pressure of 287 kPa. The calibrations data is given in Figs. A.1 and A.2. The values from the linear regression are given in Table A.1.

A.1.2 Biofuel Mixtures

The injector are calibrated for the biofuels by measuring the fuel flow for a given pulse width and correcting using the fuel density and RPMs. Them mean RPMs for each test are 797. The calibrations data is given in Figs. A.1 and A.2. The values from the linear regression are given in Table A.2.

Table A.1: Linear regression results of injector calibrations.

Fuel	p_1	p_2	R^2
iso-octane	$1.572 \pm 0.12 \times 10^{-3}$	$-1.044 \pm 0.127 \times 10^{-3}$	0.9996
n-heptane	$1.493 \pm 0.11 \times 10^{-3}$	$-8.712 \pm 0.9 \times 10^{-4}$	0.9999

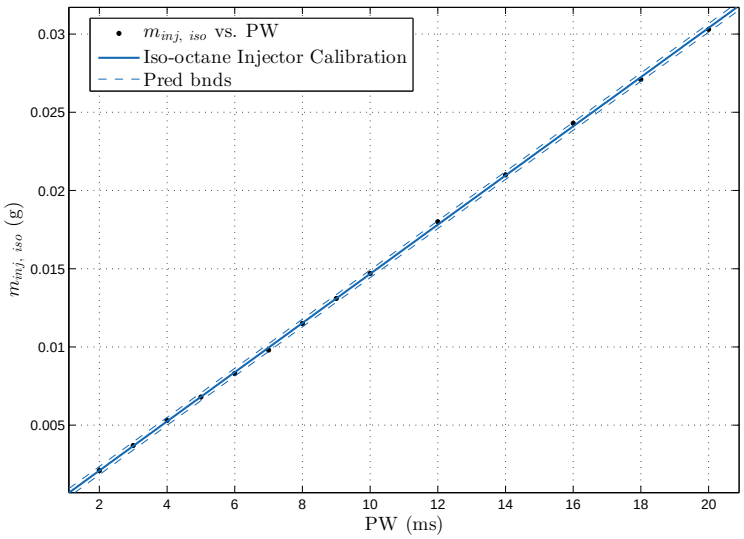

Figure A.1: Iso-Octane injector calibration.

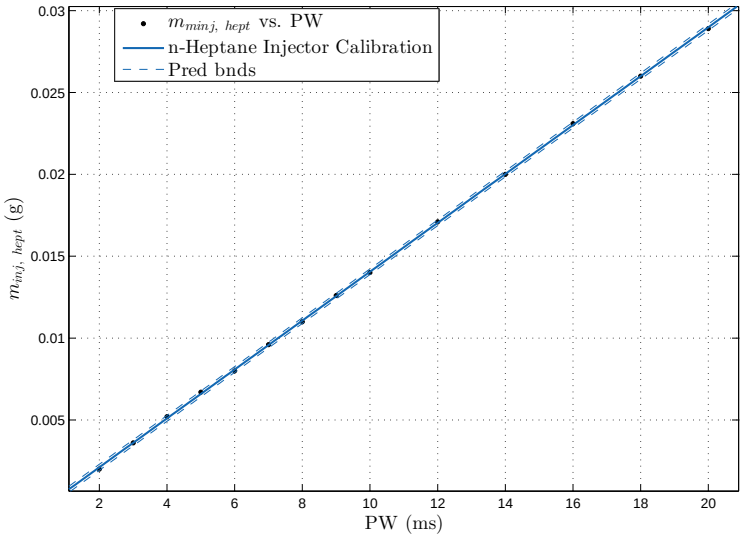

Figure A.2: n-Heptane injector calibration.

Table A.2: Linear regression results of biofuel injector calibrations.

Fuel	p_1	p_2	R^2
ethanol/iso-octane	$1.419 \pm 0.32 \times 10^{-3}$	$-1.117 \pm 0.126 \times 10^{-3}$	0.9996
biodiesel/n-heptane	$1.486 \pm 0.091 \times 10^{-3}$	$-1.467 \pm 0.616 \times 10^{-3}$	0.9963

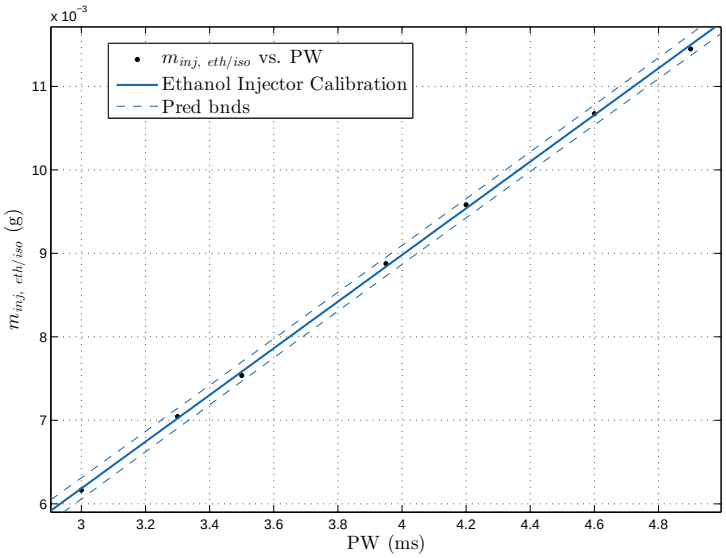

Figure A.3: Ethanol/iso-octane injector calibration.

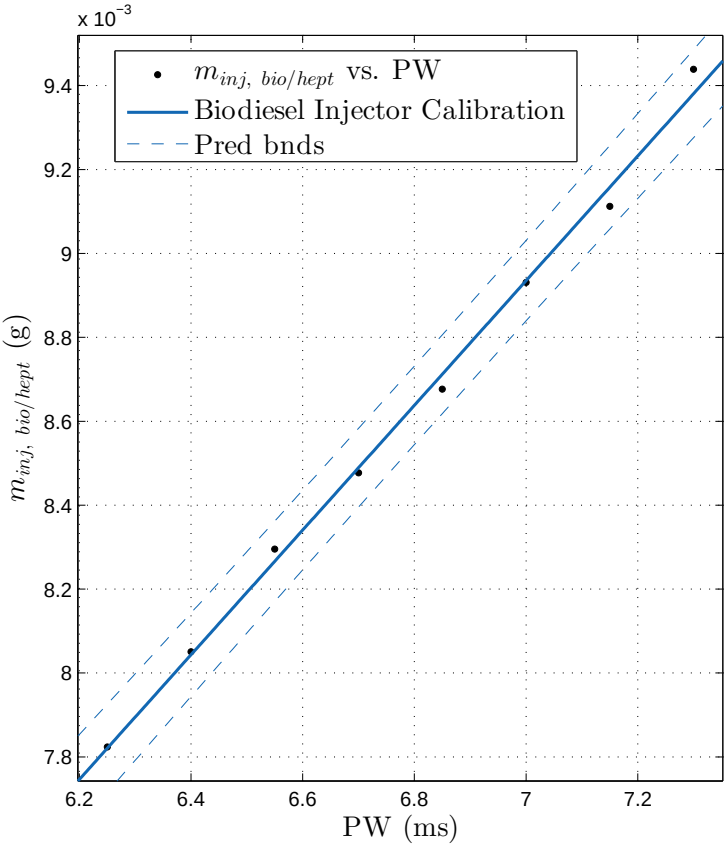

Figure A.4: Biodiesel/n-heptane injector calibration.

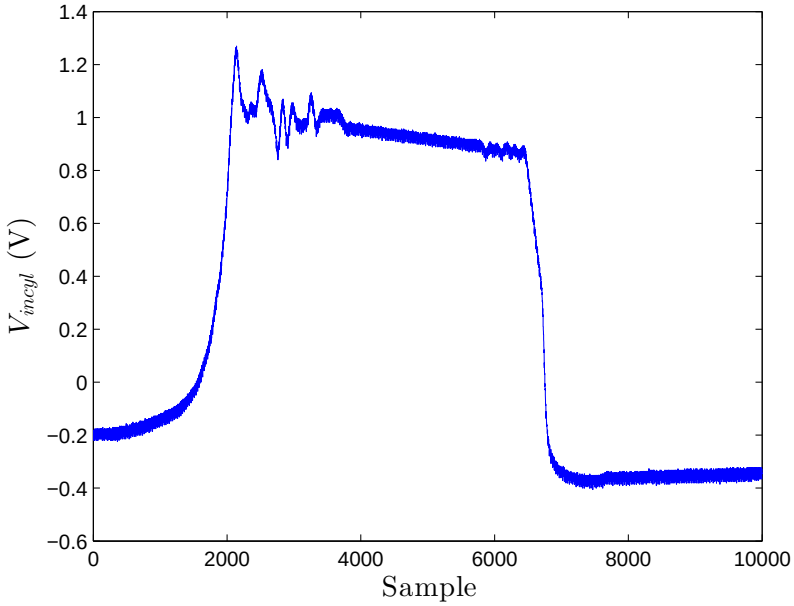

Figure A.5: Dynamic sensitivity testing of Kistler 6043A pressure transducer with 250 lbs step.

A.2 In-cylinder Pressure Calibration

The Kistler 6043A pressure transducer is the same used in Handford [2009]. The Handford did a in depth calibration for the pressure. Since the transducer drifts this makes calibration difficult as a dynamic calibration must be done. The value found from Handford [2009] is used for sensitivity. Two dynamic testings are done, similar to the procedure given in Handford [2009], to confirm the sensitivity has not changed. One with a 500 lbs step and the other with 250 lbs. The results are shown in Figs. A.5 and A.6 at 1000 Hz. The sensitivity are within the standard deviation given in Handford [2009], which gives the sensitivity as 205.5 psi/V with standard deviation of 8.01 psi/V.

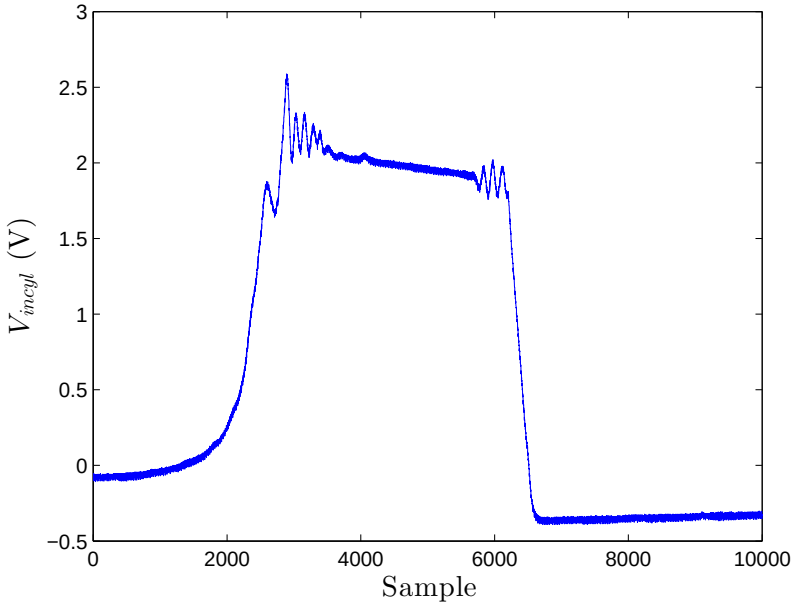

Figure A.6: Dynamic sensitivity testing of Kistler 6043A pressure transducer with 500 lbs step.

A.3 Validyne Calibrations

The Validyne intake and exhaust pressure transducer calibration plots are shown in Figs. A.7 and A.8, respectively with 95% confidence bounds. The calibration is done using a Omega Pressure Calibrator PCL-601. It has an accuracy of 0.04 kPa. Each point is the mean of 50000 data points with the maximum point standard deviation given in Table A.3. The calibration is assumed to take the form of:

$$P = mV + b \tag{A.1}$$

with P being the pressure, V is the voltage and m and b are found from the linear regression given in Table A.3 with 95% confidence bounds and R^2 of the regression.

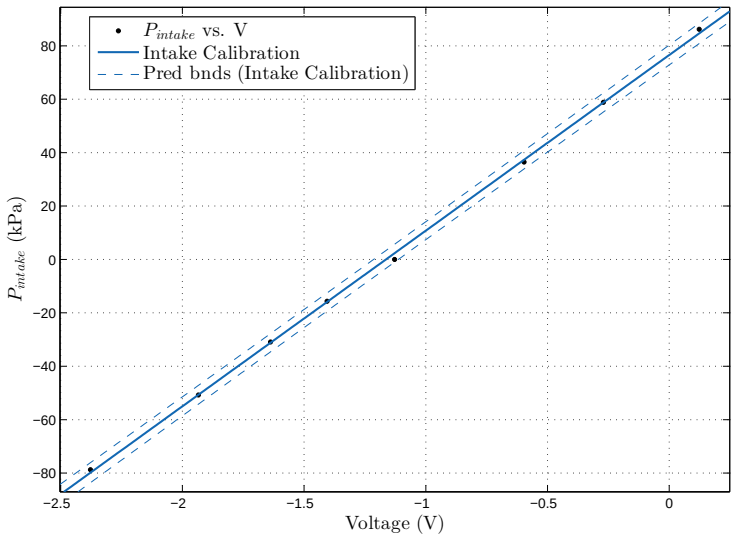

Figure A.7: Intake pressure calibration plot relating voltage to intake pressure.

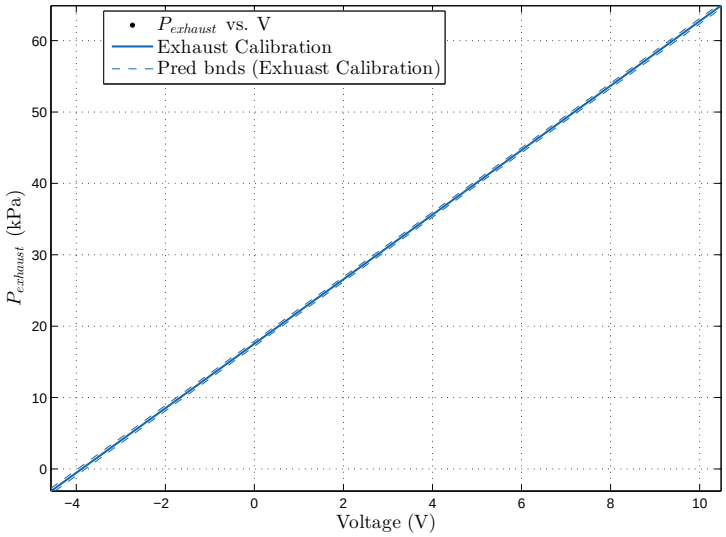

Figure A.8: Exhaust pressure calibration plot relating voltage to exhaust pressure.

Table A.3: Calibration of pressure transducers.

Pressure	m	b	R^2	standard deviation
Intake	65.78±1.4	76.56±1.96	0.9996	0.0036
Exhaust	4.518±0.026	17.54±0.15	1	0.0029

Appendix B

Error Analysis

The uncertainties are calculated using formulas given in Moffat [1988]. The sources of error are either "fixed" or "random" with errors being called *bias* and *precision* errors Moffat [1988]. For this study, calibrations were done for most measurements therefore the bias errors are considered negligible. The thermocouples were not calibrated but are tested with both an ice bath and boiling water and no bias error is found. For a measurement $X_i \pm \delta X_i$, δX_i is the uncertainty in the measurement X_i. This uncertainty is taken as the 95% confidence interval for this study. This number indicates that the true value has 20:1 odds of being within this interval. Here the true value is taken as the measurement system value, i.e. for a thermocouple measurement the true value is the temperature at the thermocouple junction. There are two types of uncertainty: Single sample and multi-sample Moffat [1988]. For single sample the uncertainty is given as:

$$\delta X_i = 2\sigma \tag{B.1}$$

where σ is the population standard deviation. Since calculation for standard deviations use more than 1000 observations, the sample standard deviation approximates

the population standard deviation well according to the central limit theorem.

For multi-sample uncertainty, the uncertainty is calculated as:

$$\delta X_i = \frac{tS_N}{\sqrt{N}} \tag{B.2}$$

where N is the number of samples, t is the Student's t statistic appropriate for the number of samples and confidence level, and S_N is the sample standard deviation.

For values calculated from measurements as $R = R(X_1, X_2, ..., X_n)$ the uncertainty is given as:

$$\delta R = \sqrt{\sum_{i=1}^{N} \left(\frac{\partial R}{\partial X_i} \delta X_i \right)^2} \tag{B.3}$$

Most calculations are from a linear calibration such as $Y = mX + b$. For these, eqn. B.3 becomes:

$$\delta Y = \sqrt{(X\delta m)^2 + (m\delta X)^2 + (\delta b)^2} \tag{B.4}$$

where δm and δb are from the linear regression of the calibration and X is taken as the maximum value observed. This equation is used to calculate the single sample uncertainties for intake pressure, in-cylinder pressure, exhaust pressure, injectors and torque. For thermocouples, eqn. B.1 is used for single sample uncertainty. For these measurements the accuracy of the measurement systems are much lower than the calculated values from the system standard deviation and therefore are not included. For in-cylinder pressure measurement δb is taken as the uncertainty in the intake

measurement as it is used to peg the in-cylinder pressure trace.

B.1 IMEP and CA50 Error

IMEP and CA50 are not easily calculated, therefore eqn. B.3 is difficult to apply. Instead, as suggested in Moffat [1988], the uncertainty is calculated using computer simulation of the noise. This done by taking an ensemble of 100 cycles in-cylinder and intake voltage measurements and calculating the CA50 and IMEP from the mean combustion trace. Then this is repeated 1000 times with the addition of Gaussian white noise in the signals as well as the calibration values with their respective standard deviations. This gives a normal distribution, shown in Figs. B.1 and B.2, of the resulting CA50 and IMEP values caused by errors in the calibration and system noise. Then two times the standard deviations of these distributions are used as the single sample errors of their respective values. A normal probability density function is plotted with the histograms in Figs. B.1 and B.2 to show how close to a normal distributions the results are.

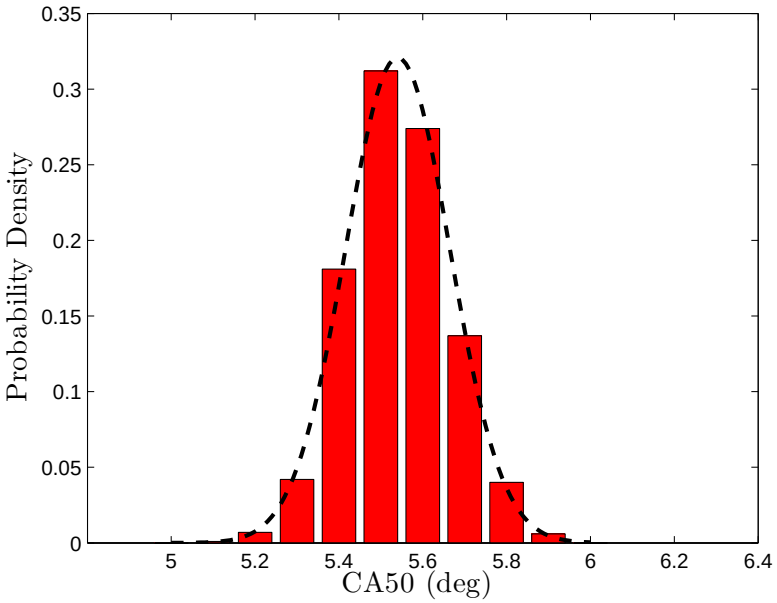

Figure B.1: CA50 calculations with mean of 5.5 deg and addition of simulated Gaussian white noise.

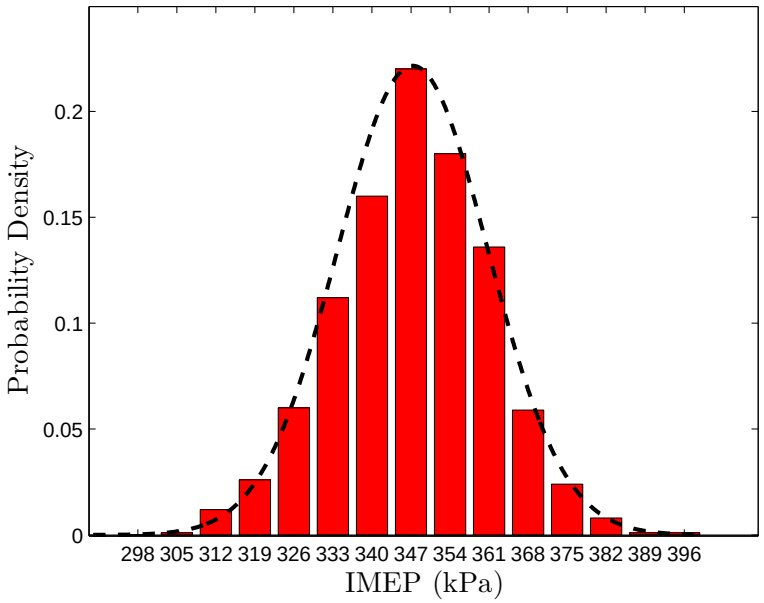

Figure B.2: IMEP calculations with mean of 347 kPa and addition of simulated Gaussian white noise.

Appendix C

System Identification

C.1 ARMAX Coefficients

The ARMAX model coefficients found from the system identification in Section 4.2.2 is given below

$$A_{11} = 1 - 1.13\,(\pm 0.026)\,z^{-1} + 0.1533\,(\pm 0.025)\,z^{-2} \tag{C.1}$$

$$A_{22} = 1 - 0.876\,(\pm 0.068)\,z^{-1} + 0.04965\,(\pm 0.014)\,z^{-2} \tag{C.2}$$

$$B_{11} = -87.27\,(\pm 2.4)\,z^{-1} + 85\,(\pm 2.4\,)z^{-2} \tag{C.3}$$

$$B_{12} = 5.726\,(\pm 0.47)\,z^{-1} - 5.159\,(\pm 0.48)\,z^{-2} \tag{C.4}$$

$$B_{21} = 419.3\,(\pm 11\,)z^{-1} - 336.2\,(\pm 30)\,z^{-2} \tag{C.5}$$

$$B_{22} = 462.2\,(\pm 5.5)\,z^{-1} - 372.9\,(\pm 30)\,z^{-2} \tag{C.6}$$

$$C_1 = 1 - 1.011\,(\pm 0.046\,)z^{-1} + 0.1757\,(\pm 0.043)\,z^{-2} \tag{C.7}$$

$$C_2 = 1 - 0.963\,(\pm 0.075\,)z^{-1} + 0.1956\,(\pm 0.039)\,z^{-2} \tag{C.8}$$

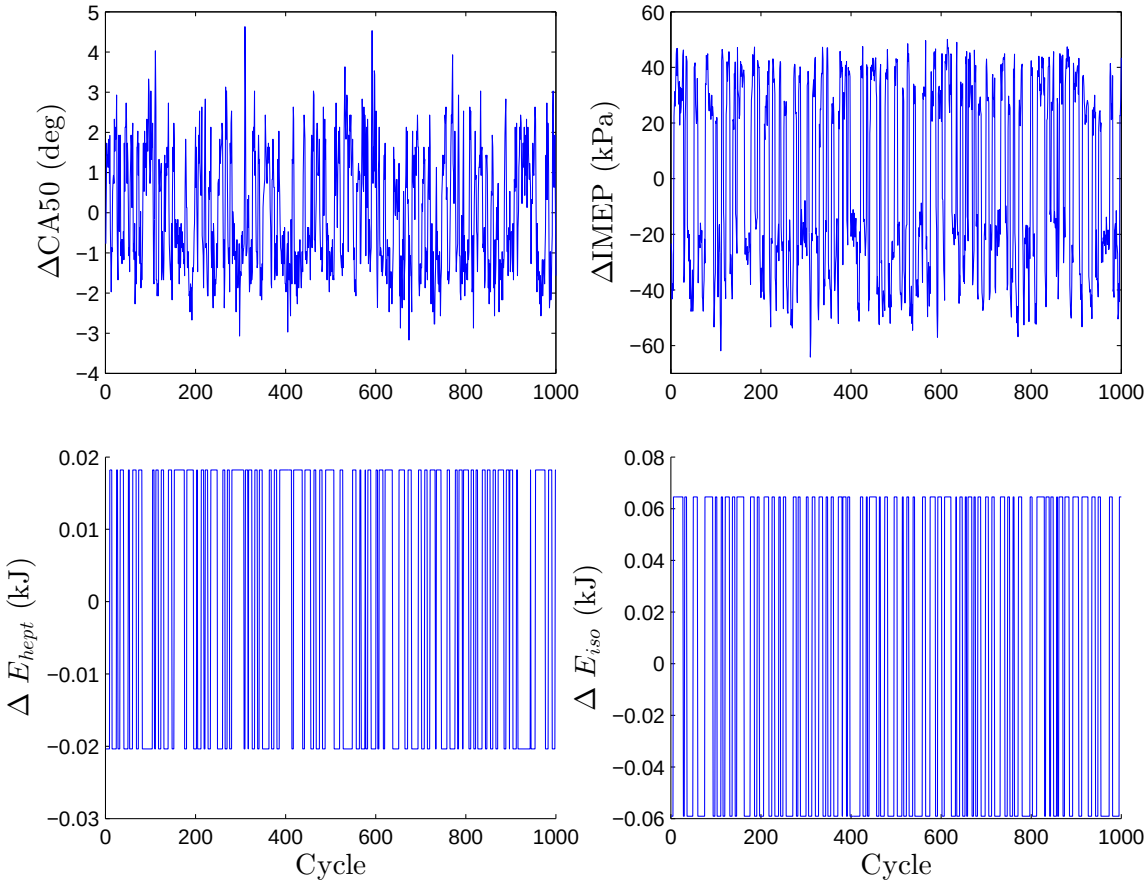

Figure C.1: PRBS inputs and engine responses with $T_{int} = 50°C$.

C.2 PRBS Operating Conditions

Shown in this section are the PRBS results used for finding the Markov Parameters in Section 5.1

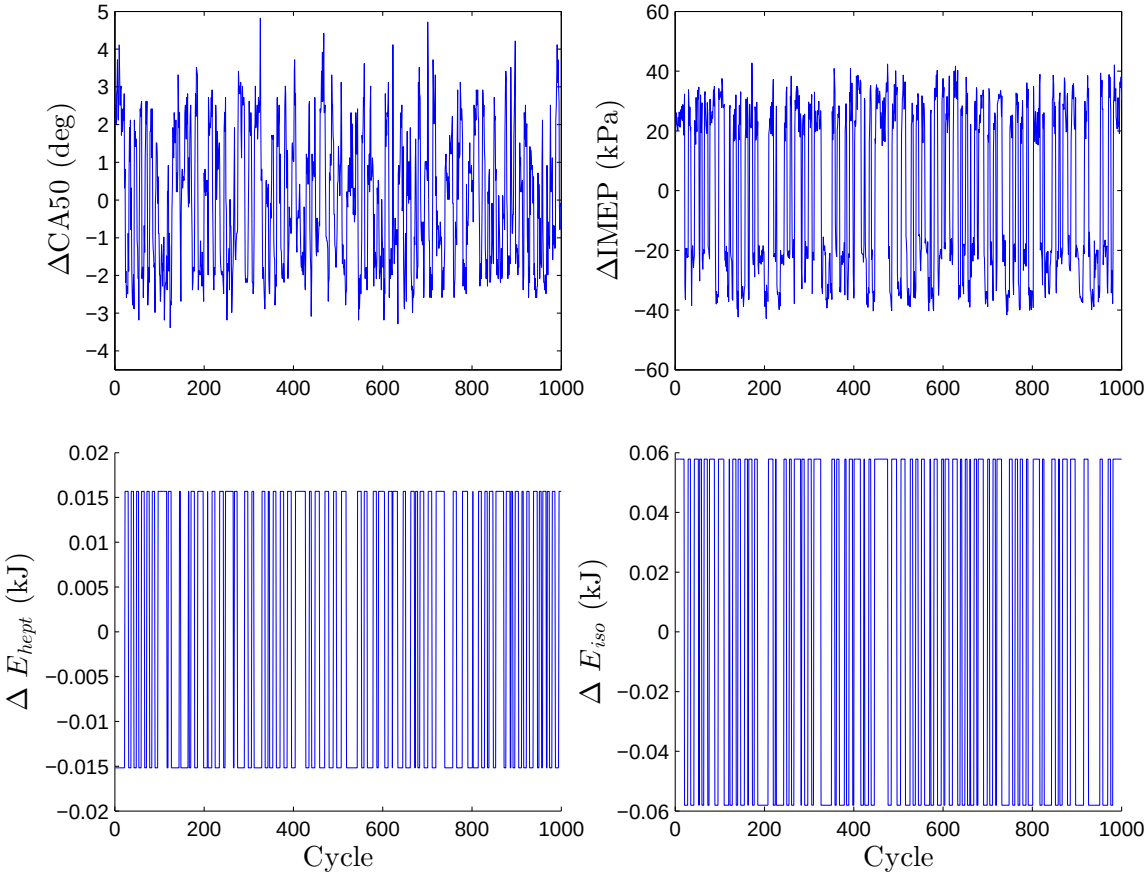

Figure C.2: PRBS inputs and engine responses with $T_{int} = 150°C$.

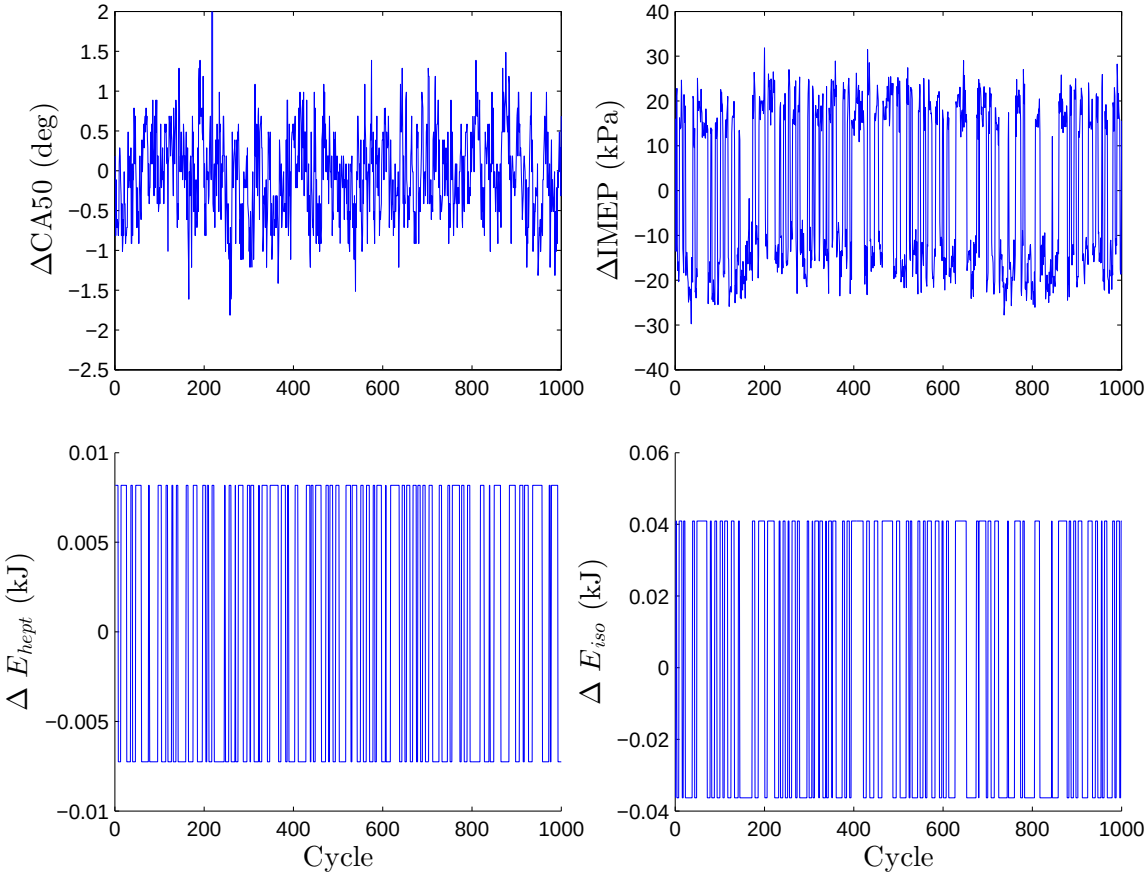

Figure C.3: PRBS inputs and engine responses with CR=10.

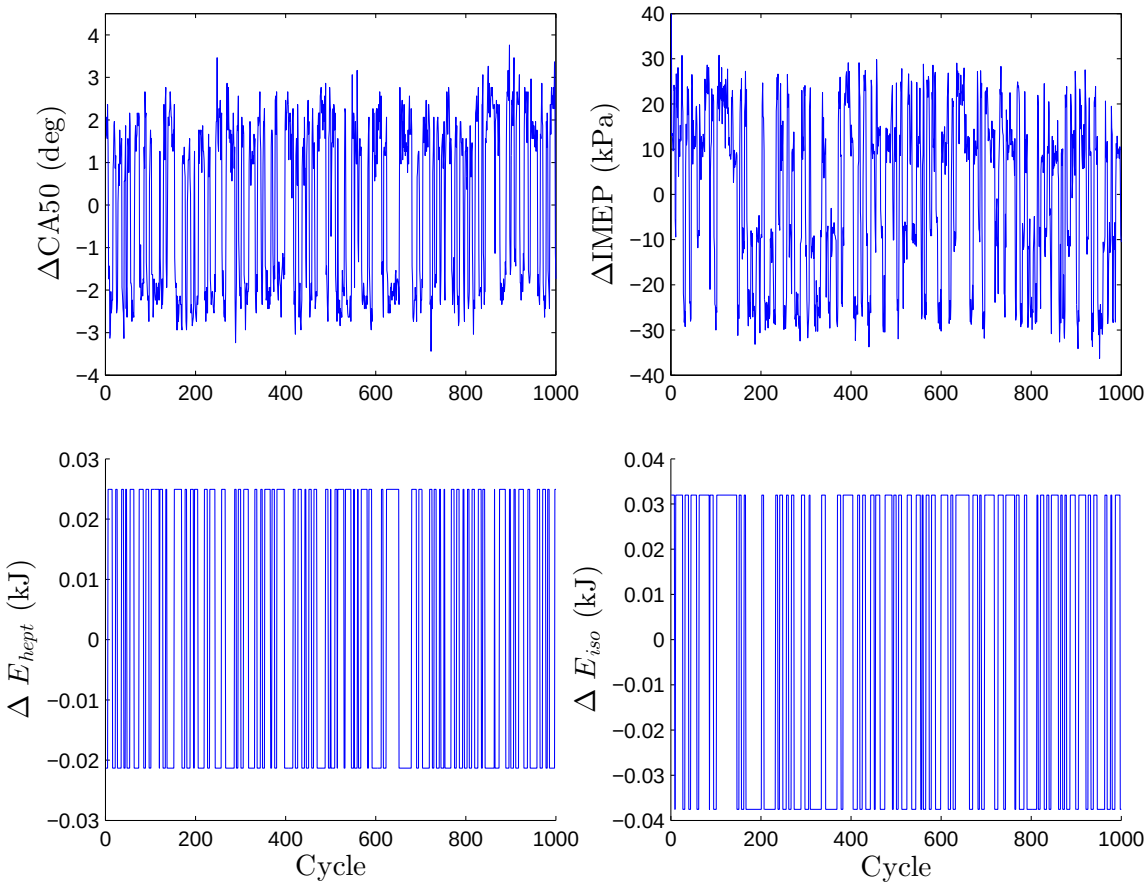

Figure C.4: PRBS inputs and engine responses with CR=12.

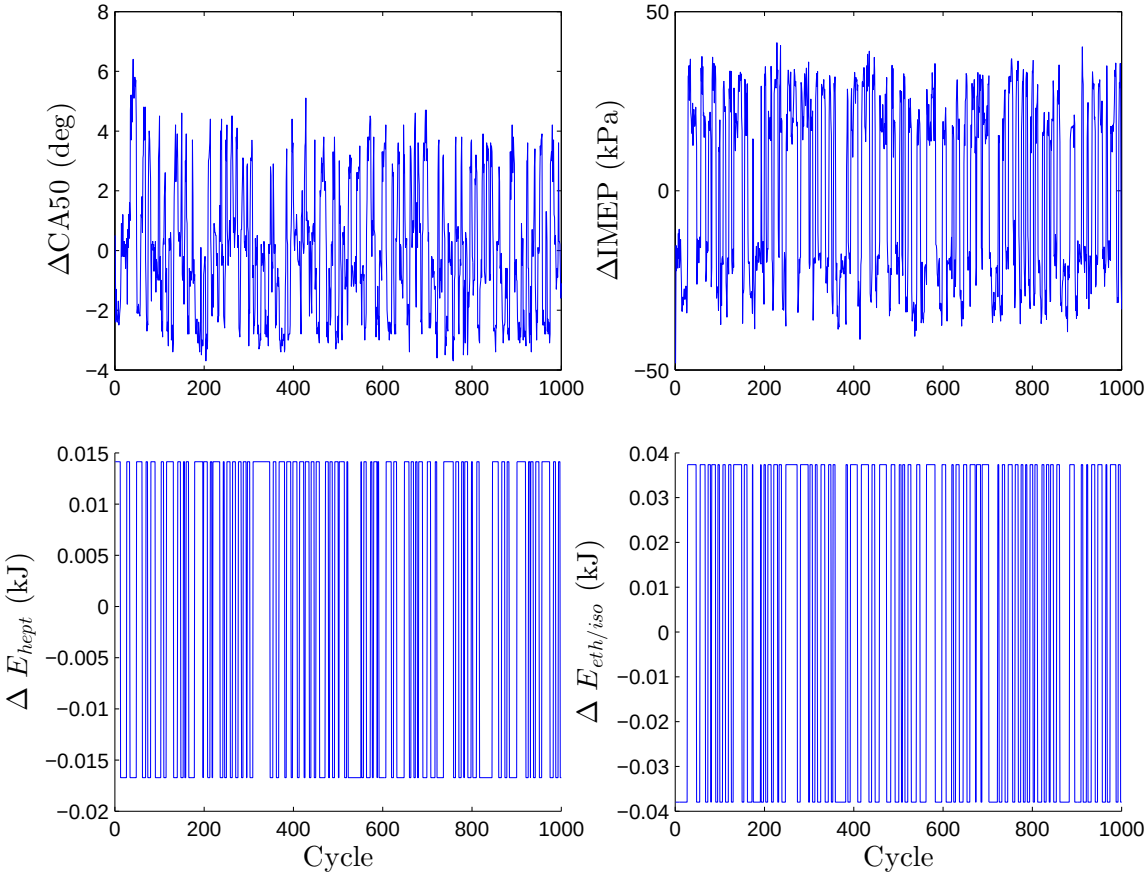

Figure C.5: PRBS inputs and engine responses with $E_{eth/iso}$.

C.3 PRBS Biofuels

Shown in this section are the PRBS results used for finding the Markov Parameters in Section 5.2

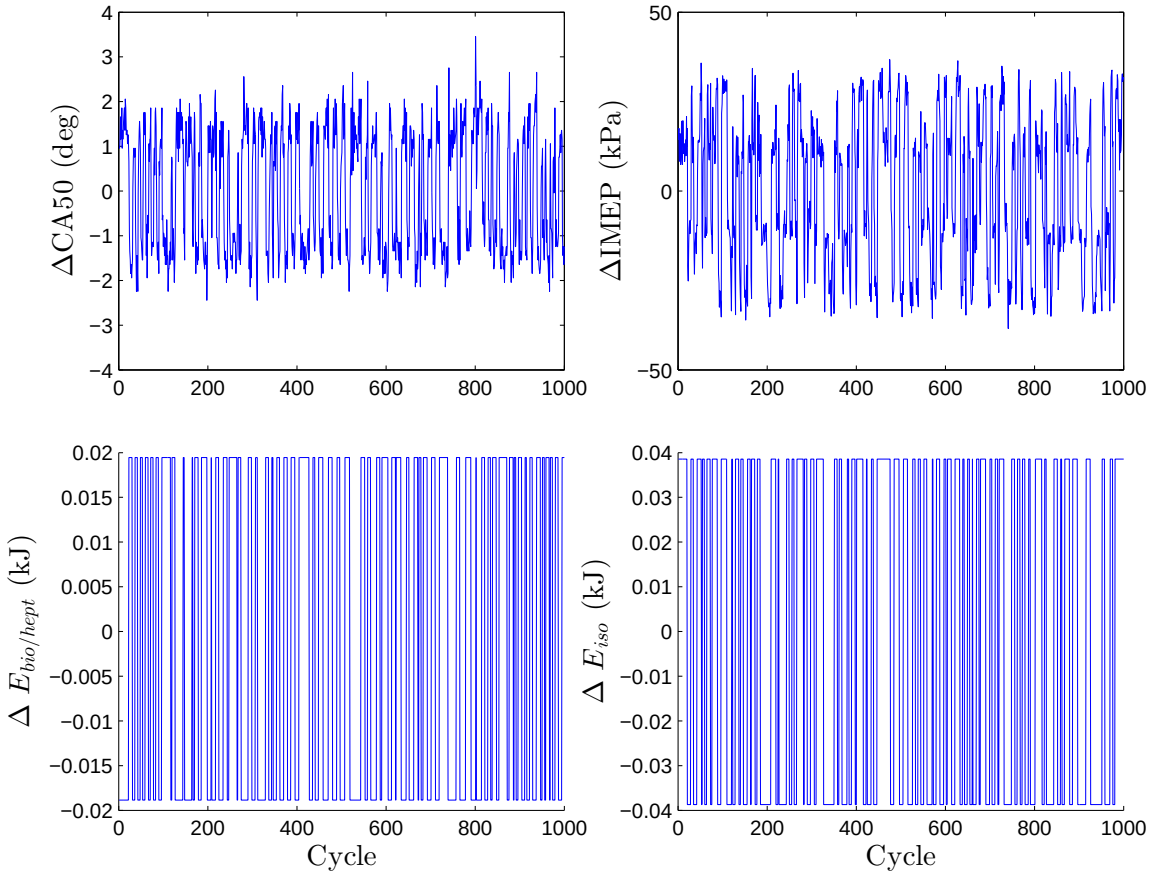

Figure C.6: PRBS inputs and engine responses with $E_{bio/hept}$.

C.4 ARMAX Coefficients for Operating Condition Changes

The ARMAX coefficients for $T_{int} = 50°C$:

$$A_{11} = 1 - 0.8092\,(\pm 0.07043)\,z^{-1} \tag{C.9}$$

$$A_{12} = 0.001934\,(\pm 0.002853)\,z^{-1} \tag{C.10}$$

$$A_{22} = 1 - 1.227\,(\pm 0.1202)\,z^{-1} + 0.2429\,(\pm 0.1164)\,z^{-2} \tag{C.11}$$

$$B_{11} = -57.18\,(\pm 2.255)\,z^{-1} + 32.01\,(\pm 5.702\,)z^{-2} + 15.36\,(\pm 4.002\,)z^{-3} - 4.522\,(\pm 2.273\,)z^{-4} \tag{C.12}$$

$$B_{12} = -1.881\,(\pm 0.6946)\,z^{-1} + 4.812\,(\pm 1.825)\,z^{-2} - 3.975\,(\pm 1.214)\,z^{-3} + 2.21\,(\pm 0.694)\,z^{-4} \tag{C.13}$$

$$B_{21} = 416.4\,(\pm 21.88\,)z^{-1} - 464\,(\pm 72.1)\,z^{-2} + 53.95\,(\pm 59.41)\,z^{-3} \tag{C.14}$$

$$B_{22} = 475.9\,(\pm 6.817)\,z^{-1} - 542.4\,(\pm 64.87)\,z^{-2} + 75.1\,(\pm 60.63)\,z^{-3} \tag{C.15}$$

$$C_1 = 1 - 0.630\,(\pm 0.079\,)z^{-1} - 0.0641\,(\pm 0.047)\,z^{-2} - 0.00879\,(\pm 0.045\,)z^{-3} - 0.01487\,(\pm 0.04563\,)z^{-4} + 0.08209\,(\pm 0.04128\,)z^{-5} \tag{C.16}$$

$$C_2 == 1 - 1.057\,(\pm 0.13\,)z^{-1} + 0.0988\,(\pm 0.11)\,z^{-2} + 0.00587\,(\pm 0.057\,)z^{-3} + 0.004928\,(\pm 0.039\,)z^{-4} \tag{C.17}$$

The ARMAX coefficients for $T_{int} = 150°C$:

$$A_{11} = 1 - 0.904\,(\pm 0.02604)\,z^{-1} \tag{C.18}$$

$$A_{12} = 0.002037\,(\pm 0.003622)\,z^{-1} \tag{C.19}$$

$$A_{22} = 1 - 1.04\,(\pm 0.01626)\,z^{-1} + 0.06185\,(\pm 0.007241)\,z^{-2} \tag{C.20}$$

$$B_{11} = -84.35\,(\pm 1.974)\,z^{-1} + 63.83\,(\pm 5.394\,)z^{-2} + 5.394\,(\pm 3.671\,)z^{-3} \tag{C.21}$$
$$+ 3.814\,(\pm 3.504\,)z^{-4} + 2.55\,(\pm 1.97\,)z^{-5}$$

$$B_{12} = 15.63\,(\pm 0.5035)\,z^{-1} - 16.6\,(\pm 1.96)\,z^{-2} + 1.012\,(\pm 0.9564)\,z^{-3} \tag{C.22}$$
$$+ 1.926\,(\pm 0.9083)\,z^{-4} + 0.7584\,(\pm 0.5212)\,z^{-5}$$

$$B_{21} = 352.1\,(\pm 8.203\,)z^{-1} - 347.1\,(\pm 8.967)\,z^{-2} \tag{C.23}$$

$$B_{22} = 458.9\,(\pm 3.424)\,z^{-1} - 447.5\,(\pm 7.334)\,z^{-2} \tag{C.24}$$

$$C_1 = 1 - 0.67\,(\pm 0.046\,)z^{-1} - 0.01076\,(\pm 0.047)\,z^{-2} - 0.03862\,(\pm 0.047\,)z^{-3} \tag{C.25}$$
$$+ 0.06395\,(\pm 0.04074\,)z^{-4}$$

$$C_2 == 1 - 1.161\,(\pm 0.0425\,)z^{-1} + 0.2201\,(\pm 0.06)\,z^{-2} + 0.09169\,(\pm 0.06\,)z^{-3} \tag{C.26}$$
$$- 0.09132\,(\pm 0.03958\,)z^{-4}$$

The ARMAX coefficients for CR=10:

$$A_{11} = 1 - 0.275\,(\pm 0.06854)\,z^{-1} + 0.0187\,(\pm 0.05328)\,z^{-2} \tag{C.27}$$

$$A_{12} = 0.006339\,(\pm 0.001107)\,z^{-1} \tag{C.28}$$

$$A_{22} = 1 - 0.9627\,(\pm 0.01708)\,z^{-1} \tag{C.29}$$

$$B_{11} = -35.01\,(\pm 2.443)\,z^{-1} \tag{C.30}$$

$$B_{12} = 6.122\,(\pm 0.5089)\,z^{-1} \tag{C.31}$$

$$B_{21} = 328\,(\pm 20.63)\,z^{-1} - 315.9\,(\pm 21.39)\,z^{-2} \tag{C.32}$$

$$B_{22} = 448\,(\pm 4.194)\,z^{-1} - 428.8\,(\pm 9.1))\,z^{-2} \tag{C.33}$$

$$C_1 = 1 - 0.116\,(\pm 0.078)\,z^{-1} + 0.178\,(\pm 0.059)\,z^{-2} + 0.00935\,(\pm 0.039)\,z^{-3} + 0.1241\,(\pm 0.03844)\,z^{-4} \tag{C.34}$$

$$C_2 = 1 - 0.935\,(\pm 0.042)\,z^{-1} + 0.0733\,(\pm 0.053))\,z^{-2} + 0.0452\,(\pm 0.053)\,z^{-3} - 0.03257\,(\pm 0.04006)\,z^{-4} \tag{C.35}$$

The ARMAX coefficients for CR=12:

$$A_{11} = 1 - 0.1679\,(\pm 0.01316)\,z^{-1} \tag{C.36}$$

$$A_{22} = 1 - 0.1145\,(\pm 0.012)\,z^{-1} \tag{C.37}$$

$$B_{11} = -70.53\,(\pm 1.061)\,z^{-1} \tag{C.38}$$

$$B_{12} = 6.775\,(\pm 0.5342)\,z^{-1} \tag{C.39}$$

$$B_{21} = 284.9\,(\pm 6.731)\,z^{-1} \tag{C.40}$$

$$B_{22} = 440\,(\pm 6.063)\,z^{-1} \tag{C.41}$$

$$C_1 = 1 - 0.0526\,(\pm 0.040)\,z^{-1} + 0.08776\,(\pm 0.038)\,z^{-2} + 0.107\,(\pm 0.039)\,z^{-3} + 0.1358\,(\pm 0.039)\,z^{-4} \tag{C.42}$$

$$C_2 = 1 - 0.1481\,(\pm 0.04)\,z^{-1} + 0.06088\,(\pm 0.038)\,z^{-2} + 0.00417\,(\pm 0.039)\,z^{-3} + 0.04379\,(\pm 0.03854)\,z^{-4} \tag{C.43}$$

The ARMAX coefficients for $E_{eth/iso}$:

$$A_{11} = 1 - 0.9245\,(\pm 0.03002)\,z^{-1} \tag{C.44}$$

$$A_{12} = -0.005901\,(\pm 0.004404)\,z^{-1} \tag{C.45}$$

$$A_{22} = 1 - 1.01\,(\pm 0.1037)\,z^{-1} + 0.02863\,(\pm 0.1008)\,z^{-2} \tag{C.46}$$

$$B_{11} = -62.73\,(\pm 2.21)\,z^{-1} + 39.03\,(\pm 5.019)\,z^{-2} + 11.58\,(\pm 3.925)\,z^{-3} + 3.727\,(\pm 2.199)\,z^{-4}\,z^{-4} \tag{C.47}$$

$$B_{12} = 45.42\,(\pm 0.9444)\,z^{-1} - 46.92\,(\pm 2.808)\,z^{-2} + 1.97\,(\pm 1.722)\,z^{-3} - 0.3021\,(\pm 0.9698)\,z^{-4} \tag{C.48}$$

$$B_{21} = 359.3\,(\pm 12.84)\,z^{-1} - 304.7\,(\pm 48.52)\,z^{-2} - 45.6\,(\pm 42.17)\,z^{-3} \tag{C.49}$$

$$B_{22} = 610.2\,(\pm 5.597)z\,z^{-1} - 566.4\,(\pm 69.74)\,z^{-2} - 30\,(\pm 66.18)\,z^{-3} \tag{C.50}$$

$$C_1 = 1 - 0.66\,(\pm 0.05)\,z^{-1} + 6.67 \times 10^{-5}\,(\pm 0.05)\,z^{-2} - 0.053\,(\pm 0.05)\,z^{-3} - 0.01542\,(\pm 0.04071)\,z^{-4} \tag{C.51}$$

$$C_2 = 1 - 1.073\,(\pm 0.11)\,z^{-1} + 0.1282\,(\pm 0.12)\,z^{-2} + 0.001143\,(\pm 0.057)\,z^{-3} + 0.0105\,(\pm 0.0388)\,z^{-4} \tag{C.52}$$

The ARMAX coefficients for $E_{bio/hept}$:

$$A_{11} = 1 - 0.5885\,(\pm 0.2766)\,z^{-1} \tag{C.53}$$

$$A_{22} = 1 - 0.6209\,(\pm 0.1313)\,z^{-1} \tag{C.54}$$

$$B_{11} = -48.63\,(\pm 1.253)\,z^{-1} + 12.94\,(\pm 13.6)\,z^{-2} + 3.834\,(\pm 4.434)\,z^{-3} + 2.05\,(\pm 2.673)\,z^{-4} \tag{C.55}$$

$$B_{12} = 3.325\,(\pm 0.6018)\,z^{-1} - 1.101\,(\pm 1.355)\,z^{-2} - 1.675\,(\pm 1.012)\,z^{-3} + 1.034\,(\pm 0.6038)\,z^{-4} \tag{C.56}$$

$$B_{21} = 344.5\,(\pm 12.75)\,z^{-1} - 130.5\,(\pm 47.56)\,z^{-2} - 35.39\,(\pm 21.95)\,z^{-3} \tag{C.57}$$

$$B_{22} = 450.4\,(\pm 6.073)\,z^{-1} - 218.1\,(\pm 58.05)\,z^{-2} - 28.57\,(\pm 13.55)\,z^{-3} \tag{C.58}$$

$$C_1 = 1 - 0.5308\,(\pm 0.279)\,z^{-1} + 0.02244\,(\pm 0.0463)\,z^{-2} + 0.065\,(\pm 0.046)\,z^{-3} - 0.05669\,(\pm 0.04708)\,z^{-4} \tag{C.59}$$

$$C_2 = 1 - 0.6147\,(\pm 0.14)\,z^{-1} + 0.01531\,(\pm 0.046)\,z^{-2} - 0.01402\,(\pm 0.045)\,z^{-3} + 0.03048\,(\pm -0.03878)\,z^{-4} \tag{C.60}$$

Appendix D

Matrix Approximation Proof and Interval Matrix Results

D.1 Vertex Matrix

Shown is the spectral radius as a function of K for each vertex matrix, 16 in total, discussed in Section 4.3.3. Fig. 4.15 is created from Fig. D.1 in that at every K, the maximum value of the spectral radius is the maximum of the 16 traces shown in Fig. D.1.

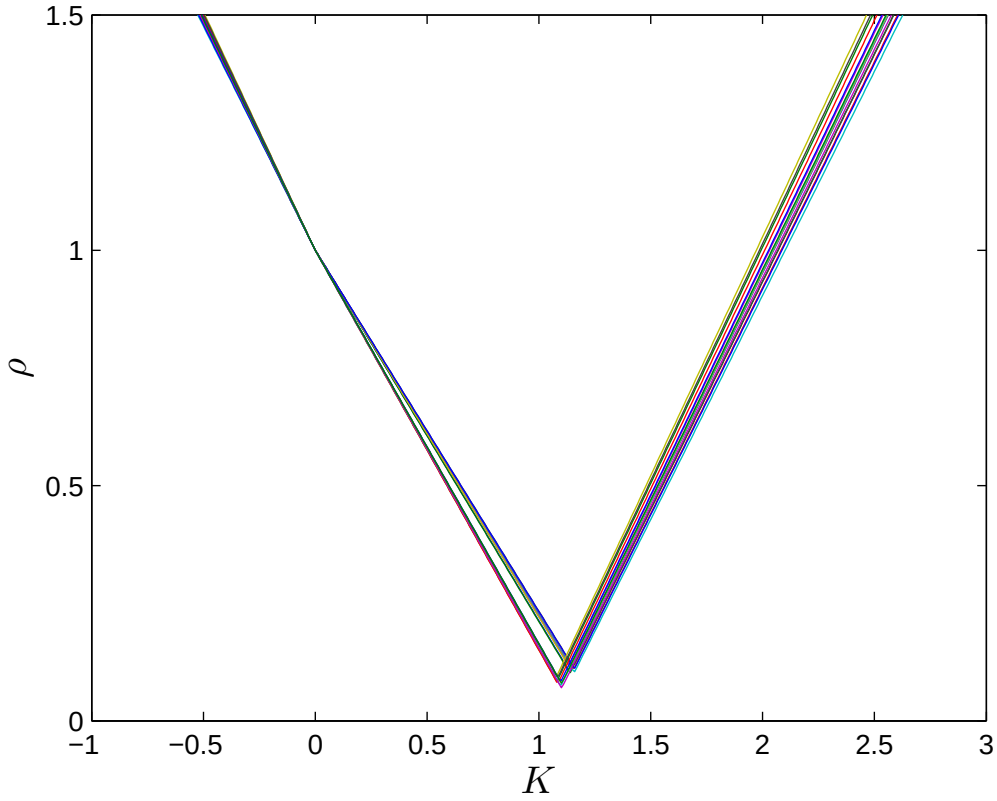

Figure D.1: All spectral radius of vertex matrices from Markov Parameters shown in Fig 4.9 for varying K.

D.2 Matrix Approximation Proof

Theorem: If $\overline{\sigma}(A) << \underline{\sigma}(B)$ then $I + AB^{-1} \approx I$.

Proof: If the matrix is real, it can be decomposed into two orthogonal rotation matrices and a scaling matrix in Singular Value Decomposition Golub and Van Loan [1996] such as:

$$A = U_A \Sigma_A V_A^T \tag{D.1}$$

Where U_A and V_B are orthogonal rotation matrices, meaning $||x|| = ||Ux|| \ \forall x$, and Σ_A is a diagonal matrix containing the singular values of A. Assuming B is invertible $B^{-1} = V_B \Sigma_B^{-1} U_A^T$. Then AB^{-1} can be written as:

$$AB^{-1} = U_A \Sigma_A V_A^T V_B \Sigma_B^{-1} U_B^T \tag{D.2}$$

Lemma Product of two orthogonal matrices is orthogonal as well.

Proof Unitary matrices are defined that their transpose is their inverse if square, i.e. $UU^T = I$ Golub and Van Loan [1996]. This implies that the inverse is also orthogonal. Given two orthogonal matrices U and V:

$$UV(UV)^T = UVV^T U^T \tag{D.3}$$

$$= UIU^T \tag{D.4}$$

$$= UU^T \tag{D.5}$$

$$= I \tag{D.6}$$

Rewriting eqn. D.2 with the following substitutions:

$$R = V_A^T V_B \tag{D.7}$$

$$C = \Sigma_A R \Sigma_B^{-1} \tag{D.8}$$

Gives:

$$AB^{-1} = U_A C U_B^T \tag{D.9}$$

C is the application of a rotation matrix, R, on a scaling matrix, Σ_B^{-1}, then multiplied by another scaling matrix, Σ_A. This means the column vector norm's maximums and minimums of C are only manipulated by the scaling matrices. R determines in what direction the second scaling affects the first; Intuitively if the maximum singular value of Σ_A lines up with the maximum singular value of Σ_B^{-1} will give the maximum column norm of C. With c_i, and $\sigma_{A,i}$ are the column vectors of C and Σ_A respectively with $\sigma_{B,i}$ being the row vectors of Σ_B^{-1}.

$$\langle c_i, c_i \rangle = \sum_{k=1}^{n} (\sigma_{A,i} \cdot \sigma_{B,k})^2 \tag{D.10}$$

$$\langle c_i, c_i \rangle = \sum_{k=1}^{n} (||\sigma_{A,i}|| \cdot ||\sigma_{B,k}|| \cos\theta_k)^2 \tag{D.11}$$

With θ_k being the angles between the angles between the $\sigma_{B,i}$ and $\sigma_{A,i}$ caused by the rotation matrix R. The domain of $\theta_k,\ 1 \leq k \leq n,\ k \in \mathbb{N}$ for is defined by:

$$1 = \sum_{k=1}^{n} \cos^2\theta_k \tag{D.12}$$

Since Σ_A and Σ_B^{-1} are the diagonal matrices with positive values, $||\sigma_{A,i}||$ and $||\sigma_{B,i}||$

are just the i^{th} diagonal value of Σ_A and Σ_B^{-1}. With the σ_A and σ_A being the max singular value of Σ_A and Σ_B^{-1} respectively.

$$\langle c_i, c_i \rangle = \sum_{k=1}^{n} (||\sigma_{A,i}|| \cdot ||\sigma_{B,k}|| \cos\theta_k)^2 \tag{D.13}$$

$$= \sum_{k=1}^{n} (\sigma_A \cdot \sigma_B \cos\theta_k)^2 \leq (\sigma_A \sigma_B)^2 \quad \forall i \tag{D.14}$$

This means the column norms of C are bounded by the product of the max singular values of Σ_A and Σ_B^{-1}, (minimum singular value of Σ_B). C can be written as:

$$C = U_C \Sigma_C V_C^T \tag{D.15}$$

Since U_C and V_C^T are orthogonal matrices, the largest singular value of C must also be bounded by product of the max singular values of Σ_A and Σ_B^{-1}. Combining Eqs. D.2 and D.15 gives:

$$AB^{-1} = U_A U_C \Sigma_C V_C^T U_B^T \tag{D.16}$$

$$= U \Sigma_C V^T \tag{D.17}$$

With $U_A U_C = U$ and $V_C^T U_B^T = V^T$ being new rotation matrices. Using the same logic that orthogonal matrices do not change the column norms of a matrix, the column norms of AB^{-1} are bounded by the product of the max singular values of Σ_A and Σ_B^{-1} as well.

If $\overline{\sigma}(A) << \underline{\sigma}(B)$ then $\overline{\sigma}(A)\underline{\sigma}(B)^{-1} << 1$ which is the upper bound of the column norms of AB^{-1}. Since the column norms of I are 1, and $||v + u|| \leq ||u|| + ||v||$ for vector norms, the column norms of $I + AB^{-1}$ are ≈ 1 meaning $I + AB^{-1} \approx I$.

Appendix E

Program List

Table E.1: File name and brief description of its purpose.

File Name	Description
EngineDAQSystem_wControl_ILC_v07.c	Runs NI DAQ and engine control program for ILC and steady-state data collection
EngineDAQSystem_wControl_PID_v07.c	Runs NI DAQ and engine control program for PID control
DataProcess_v02.m	Initialize workspace for CFR engine parameters and calculates and filters in-cylinder pressure
pressanalysis_08.m	Calculates relevant engine operation values, e.g. CA50, IMEP, from in-cylinder pressure
difference.m	Differencing scheme function
domainPlot.m	Plots steady-state responses of engine parameters vs. injected energies
SysID.m	Finds and tests ARMAX coefficients and Markov parameters
PIDanalysis.m	Analyze PI engine responses
IntervalStability.m	Calculate spectral radius of vertex matrix from interval matrix
ILCcompare.m	Analyze all ILC engine response data
ILCsim.m	Simulate ILC on ARMAX model